Atomic dynamics in the solid and liquid phases

by

Eleftherios Andritsos

Submitted in partial fulfillment
of the requirements of the Degree of
Doctor of Philosophy

School of Physics and Astronomy
Queen Mary, University of London
United Kingdom

June 2015

Statement of originality

I, Eleftherios Andritsos, confirm that the research included within this thesis is my own work or that where it has been carried out in collaboration with, or supported by others, that this is duly acknowledged below and my contribution indicated. Previously published material is also acknowledged below.

I attest that I have exercised reasonable care to ensure that the work is original, and does not to the best of my knowledge break any UK law, infringe any third party's copyright or other Intellectual Property Right, or contain any confidential material.

I accept that the College has the right to use plagiarism detection software to check the electronic version of the thesis.

I confirm that this thesis has not been previously submitted for the award of a degree by this or any other university.

The copyright of this thesis rests with the author and no quotation from it or information derived from it may be published without the prior written consent of the author.

.....

Eleftherios Andritsos

15 June 2015

Acknowledgements

First and foremost, I am grateful and I would like to thank my supervisors Prof Martin Dove and Dr Kostya Trachenko for their effort and support all these years. I am very fortunate to have had them as mentors and collaborators during these years. Without their insightful advice, this work would not have been possible.

I am particularly grateful to our collaborators Dr Franz Demmel and Dr Jon Taylor from the STFC Rutherford Appleton Laboratory. Both of them significantly involved in the experimental part of this work and helped me on experiments using their expertise.

I wish to acknowledge the generous help and support of Prof Michael Finnis and Prof Keith Refson, experts in theory and simulation of materials. Our fruitful conversations helped me understand and optimise the difficult process of developing interatomic potential parameters for my model.

Finally, I wish to thank Dr Anthony Phillips and Dr Evangelia Zarkadoula. They have been a constant source of answers and support during my PhD, especially during my first year.

Financial support during my PhD was provided by the School of Physics and Astronomy, Queen Mary University of London.
STFC funded the neutron scattering experiments at ISIS - STFC Rutherford Appleton Laboratory.

Abstract

The objective of this thesis is to provide a better understanding of the dynamics of liquids. Dynamics are related to important properties of materials and can predict their behaviour. Theories of dynamics often study only crystalline systems and they do not involve other structural phases. Therefore it is important to understand the correlation of dynamics of the crystalline, amorphous and liquid phase. Understanding disordered systems can be facilitated if we understand their correlation with crystalline systems.

In order to understand the connection on dynamics of the three phases I perform inelastic neutron scattering experiments and simulations. The inelastic neutron scattering is the best method to study high-frequency dynamics and obtain accurate results. I analyse and compare results from experiments and simulations for materials in their crystalline, amorphous and liquid phase. Further to the microstructure analysis of the three phases I analyse their local structure. I study possible memory effects in the short-range structure during phase changing and I discuss how these affect the dynamics of the system. Moreover I provide a theoretical explanation of the interatomic interactions in the local structure of crystals and I discuss the origin of the phonon−roton minimum that can be observed in phonon dispersion spectra of many materials. Finally I study macroscopic properties of the three phases on various materials, such as the heat capacity.

The analysis and conclusions I present in this thesis provide a pioneer way of studying dynamics and they contribute to better understanding of unsolved fundamental physics questions. In this thesis I address and try to answer two major questions. To what extent the dynamic properties of solids and liquids can be compared at the microscopic and macroscopic level and how much the local structure affects dynamics.

Contents

List of Figures

List of Tables

List of Abbreviations

α coefficient of thermal expansion

α_{NPT} coefficient of thermal expansion calculated under NPT Berendsen ensemble

α_{NVE} coefficient of thermal expansion calculated under NVE ensemble

β compressibility

Γ damping factor

γ Grüneisen parameter

θ_{D} Debye temperature

θ_E Einstein temperature

λ wavelength

τ relaxation time

ϕ interatomic energy

Φ flux

ω angular frequency

B bulk modulus

b scattering length

bcc body-centred cubic

C heat capacity

c isotropic elastic stiffness

C_{P} heat capacity under constant pressure

C_{V} heat capacity under constant volume

ccp cubic close-packed

DFT density functional theory

DHO damped harmonic oscillator

E Energy

EAM embedded atom model

F free energy

fcc face-centred cubic

GGA generalized gradient approximation

GO geometry optimisation

H enthalpy

hcp hexagonal close-packed

INS inelastic neutron scattering

IXS inelastic X-ray scattering

J force constant

K atomic force constant

k wave vector

k_B Boltzman's constant

K_E kinetic energy

LA longitudinal acoustic mode

LDA local-density approximation

LO longitudinal optic mode

MD molecular dynamics

NNA nearest neighbour atoms

p momentum

P_E potential energy

PBC periodic boundary conditions

PDF pair distribution function

Q Heat

Q scattering vector

R gas constant

RDF radial distribution function

S scattering intensity

T_c critical temperature

T_g glass transition temperature

TA transverse acoustic mode

TO transverse optic mode

TOF time of flight

U internal energy

v_{sound} speed of sound

VCF velocity correlation function

W work

1 Introduction and thesis outline

1.1 Introduction to the topic

Properties of a material are related to its structure and dynamics. Nowadays there is a good understanding of the similarities and distinctions between the solid structure, crystalline or amorphous, and the liquid structure at macroscopic level, while at the microscopic level the connection of the structure is clear up to a certain point. Classical theories of structure definition describe accurately the crystal and gas structure but they fail to describe the intermediate structures such as glasses and liquids.

Similar problem exists in theories of atomic dynamics of materials. Solids are dominated by structural processes and gasses by kinetic processes, while the intermediate structures are dominated by a combination of them. For the amorphous phase, due to the absence of specific theory, people usually discuss dynamics by either using the theory for crystals or the theory for gases. Due to the lack of accurate theoretical description of the amorphous and liquid state, it is very important to understand the connection between these two states and the well defined crystal phase, not only regarding atomic arrangements but also atomic motion.

The atoms in crystals follow a repeated pattern while for amorphous and liquid structures there is no periodicity. Standard theories for crystals fail to predict basic properties in the amorphous and liquid state. This problem is being treated by using various approximations during the calculation of the properties or by treating liquids as high temperature disordered solids or as high-density gases. These approximations do not treat the system realistically and there is need for new theory that will describe and predict more accurately the properties of the various structural phases. For the development of this theory it is important to initially understand the connection between the phases at the atomic level and study the atomic interactions and the atomic motion.

Experimental methods for studying the atomic motion involve inelastic scattering techniques such as Raman scattering, infra-red (IR) light scatter-

ing, inelastic X-ray scattering (IXS) and inelastic neutron scattering (INS). The first two techniques describe accurately the vibrations of atoms, are highly sensitive, cheap to use and easily accessible to most people, but they are limited to studying vibrations of a specific point in reciprocal space, the Brillouin zone centre. IXS and INS techniques surpass this problem but their main problem is that they require special equipment with high flux, especially the INS. This can be achieved only in few big centralised facilities in the world, such as the ISIS neutron spallation source in UK and it has high cost. Between all inelastic scattering techniques, INS gives much richer data and for higher wavelengths, and it is considered as the best technique to study dynamics.

Experiments on dynamics with the use of the previous techniques are quite common and there are many data in literature depicting atomic vibrations with collective excitation spectra of phonons. These spectra give information of the atomic motion and the properties of the structure but only recently scientists started comparing atomic dynamics spectra of solids and liquids in order to get a connection. More specifically, following previous observations Giordano and Monaco [1] performed IXS experiments on sodium and they compared excitation spectra of polycrystalline and liquid sodium and they found intriguing similarities between the two spectra. They analysed specific modes of vibration along various directions and they found a match between the two phases, something that they relate to short-range structure similarities of the two phases. They make a connection between phonon frequencies of crystal and liquid and between amorphous solid and liquid. They conclude by stating that the short-range order and the overall structural disorder leave both very distinct fingerprints on the dynamic properties of liquids, and that the dynamics of a liquid can be predicted once its structure and the dispersion curves of the corresponding crystal are known.

Something very interesting that can be extracted from Giordano's and Monaco's results is the pattern of collective excitation spectra of both polycrystalline and liquid case. For the longitudinal acoustic mode along the [1 1 1] direction we can see that after the initial linear increase and the first peak, the phonon dispersion curve exhibits a minimum. This minimum is

related to the roton minimum, which in the past it was associated to superfluid helium−4 (^{4}He). This minimum was initially mentioned by Landau in 1947 [2]. Landau initially predicted the formation of this minimum while later it was verified by experiments. In 1954, Feynman [3] gave a theoretical explanation on this minimum. The explanation both Landau and Feynman gave was related to superfluidity and the special state of helium−4, something that we know nowadays that it is not accurate since the minimum can be observed for many materials in results from IXS or INS experiments in both solid and liquid phase [4]. However, scientists have not proposed a sufficient theoretical explanation about the origin of this minimum so far.

Giordano's and Monaco's experiments give a good early indication about the connection between solid and liquid dynamics but without providing a theoretical explanation on the interatomic interactions. In this thesis, inspired by Giordano's and Monaco's results, I try to take further the previous conclusions and present results from INS experiments and INS simulations for various materials and try to explain the connection of the microstructure and the atomic dynamics in the various structural phases. I provide a detailed analysis of the local structure of each phase in order to understand better their connection.

Moreover I focus on the interatomic interactions in the local structure and I try to provide a sufficient explanation of the formation of the phonon−roton minimum and its origin. Although I describe the interatomic interactions for a simple crystalline structure, this explanation can extend to more complex solid structures and liquids. This is clear from the result analysis in all chapters due to the high similarity of dynamics of solids and the corresponding liquids. This method provides a complete approach that includes theory and results from experiments and simulations, something that has not been implemented before for studies of atomic dynamics. Further to the study of the microstructure I try to correlate the solid and liquid state at the macroscopic level, where I focus on thermodynamics and the calculation of heat capacity for various materials.

The material I used for the INS experiments is pure polycrystalline barium in beads form. The main criterion of choosing barium is its physical

properties. Barium belongs to the family of alkaline earth metals and it exhibits similar properties, such as crystalline structure and metallic properties, as sodium. To obtain rich and high quality data I performed INS instead of IXS. The INS experiments took place at ISIS facilities in Oxfordshire UK [5], where I used the MARI instrument. Experiments at ISIS are performed with pulsed neutron and muon sources. Neutron scattering is a unique research and analysis technique, non destructive, for exploring the structure and dynamics of materials at the atomic level. Barium due to its metallic well defined structure and high atomic number has a high neutron scattering factor and it provides clear results during INS experiments at moderate temperatures.

Further to the experimental INS I performed INS simulations. Most of the materials I used for computational studies are metals with similar properties with barium, in order to be able to compare experimental and computational results. To simulate the structure for the various phases I performed molecular dynamics (MD) simulations. In MD simulations the equations of motion, force equal to mass times acceleration, are solved numerically providing data for the new positions of every atom in a system at any time. MD simulations require only the knowledge of the initial positioning of the atoms in a system and the interatomic potential that describes the interaction between the atoms. Most of the required initial data can be found in crystallographic databases, interatomic potential databases or published scientific research papers.

After the preparation of the configuration in the crystalline, amorphous or liquid phase I used the calculated data for two purposes. Initially, I calculated the collective excitations phonon frequencies along all directions for various materials and I was able to represent collective excitation spectra, similarly to the experimental procedure. Secondly, I performed detailed analysis of the local microstructure. This analysis involves detailed information of the local population and the local order of the three phases in order to identify similarities.

Classical MD simulations of barium are not feasible since there is lack of interatomic potential in literature describing interactions of barium atoms.

Since the 1960s the developing of interatomic potentials gained a lot of growth, since computational research started increasing. Nowadays there are accurate models and potentials describing the interactions between most of elements or the interactions between molecules, but there is no model describing barium atoms. In order to perform MD simulations for barium I tried to develop a new interatomic potential based in the well known Finnis−Sinclair model.

Developing an interatomic potential requires precise information of the interatomic interactions and the system properties. The most common technique to obtain high quality data for the structure is the density functional theory (DFT). This technique gives high accuracy data, needed for describing the parameters of an interatomic potential. All data need to be fitted to the potential functions and parameters in order to describe accurately the physical properties of the system and the atomic motion and interaction.

The previously mentioned techniques study the connection between the solid and liquid phase at the atomic level. To support further this connection I studied thermodynamical properties of various materials and I focused on the heat capacity (C) of materials and the coefficient of thermal expansion (α). Heat capacity of matter is a theoretically and experimentally very well studied property. There are various theories explaining and predicting heat capacity of crystals and gases and there are numerous data from experiments on solids, liquids and gasses showing that its value changes depending on the structural phase. Yet, there is no theory dedicated in predicting heat capacity of liquids.

An interesting approach is a theory for the heat capacity, derived from the solid phase [6]. The authors predict the anharmonic effects in heat capacity under constant volume (C_{V}) by using only one parameter the coefficient of thermal expansion. In my research I extend this theory in order to study the heat capacity of various simple crystalline, amorphous, and liquid materials. To verify my theory and examine if this theory is consistent with the various phases of matter I perform MD simulations on various materials and I use the coefficient of thermal expansion as the comparison parameter. While heat capacity changes for the various conditions, the coefficient of thermal expan-

sion is characteristic for each material and it gives a better understanding of the validity of my theory.

By the end of this thesis, I will present the relation of dynamics of solids and liquids. The understanding of dynamics at the microscopic level in combination with the understanding of dynamics at the macroscopical level, provide a complete estimation of the connection between the three phases. The reader will be able to understand to what extent dynamic properties of liquids and solids can be compared, to what extend the dynamics are determined by the short or long-range order and what is the origin of the phonon−roton minimum. The importance of this topic is high since it tries to give answers to fundamental physics' questions and it provides a better understanding for basic physical properties.

1.2 Thesis outline

Every chapter of this thesis deals with different topic or method. All chapters are supported by the general theory section but they also include their own specific theory. Every theory, method and software I used are explained, described and discussed in details in each chapter. All the topics of every chapter are connected and they complement each other.

In chapter 2, I discuss structural and dynamics similarities and distinctions of crystalline, amorphous and liquid materials. I appose the structural connection between crystals and glasses, glasses and liquids and the differences in atomic motion of solids and liquids. I discuss modes of vibration in the various directions and explain the phonon theory for solids and liquids. Finally I introduce scattering techniques, focusing more in neutron scattering.

In chapter 3, I give details of the INS experiments on barium. I describe the INS experiments and how I use the results to discuss dynamics. I give details of the instrument and the technique I used, the material, the procedure I followed and the data collection and analysis. I explain in details how I used software to analyse, refine, fit and visualise data. Finally, I present and discuss the experimental results.

Chapter 4 is dedicated to the computational understanding of research regarding dynamics and structure. I discuss classical and quantum MD simulations of various materials, the theoretical background and the procedure. Furthermore I describe the procedure for performing INS simulations and calculating phonon frequencies, how I analysed the local structure and how I developed the parameters for the interatomic potential of barium.

In chapter 5, I discuss the already existed theories of roton minimum and I provide a theoretical explanation on the origin of the phonon−roton minimum. I explain the origin of the minimum by discussing the interactions of the local order in a bcc material. Finally I compare the theoretical results with results from experiments and simulations.

In chapter 6, I focus on thermodynamics and the prediction of heat capacity. I describe and extend the current theory and present MD simulations and results from various materials. I discuss in details about all materials, methods and conditions used in the simulations. I explain the predictive power of the theory and I discuss results of solids and liquids and the connection between them.

In chapter 7, I summarise the theory and the results from all chapters and I discuss the conclusions.

2 Theoretical approach to crystalline, amorphous and liquid matter

The theory I will present in this chapter is related to the presented work in the rest of chapters of this thesis. In this chapter I will discuss some basic definitions of structure and dynamics. I will discuss crystals, glasses and liquids, their structural and dynamical properties and the relationship between these three phases. I will give a short general description on the structure of the three phases and some basic information on related crystallographic properties. Then I will describe the theory of dynamics of matter and modes of vibration and I will discuss the phonon theory and general principles of scattering techniques, focusing on the INS technique which I used for both experimental and computational studies.

2.1 Similarities and distinctions in structure

2.1.1 Defining the structure

Distinctions of structure of the various phases of matter are well known and well defined especially for solids and gasses and less for liquids. Solids can be separated in crystalline and amorphous structures. The crystalline state is the lowest energy state for elements and compounds. Crystalline materials have a repeating structure, the crystal lattice, that is described by the basis vectors. In D dimensions there are D lattice vectors and for the realistic 3-dimensional case the lattice vector, which describes the repeated unit of the crystal, can be defined as

$$\mathbf{r}_{xyz} = x\mathbf{a} + y\mathbf{b} + z\mathbf{c} \tag{2.1}$$

where x, y, z take integer values and $\mathbf{a}$, $\mathbf{b}$, $\mathbf{c}$ represent the basis vectors. Elements of the lattice vectors are the cell vectors of an atom that point towards the unit cell in which that atom is located. The unit cell and the lattice share the same basis vectors.

The formation of the structure depends on the different elements in a

molecule, the type of bonding and the atmospheric conditions. The crystal structure of a material is often described in terms of its unit cell. The unit cell is a spatial arrangement of atoms which is piled in 3-dimensional space to describe the crystal. The unit cell is given by its lattice parameters, the length of the cell edges and the angles between them, while the positions of the atoms inside the unit cell are described by the set of atomic positions measured from a lattice point. The unit cell can be either primitive or conventional. The primitive unit cell is defined with vectors that represent the minimum volume or same size volume, regarding the volume that occupies in space. The conventional unit cell might represent a cell of larger volume but the cell exhibits the symmetry of the lattice in a better understood way.

Amorphous materials or glasses are disordered solids. They are disordered solids in the sense that in this structure there is no periodicity or long range order, although there are indications that the local structure may have short range order similar to the crystalline [7–9]. Despite the fact of possible similarity in the short range order with crystals we can not use similar terms to describe atomic coordinates for glasses, such as unit cell and symmetry. Glasses are also described as frozen liquids, with fixed atoms in specific positions without periodicity. Traditionally the glassy state is treated as solid since many scientists approach the topic by studying the structural properties of glasses [10–15], while other treat it as a liquid by studying thermodynamical properties of glasses [6, 16–18].

To describe glasses it makes more sense to describe the distance and the angle between neighbour atoms and then compare them with the crystal structure, where distance and angle are well defined. The calculation of the atomic distances of neighbour atoms can be done with the pair distribution function (PDF) $g(r)$. This gives the probability of finding a pair of atoms at specific distance. For two atom types A and B, the number of atoms of type B that can be found in a distance dr, of radius r, is

$$n_{\mathrm{AB}}(r) = 4\pi r^2 \rho_{\mathrm{B}} g_{\mathrm{AB}}(r)\mathrm{d}r \tag{2.2}$$

where ρ_{B} is the density of atoms B or the number of atoms per unit volume.

The PDF holds information about the the interatomic distances within the molecules and between the molecules, so perhaps the equation 2.2 can be understood easier for well defined structures as crystals. At distances shorter than the interatomic distance the $g(r)$ will be zero since there will be no neighbouring atoms at this distance. At very large distances the $g(r)$ will be equal to 1 since at the long range the pair of atoms depends only in density ρ_B and not the atomic arrangement. In chapter 4 I will analyse the short-range structure of crystals, glasses and liquids and I will present and explain results from PDF analysis.

2.1.2 Reciprocal lattice

The reciprocal lattice gives a mathematical representation of planes of atoms in a crystal and is the Fourier transformation of the real-space lattice and it applies in theories such as lattice dynamics, electrons in crystals and in diffraction and scattering. The reciprocal space vector can be defined as

$$\mathbf{d}^*_{hkl} = h\mathbf{a}^* + k\mathbf{b}^* + l\mathbf{c}^* \tag{2.3}$$

$\mathbf{a}^*$, $\mathbf{b}^*$, $\mathbf{c}^*$ are the basis vectors of the new lattice h, k, l are integers and called Miller indices. The length of the reciprocal space vectors is the inverse of the spacing of the corresponding planes in real-space lattice. In reciprocal space there is a set of vectors, the wave vectors ($\mathbf{k}$), which each set is normal to a pair of basis vectors of the crystal lattice and characterise the wavelength and the direction of the travelling space. The wave vector is related to the wavelength (λ) as $|\mathbf{k}| = 2\pi/\lambda$. A travelling wave $\mathbf{u}$ at any position r can be described as

$$\mathbf{u}(r) = u_0 \exp(i\mathbf{k}r) \tag{2.4}$$

where $\mathbf{k}$ is the wave vector and u_0 is the amplitude.

The wave vector and the reciprocal lattice are related to the Brillouin zone. The Brillouin zone describes a zone that is in between two consecutive reciprocal lattice points. It is the final point of the first reciprocal lattice point and the last of the second reciprocal lattice point. This is the area

described at the limit from $-\mathbf{k}$ and $+\mathbf{k}$. The Brillouin zone boundary is denoted as $\mathbf{k}_{ZB}$ and the partial derivative of a function with respect to wave vector in the $\mathbf{k}_{ZB}$ limit is equal to zero. The volume of the Brillouin zone is equal to the reciprocal unit cell volume.

A common representation of the wave vector is with the use of the reduced wave vector. This is the wave vector normalised by the magnitude of the first reciprocal space vector that lie along the direction of the wave vector. For the 1-dimension case, the Brillouin boundaries lie between the limits of $-\pi/\mathrm{a} < k < \pi/\mathrm{a}$, where a is the reciprocal space vector. The reduced wave vector of the Brillouin zone is represented with value 1/2, which is obtained by dividing the wave vector a/2 by the reciprocal space vector a. For the 3-dimension case, the reduced wave vector is represented as in equation 2.1 with x, y, z, but now x, y, z are not integers. This approach is quite common especially in scattering techniques for the representation of dispersion curves. I will use the reduced wave vector for the analysis of my results in the next chapters. The reciprocal space, Brillouin zone and the reduced wave vector are defined only for crystal structures but they are being used in various calculations and techniques such as neutron scattering techniques for the representation of atomic positioning in space regardless the structural phase of the material.

2.1.3 Long and short-range order

A material is crystalline if it is described by long-range periodic order and one or more atoms periodically repeat themselves in the three dimensional space. Theoretical or computational studies on crystals involve approximations such that crystals are perfect or they are treated as bulk materials that extend spatially from minus infinity to plus infinity. In reality, crystalline materials might be imperfect or might be governed by various defects or dislocations. Defects and dislocations interrupt the order in structure and affect the dynamics of materials. If these defects extend to larger scale, a material can be categorised as amorphous material.

The amorphous state represents an intermediate state between the liquid

and crystal state. Amorphous materials lack of order over large scale but often they have a short or medium-range order, where short-range is the distance between the nearest neighbour atoms and medium-range order is the distance between one atom and several neighbour atoms. Its structure is characteristic of the instantaneous structure of a liquid with lack of long-range order. However, the atoms are constrained to vibrate around their disordered equilibrium position so that their dynamics is characteristic of a solid. An amorphous material usually exists under strong constraints, such the interatomic interactions, that help the atoms in the material to form a specific amorphous structure depended on each system.

Liquids, similarly to glasses, are characterised as structures with absence of long-range order. They have similar atomic density with the corresponding solid phase but they are much less viscous and they have bigger self-diffusion coefficient. In comparison with the corresponding gas state, liquids have much higher density, much lower self-diffusion coefficient and same order of magnitude viscosity.

In the figure 1, I present a system of NaCl in the crystalline, amorphous, liquid and gas state, after performing classical molecular dynamics simulations for several ps of atomic movement. The green spheres represent the chloride and the yellow spheres the sodium. The bonds that connect the atoms represent the interatomic distance for the NaCl crystal structure. As we can see, the crystalline structure has a well defined structure, while the glass, liquid and gas do not. The amorphous structure seems to have absence of long-range order, as it is the case with liquids and gases. As I will describe in the following chapters, despite the absence of long-range order, amorphous and liquid materials hold their short-range order.

In the next section I will briefly discuss the lattice dynamics of the crystalline, amorphous and liquid state. For a more thorough review on dynamics of materials the reader is refereed to literature [19, 20].

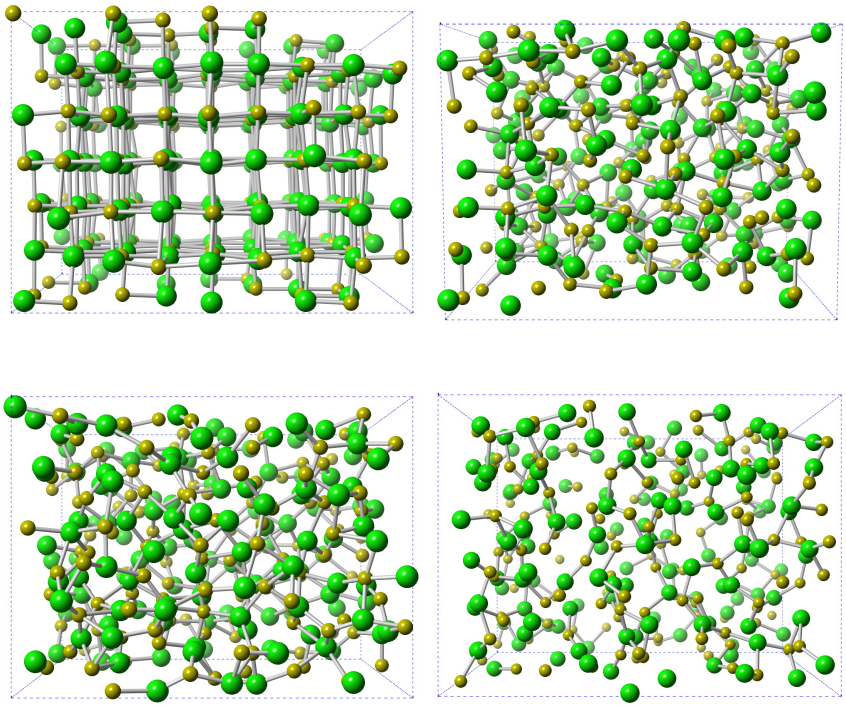

Figure 1: MD simulations of 288 NaCl atoms in various phases: crystal (upper left), amorphous (upper right), liquid (lower left) and gas (lower right).

2.2 Similarities and distinctions in dynamics

Lattice dynamics is a method commonly used for the calculation of the free energy, thermal properties, optical properties, dielectric properties and other properties of a material and it refers to atomic vibrations or phonons, where phonons are defined as the quanta of the atomic motion. Atoms in a solid constantly oscillate around their equilibrium positions with an energy which is governed by the temperature of the solid. In liquids the atoms initially vibrate around their equilibrium position and then they move to another position where they repeat the same procedure.

The lattice energy is the potential energy of the system while the atoms are in rest. In classical theory atoms are in complete rest at zero temperature while in quantum mechanics theory atoms never rest and they are in constant

vibration. In both cases, the potential energy between two atoms i and j with interaction $\phi_{ij}(r_{ij})$, at distance r between the atoms is given as

$$U = \sum_{ij} \phi_{ij}(r_{ij}) \tag{2.5}$$

and can be used for the calculation of equilibrium structure, for energy calculations and for calculations of energy derivatives. The Gibbs free energy determines the stability of a crystal structure, its physical properties and its behaviour and is defined as $G = U + PV - TS$, where U is the internal energy, P is the pressure, V is the volume, T is the temperature and S is the entropy. The entropy of a system has always positive value and it arises from the disorder of atoms and the vibration of atoms.

The atomic vibrations in a periodic lattice give rise to a wave propagation with energy, which significantly affect the heat capacity and the thermal conductivity of solids. Initially Dulong and Petit [21] discovered experimentally that the heat capacity per mole of any crystal is 3R, where R is the gas constant. Although this law was correct for most elements at intermediate temperatures, it failed to predict heat capacity at lower temperatures. Later, it was Einstein who gave a quantum explanation for heat capacity. He assumed that atoms vibrate at fixed frequencies and they behave like independent quantum oscillators. This theory did not describe properly the decrease of specific heat with decreasing temperature. After Einstein, initially Debye and at similar period Born and von Karman, explained that the atoms are not behaving as independent oscillators and the vibration of one atom affects the other atoms, because of the strong binding between different atoms in a crystal. Today Debye's theory is proved to work for some specific cases such as most metals, but not for more complicated materials.

2.2.1 Adiabatic approximation

The theory of the dynamical properties can be treated by two approximations. The first approximation is the adiabatic approximation, known as Born−Oppenheimer approximation, which allows to separate the elec-

tronic dynamics from the corresponding nuclear dynamics. The second is the harmonic approximation which is based on the hypothesis of small nuclear oscillations around the equilibrium positions [22].

The idea of the adiabatic approximation is that atomic nuclei moves much slower than electrons, because of the bigger mass. In this picture the nuclei are steady and only electrons are moving in respect of nuclei. While nuclei are moving the electrons follow the nuclear motion adiabatically, in the sense that the electronic state follows a smooth variation. The Born−Oppenheimer approximation is rather a good approximation since it depends on the mass of the electrons being much smaller than the masses of the nuclei, something that is true, and it also depends on the velocity of the nuclei being low compared to the velocity of the electrons, something that is very often true. The consequence of this approximation is that properties for any system are restricted to situations where electrons follow the motion of the nuclei adiabatically and situations where electronic excitations are important are excluded. Within the Born−Oppenheimer approximation the total energy of the system is a function of the positions of the nuclei, independent of their velocities or history. With this assumption it is possible to derive interatomic potentials and interatomic forces which are functions only of the nuclear positions.

The vibrational dynamics of a system of N atoms in positions r is usually described in adiabatic approximation by a Hamiltonian equation of the form

$$H = \frac{1}{2} \sum_{(xyz)i} m_i \dot{r}^2_{(xyz)i} + V(r_1, ..., r_N) \tag{2.6}$$

where (xyz) indicate Cartesian coordinates, m_i is the mass of the ith atom and $V\ (r_1, \ldots\ , r_N)$ is the N body potential which describes in the interactions of all atoms in the system. This approximation is good only if the excitation energy for the nuclear vibrations is much less than that for the electrons, thus for closed shells. On the other hand, the adiabatic approximation can not be applied for conductive solids such as metals [23], where the conduction band implies a large number of electronic states with small energy gap. More details on this approximation can be found in literature [24, 25].

In the harmonic approximation the forces in a well defined structure, as in crystals, are proportional to the atomic displacement and they are treated as harmonic. In this way the atomic motion behaves as simple harmonic motion. The use of the harmonic approximation overpasses the anharmonicity that exists in real systems and it can simplify the solution of the equation 2.6. Anharmonicity refers to the deviation of a system to behave as a harmonic oscillator, so not to have harmonic motion. In chapter 6, I give an extended review on thermodynamic properties of solids and liquids, discussing the harmonic and anharmonic case and thermodynamic implications.

2.2.2 Modes of vibration

One of the challenges of condensed matter physics is the microscopic understanding of macroscopic phenomena. The atoms of a system, solid or liquid, are constantly in motion. In solids the atoms vibrate around their equilibrium position. In a perfect crystal the vibrations are simplified by using lattice periodicity and with the Bloch theorem the study of vibrations can be transferred to one unit cell. Each vibration is described by an angular frequency (ω) that describe the periodicity of the displacement and the wave vector ($\mathbf{k}$) that give the direction of the displacement. The last two terms are connected with the speed of sound (v_{sound}) as

$$\omega = v_{\text{sound}} k \tag{2.7}$$

The vibrational eigenvectors in a crystal can be described with plane waves defined by a $\mathbf{k}$ vector lying in the first Brillouin zone.

A solid described as a system of $3N$ total degrees of freedom, where N is the total number of atoms in the system, it has 3 coordinates to describe the translational motion around the centre of mass, the translational degrees of freedom, 3 coordinates to describe the rotational motion in non-linear molecules and only 2 rotational degrees of freedom for linear molecules and the remaining coordinates are used to describe vibrational motion. A non-linear molecule has $3N$ - 6 vibrational degrees of freedom whereas a linear molecule has $3N$ - 5 degrees of freedom. A system with $3N$ vibrational

degrees of freedom has $3N$ independent oscillators, something that is easily derived from the example of a harmonic oscillator. Each of the independent oscillators corresponds to a normal mode of vibration [24].

Normal modes are used to describe the different vibrational motions in molecules or crystals. Each mode is characterised by a different type of motion and each mode has a certain symmetry associated with it. The number of normal modes is equal to the number of degrees of freedom of the crystal in its Cartesian representation. A normal mode of an oscillating system is a pattern of motion in which all parts of the system move sinusoidally with the same frequency and with a fixed phase relation, as in a harmonic oscillator. In general, a normal mode is an independent motion of atoms in a molecule that occurs without causing movement to any of the other modes [26]. Normal modes, as implied by their name, are orthogonal to each other.

The plot of the frequency of each mode of vibration ω as function of the wave vector is the dispersion curve. Every curve is related to each mode and is known as the branch of a dispersion curve. When $\mathbf{k}$ tends to zero and the ω tends to zero, the corresponding solutions are the ones of sound waves and the corresponding modes are called acoustic modes. The acoustic modes are vibrations for small $\mathbf{k}$ in which the unit cell moves in phase and they tend to zero at the Γ point [0 0 0]. For a system of N atoms and D dimensions there are ND modes of vibration for each wave vector. D is equal to the number of the acoustic modes.

Vibrations of atoms of different phase are called the optic modes. These modes have non-zero frequency when $\mathbf{k}$ is zero or at any $\mathbf{k}$. These modes are called optic, because if two atoms have opposite charge, their relative motions correspond to the motions that would be induced by the passage of an electromagnetic wave of optical frequencies. The frequencies of optic modes are usually within the infrared region of the electromagnetic spectrum [27].

Another distinction of modes can be made when the crystal consists of different atoms, such as molecules or polyatomic ions. If there are Z molecules in the unit cell and N atoms, then out of the $3N$ branches of the dispersion curves, the $6Z$ lowest frequencies represent the external modes, and corre-

spond to the motion of the different atoms. The remaining $3N$ - $6Z$ modes are the internal modes. The 3 acoustic modes belong to the set of external modes [28].

As I mentioned earlier, for each wave vector there are two orthogonal perpendicular directions. Because of that, there will be two acoustic branches with different dispersion curves determined by new force constants, where their corresponding vibrations are called transverse acoustic mode (TA). The acoustic branches parallel to the wave vector have corresponding vibrational motion parallel to the wave vector, the longitudinal acoustic mode (LA). The symmetry of every system related to axis in the direction of the wave vector, highly affects the interatomic forces of the system. For the optic modes similarly there are two modes defined as the transverse optic mode (TO) and the longitudinal optic mode (LO).

In crystalline systems, the approximation of crystal translational invariance reduces the problem of using microscopic phenomena to understand macroscopic phenomena to that of a relatively small number of atoms. Because of this approximation, problems like atomic motions in crystals can be described in terms of collective vibrations around equilibrium positions and these microscopic vibrational dynamics can be linked to a large class of macroscopic phenomena [29]. The harmonic theory of atomic vibrations does not predict the damping of vibrational excitations that is observed for glasses and liquids, something that is due to higher order effects. That means that the previous approach for crystals can not be extended to glasses or liquids. For the latter, the periodicity that is described for crystals is lost and as long as the periodicity does not exist there are qualitative differences with the corresponding crystal in dynamics [8, 29, 30].

To describe the vibrational properties in crystals as well as in disordered systems we can use the vibrational density of states, or phonon density of states, or the normal mode density. This is defined as

$$g(\omega) = \sum_{\mathbf{k}} \delta(\omega - \omega_{\mathbf{k}}) \tag{2.8}$$

where g(ω) is the number of states lying between ω and $\omega + \mathrm{d}\omega$. For crystals

the sum over **k** is over all branches and covers the first Brillouin zone. The vibrational density of states represents the natural link between a microscopic description of a solid and its macroscopic properties. By knowing the $g(\omega)$ someone can derive thermodynamic properties such as the heat capacity and the thermal conductivity [31].

It is known from experiments that at frequencies with small wavelength, sound propagates only in crystals and in their corresponding glasses. At frequencies with large wavelength a glass appears as an elastic continuum medium and the disorder does not effect the vibrational dynamics. Long wavelength acoustic mode vibrations, hence low frequencies, can be well described as delocalised excitations which correspond to the sound waves and have Debye density of states [32], which means that there are $3N$ vibrations. In this case the phonon density is given by

$$g(\omega) = \frac{3\omega^2}{\omega_{\mathrm{D}}^3} \tag{2.9}$$

where ω_{D} is the Debye frequency and it represents the highest frequency for the acoustic waves. As **k** approaches zero the vibrational excitations show a linear propagation of the acoustic waves. At frequencies with small wavelength (large **k**) the vibrational excitations of glasses and liquids are observed for up to specific wavelength sizes of one unit cell. After this limit the atomic motion lose its oriented propagation and more complex and broader pattern of vibrations appears.

2.2.3 Bose−Einstein distribution

Following the previous discussions, we understand the lattice as a collection of harmonic oscillators with one oscillator for each of the lattice directions. Every discrete harmonic oscillator describes an energy spectrum that atoms are allowed to vibrate. Phonons obey the Bose−Einstein statistics and represent the simplest elementary excitation for a material in the solid

or liquid phase. The energy of each normal mode is given as

$$E(\mathbf{k},\nu) = \left(n(\omega) + \frac{1}{2}\right)\hbar\omega_j(\mathbf{k},\nu) \tag{2.10}$$

where $\mathbf{k}$ is the wave vector of the travelling wave ν, n refers to a single phonon mode, ω is the angular frequency and $\hbar = h/2\pi$ where h is Planck's constant.

Phonons are bosons, and in that sense there is no limit to the number of phonons that can be present in each normal mode and are free to be distributed in these modes. The Bose−Einstein distribution, or Planck distribution for phonons over the time period is given as

$$n(\omega,T) = \frac{1}{\exp\left[E(\mathbf{k},\nu)/\mathrm{k}_B T\right] - 1} = \left(\exp\left[\frac{\hbar\omega_j(\mathbf{k},\nu)}{\mathrm{k}_B T}\right] - 1\right) \tag{2.11}$$

where n is the phonon occupancy at temperature T, $E(\mathbf{k},\nu)$ is the energy of a coupled mode, and k_B is Boltzman's constant. At the classical limit where $\mathrm{k}_B T > \hbar\omega$ the phonon distribution is given as

$$n(\omega) = \mathrm{k_B}T/\hbar\omega(\mathbf{k},\nu) \tag{2.12}$$

This defines the equilibrium phonon occupancy at a specific temperature. As I discussed in the introduction, phonons and phonon distribution can be detected with scattering techniques, with the most accurate technique to be the neutron scattering.

2.3 Neutron scattering

Scattering techniques reveal information about the crystal structure, chemical composition and physical properties of materials. Scattering methods and more specifically neutron scattering have been extensively studied and analysed in the past in various textbooks such as [33–37] where we can find more details. In this section I try to provide some basic information on neutron scattering, something that will be useful for future chapters where I analyse results from INS experiments and simulations.

Scattering techniques are based on the observation of the scattered inten-

sity of a beam hitting a sample as a function of incident and scattered angle, polarisation, and wavelength or energy. For example, an electron beam will be electrostatically repelled by the orbital electrons of the atoms so it will penetrate the sample only for few micrometers, making this method good only for studying surfaces. X-rays penetrate a material deeper than electrons. The orbital electrons interact less because X-rays do not have charge, and although they are electromagnetic waves and they consist of oscillating electric and magnetic fields, the charge of the orbital electrons interact less strong with these fields. On the other hand neutrons are neutral particles and they are not affected by orbital electrons. They interact with the nucleus of the atom with a strong nuclear force. This makes neutron scattering very powerful for studying bulk materials. Furthermore, with neutron scattering one can study all the phonon branches and create complete dispersion curves for phonons with non-zero wave vector.

In neutron scattering, neutrons can be described by using their mass and their speed. According to Planck's hypothesis the energy of an oscillation with frequency ν is given as

$$E = h\nu \tag{2.13}$$

According to de Broglie h is connected with a particle's momentum ($\mathbf{p}$) and wavelength (λ) as $|\mathbf{p}| = h/\lambda$. Neutron's kinetic energy is given as

$$E_n = \frac{1}{2} m_n v^2 \tag{2.14}$$

where m_n is the neutron mass and v the neutron speed. By involving λ, the equation 2.14 changes to

$$E_n = \frac{h^2}{2m_n\lambda^2} \tag{2.15}$$

and by introducing the wave vector in momentum, $\mathbf{p} = \hbar\mathbf{k}$, the energy changes to

$$E_n = \frac{\hbar^2|\mathbf{k}|^2}{2m_n} \tag{2.16}$$

The temperature of neutrons is quite important. The speed of neutrons is highly related to temperature and the average neutron speed is higher at

high temperatures. The relationship between energy and temperature per neutron is given with a simplified equation

$$E = \mathrm{k_B}T \tag{2.17}$$

By changing the temperature during scattering we can adjust the speed and energy of neutrons.

For better understanding of how X-ray and neutron scattering are compared it is worth mentioning that X-rays frequency is $\nu = c/\lambda$, where c is the speed of light. Then the equation 2.13 transforms to

$$E = \frac{hc}{\lambda} \tag{2.18}$$

If we compare the equation 2.18 with the equation 2.15 for the same wavelength and we replace with numerical values the speed of light and the neutron's mass, we can see that energy of neutrons is about 6.6 times higher than the X-ray's energy.

Neutrons are scattered from any material with scattering intensity (S) as function of the scattering vector ($\mathbf{Q}$) and the angular frequency (ω) or the energy (E). X-rays are highly dependent on the magnitude of $\mathbf{Q}$ as the X-ray wavelength is of the same size as the atom's radius. For neutrons, the interaction potential is at smaller length scales which are shorter than the neutron's beam wavelength [36]. This explains why the neutron scattering intensity is not related to $\mathbf{Q}$. The scattering length (b), or scattering factor, determines the amplitude of the scattered neutron beam and is related to the intensity of the interaction between the neutron and the atomic nucleus and is expressed with the cross sectional area's equation $\sigma = 4\pi b^2$. The scattering length is a characteristic value for each element or isotope and it can take either a positive or negative value. Between the value of b and the atomic number there is no correlation.

2.3.1 Elastic scattering

In neutron scattering a beam of neutrons interacts with the atomic nuclei. This beam has specific initial energy (E_i) and initial wavevector ($\mathbf{k}_i$). After the scattering the beam has final energy (E_f) and final wavevector ($\mathbf{k}_f$). The difference between the two wave vectors is the scattering vector ($\mathbf{Q}$) and is equal to

$$\mathbf{Q} = \mathbf{k}_i - \mathbf{k}_f \tag{2.19}$$

where $\mathbf{k} = 2\pi/\lambda$, and the difference between the two energies is equal to

$$E_i - E_f = \hbar(\omega_i - \omega_f) \tag{2.20}$$

With the (2.19) we can redefine the phonon energy and the (2.16) can change as

$$E_n = \frac{\hbar^2 |\mathbf{Q}|^2}{2m_n} \tag{2.21}$$

If there is no loss of energy or change in the wavelength then the scattering is elastic. Neutrons which have come into thermal equilibrium with matter at about room temperature have energies of the same order of magnitude as phonons.

The wavelength associated with a beam of neutrons all having the same energy is of the same order of magnitude as interatomic distances and the beam will be diffracted by a crystal. Most of the intensity is diffracted in accordance with Bragg's law $\lambda = 2d\sin\theta$, where d is the interatomic distance and θ is the scattering angle. Although the wavelength does not change, the neutron beam is diffracted in other directions by the thermally excited travelling waves in the crystal and exchanges energy with them in the process, which is directly proportional to frequency. For the elastic case $|\mathbf{k}_i| = |\mathbf{k}_f| = 2\pi/\lambda$ so

$$|\mathbf{Q}| = \frac{4\pi\sin\theta}{\lambda} \tag{2.22}$$

This result is represented in figure 2 where the drawn triangle is an isosceles triangle with the two equal sides being of length $2\pi/\lambda$. Consequently by measuring the change in direction and in energy of the scattered neutrons it

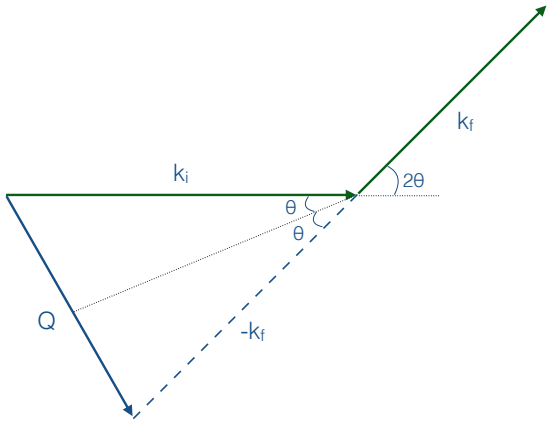

Figure 2: Wave vector representation for elastic scattering.

is possible to get more detailed information about the frequencies and polarisation properties of the lattice vibrations than by any other experimental method.

2.3.2 Geometry of scattering

Experimentally the neutron beam scatters from the sample and reaches various detectors around the sample. This allows the definition of scattering angle and the interatomic spacing. For the realistic definition of the direction of the neutrons after they deflect from the sample we need to define a second angle ϕ, and in this way we can describe the various directions with spherical polar coordinates 2θ and ϕ. The rate of incident neutrons per time is defined as flux (Φ). This rate of arrival in the direction of 2θ and ϕ into a detector at a sample that subtends a small solid angle $\mathrm{d}\Omega$ is known as the partial differential cross section and is defined as

$$\frac{\mathrm{d}^2\sigma}{\mathrm{d}\Omega\, dE_f} = \frac{n_n}{\Phi\, \mathrm{d}\,\Omega \mathrm{d}E_f} \tag{2.23}$$

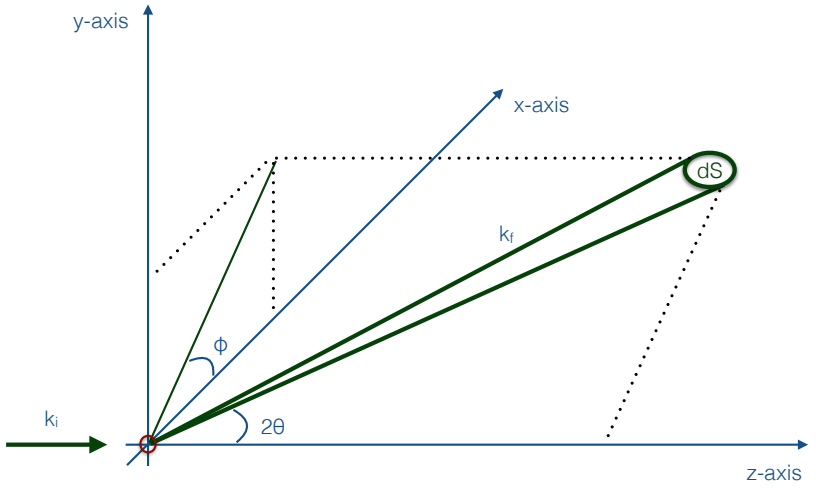

Figure 3: Neutron scattering geometry representation.

where n_n is the number of scattered neutrons per time in $\mathrm{d}\Omega$ and $\mathrm{d}\Omega$ is defined as $d\Omega = \mathrm{d}A/r^2$ with $\mathrm{d}A$ to be a very small area in the detector and r is the distance. The equation 2.23 is related to the scattering function $S(\mathbf{Q}, \omega)$ and is always proportional to the differential cross section. The figure 3 is a graphical representation of the experimental geometry in neutron scattering experiments. The incident beam has the same direction as $\mathbf{k}_i$ till it reaches the sample, in the beginning of the three axis. Then neutrons follow the $\mathbf{k}_f$ direction till they reach the detectors. The dark green dotted lines in figure 3 represent the angle $\mathrm{d}\Omega$ in 3 dimensions.

The neutron scattering function is defined as

$$S(\mathbf{Q}, \omega) = \int \mathbf{F}(\mathbf{Q}, t) e^{-i\omega t} \mathrm{d}t \tag{2.24}$$

where $\mathbf{F}(\mathbf{Q}, t)$ is the intermediate scattering function, and is given as

$$\mathbf{F}(\mathbf{Q}, t) = \langle \rho(\mathbf{Q}, t) \rho(-\mathbf{Q}, 0) \rangle \tag{2.25}$$

where $\rho(\mathbf{Q}, t)$ is the density function of particles in the sample at time t, which is the Fourier transform of the instant nuclear density, where the instant position of a nucleus j $(\mathbf{r}_j(t))$ is the sum of the equilibrium position of the

nucleus ($\mathbf{R}_j$) plus the displacement at a specific time $u_j(t)$. The density function is defined as

$$\rho(\mathbf{Q},t) = \sum_j b_j e^{i\mathbf{Q}\mathbf{r}_j(t)} \tag{2.26}$$

By combining (2.24), (2.25) and (2.26) we can define the full equation of scattering function

$$S(\mathbf{Q},\omega) = \sum_{i,j} \left\{ b_i b_j e^{i\mathbf{Q}[r_i - r_j]}\mathrm{x} \int e^{i\mathbf{Q}[\mathbf{u}_i(t) - \mathbf{u}_j(0)]} e^{-i\omega t} \mathrm{d}t \right\} \tag{2.27}$$

2.3.3 Inelastic scattering

In contrast to elastic scattering where the energy of the incident neutrons is the same after the deflection with the sample, in inelastic scattering there is loss or gain of neutron energy that comes from a phonon creation or extinction respectively. The energy is transferred to the sample and it changes to motion (rotation, translation, vibration) for atoms. This is very important for studies on dynamics of materials and lattice vibrations through phonons, and when there is need for thermal neutrons. One of the first experiments of X-ray inelastic scattering was performed by Compton who found that the signal contains two different wavelengths for any scattering angle of 2θ.

For the inelastic case the initial and the final wavelengths are different, so $|\mathbf{k}_i| = 2\pi/\lambda_i$ and $|\mathbf{k}_f| = 2\pi/\lambda_f$. If $\lambda_i < \lambda_f$ then there is loss of energy, otherwise when $\lambda_i > \lambda_f$ there is gain of energy . In this case the scattering vector is not defined by $\mathbf{Q} = \mathbf{k}_i - \mathbf{k}_f$, but it takes the form

$$\mathbf{Q}^2 = \mathbf{k}_i^2 + \mathbf{k}_f^2 - 2\mathbf{k}_i\mathbf{k}_f \cos 2\theta \tag{2.28}$$

and the equation 2.15 takes the form

$$E_n = \frac{h^2}{2m_n}\left(\frac{1}{\lambda_i^2} - \frac{1}{\lambda_i^2}\right) \tag{2.29}$$

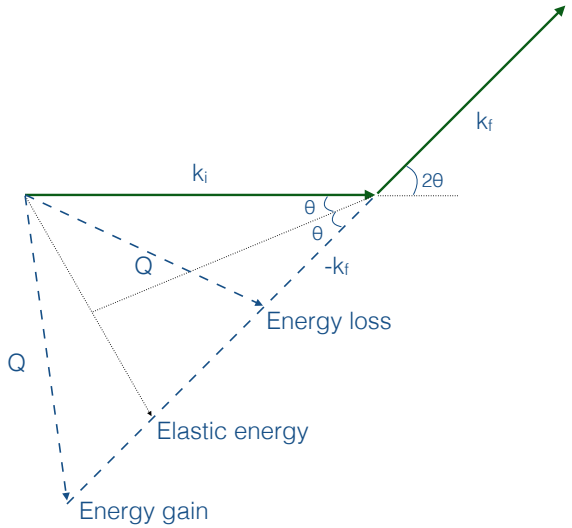

Figure 4: Wave vector representation for inelastic scattering.

and the angular frequency is

$$\omega = \frac{\pi h}{m_n}\left(\frac{1}{\lambda_i^2} - \frac{1}{\lambda_i^2}\right) \tag{2.30}$$

In similar way as I defined the partial differential cross section for elastic scattering I can define the partial deferential cross section for the inelastic scattering by using the equation 2.23, but now E_f is not the same with E_i. In figure 4 we can see that the triangle is not isosceles as it is for the elastic case (figure 2) but it depends on the energy and if the energy difference is positive or negative.

In the following chapter I will describe in detail the experimental setting, experimental instruments and the material I used for INS experiments. In chapter 4 I will describe how to reproduce INS data by performing simulations.

3 Experimental INS

In the previous chapter I discussed scattering techniques and I focused more on neutron scattering and the differences between elastic and inelastic scattering. In this chapter I will present results from inelastic neutron scattering experiments on barium at various temperatures. I will describe the experimental INS procedure, the data collection and analysis process, and I will discuss and compare them with literature. Data from INS experiments are considered to be highly accurate and provide the best method for comparison of dynamics for the various phases of materials. Barium is a simple structure metallic material that has high neutron scattering factor and the results from INS experiments are expected to be well defined.

3.1 Experimental procedure

3.1.1 MARI instrument

The experimental neutron scattering procedure is described by the neutron theory but during the procedure there are many adjustable parameters that need to be taken into account and affect the produced data. The use of different facilities and instruments might affect the quality and the quantity of data. My experiments were performed at ISIS pulsed spallation source and the instrument used is the MARI.

Spectrometers and diffractometers with pulsed spallation source are time of flight (TOF) instruments. TOF scattering is a method for determining the kinetic energy of a traveling neutron and is a form of inelastic neutron scattering where the initial position and velocity of a pulse of neutrons is fixed and their final position and the time after the pulse that the neutrons are detected are measured. This method is particularly useful for the neutron spectroscopy case where the energy of the scattered neutrons has to be determined. Furthermore, the TOF technique can also be used for fixing the energy of the neutron beam at a specific value before the interaction with the sample by means of a complex system of rotating disc choppers. This can be done by filtering neutrons with particular velocity and only these neu-

trons can pass and reach the sample. This kind of chopper system is called monochromator.

The monochromator selects just one wavelength out of the incoming neutron beam. According to de Broglie, neutrons with different kinetic energies are assigned different wavelengths so only neutrons with specific kinetic energy pass from the monochromator. The incident neutron energy that reaches the instrument is selected by phasing the opening time of the slit with respect to the neutron pulse from the target station. This can be done with a Fermi chopper which is a fast-rotating cylinder with slits designed for letting through neutrons at desired timings.

MARI is a direct geometry chopper spectrometer and it uses a Fermi chopper to monochromate the incident neutron beam giving wide energy range from 7 till 1,000 meV. In direct geometry spectrometers the incident energy is defined before reaching the sample by the chopper system and the final energy is determined by the TOF between the sample and the detectors. In indirect geometry spectrometers the incident energy is determined at the sample position by the measurement of the TOF and the final energy is measured by a monocrystal.

MARI uses a bank of ^{3}He detectors that cover a wide vertical angular range from 3° to 134° degrees and horizontal angular range of $-8°$ to $+8°$. The sample is positioned 4 m away from the MARI detector bank. Depending on the rotation frequency of the Fermi chopper, the incident energy and energy transfer at this distance, MARI instrument provides energy resolution of between 1.5-8%$\Delta E/E$. The exact incident energy is calculated from data that reach another set of detectors beyond the sample that have spatial separation. These detectors for the MARI instrument are ^{3}He gas detectors which surround a thin Vanadium foil and give a measure of the amount of beam that reaches the sample. By knowing the sample-detector distance and the time of flight after the scattering, the final energy can be calculated. MARI is the chopper spectrometer with the lowest instrumental background noise data within the ISIS instruments and although it has low incident neutron flux it is highly sensitive. That makes MARI a perfect instrument for studying phonon densities of states in crystalline and disordered systems.

3.1.2 Preparation and procedure

For studying phonon densities of states at the MARI spectrometer I used 70 g of barium in bead form. The purchased sample consists of 99.0% barium and 1.0% various impurities, with an average bead size of $0.5-2.0$ mm. Barium is a metal with body-centred cubic (bcc) crystal structure and $Im\bar{3}m$ space group, with lattice constant of 5.02 Å and melting point of the bulk at 998 K. For the initial measurements of the solid phase, barium was placed in a cylindric can made of aluminium. For measurements at higher temperatures, barium was stored in a niobium can, sealed by electron beam welding. During sealing the sample was under high vacuum. It was then placed in a furnace, spatially covered by four thin layers of niobium foil in order to allow uniform allocation of heat and low heating rate on the sample. To control the temperature there were two thermometers, one is the furnace's thermometer located in the outer part of the four niobium foils and the second is located next to sample.

The initial set of INS experiments was performed at 300 K where barium is in solid polycrystalline phase. The second set of experiments was performed at higher temperatures, at 963 K, 1,033 K, 1,173 K, 903 K and 603 K (following this sequence of temperatures) with 3 K maximum temperature fluctuation during each experiment and 9 K difference between the two thermometers. Temperature of 300 K is near room temperature where barium is solid. Temperatures of 963 K and 1,033 K are respectively slightly below and slightly above the melting point, while at 1,173 K the material is melted and at 903 K and 603 K is solidified again. That means that at these temperatures barium changes from polycrystalline solid to liquid and then again back to polycrystalline solid.

A third set of measurements at 300 K was performed with empty cans in order to measure the data that come from each can, known as background data measurement. To minimise background scattering the entire flight path is kept under vacuum but, as I will present in the results section, background scattering is unavoidable and it might affect the results. For all sets of experiments the frequency of Fermi chopper was set at 150 Hz, the frequency

of disc chopper was at 50 Hz and the incident neutron energy was 15 meV.

3.2 Results

The data from INS are in the form of three 2-dimensional matrices representing the time of flight, the energy E and the intensity for every detector at the area they cover, where intensity is the number of counts for the same pair of time of flight and E. The procedure to get the intensity as a function of momentum and energy transfer $S(\mathbf{Q}, E)$ is to normalise and reduce the data with data taken from measurements of an empty vanadium can and finally remove the background data from sample's data. Then I calculate the projection of the final data in the reciprocal space in order to get the intensity as a function of momentum and phonon frequency $S(\mathbf{Q}, \omega)$.

In figures 5, 6, 7, 8, 9 and 10 I present results from INS experiments on barium at various temperatures. In each figure there are four plots. In the first plot (upper left) I represent the intensity $S(\mathbf{Q}, \omega)$ of frequency with respect of scattering vector in a colour-scale map, drawn with data taken from the INS experiment after the data normalisation as I described earlier. In these plots we can observe the acoustic phonon branches at positive and negative values which represent the energy gain and loss. The phonon excitations are more intense around the Bragg peaks and on the elastic line and less intense at higher frequencies. With pure blue colour is the area with no detected neutron scattering.

As we can see in these figures, experimental INS the phonon collective excitations do not provide clear information on the specific phonon branches and there are many noise data close to phonon branches, thus clear results can not be extracted. It is worth mentioning that scattering intensity increases at higher values of $\mathbf{Q}$, something that mathematically can be explained from the scattering function equation 2.27, so someone would expect clearer phonon dispersion curves. Perhaps that would be the case for INS experiments with single crystal samples where the phonon dispersion curves are well defined.

The sample I used is polycrystalline with very small beads size, that can be treated as powder without any orientation. Powder samples do not

allow the study of specific phonon dispersion curves but only the study of the collective excitation spectra. The key point of my studies, the phonon−roton minimum, is located in the low or intermediate $\mathbf{Q}$ range so in my experiments I will not study data at higher $\mathbf{Q}$ values.

In the second plot (bottom left) I represent data same as in the first plot but multiplied by squared energy values over squared scattering vector values ($E^2/\mathbf{Q}^2$). For the case of polycrystals, amorphous or liquids it becomes difficult to describe the excitations for wavelengths larger than the interatomic spacing, thus for small $\mathbf{Q}$ values. By using this factor it is easier to visualise and study the collective excitation spectrum. The scattering intensity $\mathrm{S}(\mathbf{Q},\omega)$ multiplied by the ($E^2/\mathbf{Q}^2$) factor is equal to the spectra of the longitudinal current correlation function $\mathrm{J}(\mathbf{Q},\omega)$ [38].

$$J(\mathbf{Q},\omega) = \frac{\omega^2\, S(\mathbf{Q},\omega)}{\mathbf{Q}^2} \tag{3.1}$$

The current correlation function describes the correlation of particle velocities rather than particle positions, as is the case for the $S(\mathbf{Q},\omega)$. By using the $J(\mathbf{Q},\omega)$, the high-frequency part of the spectra is enhanced, allowing the study of weak high-frequency excitations. The E^2 factor has a minor effect on the peak frequencies and thus they are not strictly coincident with the frequencies given by $S(\mathbf{Q},\omega)$. Still, longitudinal current correlation function demonstrates the main features of the dispersion [39].

For all upper left colour maps and all bottom left colour maps I use the same colour scale, from 0 to 25 and from 0 to 100 respectively. It is important to make clear that the scattering intensity depends on the number of data collected during the experiment, which is different for every experiment and depends on neutron's beam flux and total scattering time, but it does not affect the ω or $\mathbf{Q}$ values. The characteristic phonon dispersion curves for the various structural phases at different temperatures should be well separated regardless of the scattering intensity, but as it is the case usually in experiments the higher the intensity the clearer the results.

The damping process of dispersion curves can be described quantitatively with the damped harmonic oscillator (DHO) line-shape modelling (fitting)

of the spectrum. The equation that describes the fitted $S(\mathbf{Q},\omega)$ is [40]

$$S(\mathbf{Q},\omega) = I_{\mathbf{Q}}\frac{n_{\mathrm{B}}(\omega)+1}{\pi} \times \frac{4\omega\omega_{\mathbf{Q}}\Gamma_{\mathbf{Q}}}{[\omega^2-(\omega_{\mathbf{Q}}^2+\Gamma_{\mathbf{Q}}^2)]^2+(2\omega\Gamma_{\mathbf{Q}})^2} \tag{3.2}$$

where $I_{\mathbf{Q}}$ is the intensity, $n_{\mathrm{B}}(\omega)$ is the Boltzman distribution function, ω is the energy transfer, $\omega_{\mathbf{Q}}$ is the energy and $\Gamma_{\mathbf{Q}}$ is the width of the phonon excitation or damping factor. The DHO fitting is a generally accepted line-shape fitting for IXS and INS spectra of solids and liquids (e.g. [41–45]) in order to evaluate the appropriate transformation, explained in details for crystals in reference [46] and for liquids in reference [47].

The results of the DHO fitting of the INS data multiplied by the $E^2/\mathbf{Q}^2$ factor are located in the upper right plot for every figure at different temperatures. All these figures describe with one curve the collective excitation spectra. The curve in each figure exhibits an almost linear increase at low $\mathbf{Q}$ with a maximum value at around $\mathbf{Q} = 1.06$Å, a minimum at around $\mathbf{Q} = 1.66$Å and then a maximum again. At 300 K the fitted data do not exhibit a clear minimum, as it is the case for the fitting at other temperatures. At 903 K and especially at 603 K the initial part of the fitting curve at low $\mathbf{Q}$ appears not to be linear, as it is at higher temperatures.

The results of the DHO fitting depend on the damping factor (Γ), which depends on scattering vector and temperature. When the damping factor is small, the dispersion curves from $\mathrm{S}(\mathbf{Q},\omega)$ are in good agreement with the dispersion curves from $\mathrm{J}(\mathbf{Q},\omega)$, which means that the multiplication with the $E^2/\mathbf{Q}^2$ factor does not highly affect the original data. The damping factor with respect of scattering vector can be seen in the bottom right plot for every temperature. Γ values increases almost linearly as $\mathbf{Q}$ increases till a certain value, while at higher values Γ increases rapidly and its value starts fluctuate. At 963 K, 1033 K and 1173 K the curves are very similar qualitatively, while at 300 K, 903 K and 603 K the curves are different.

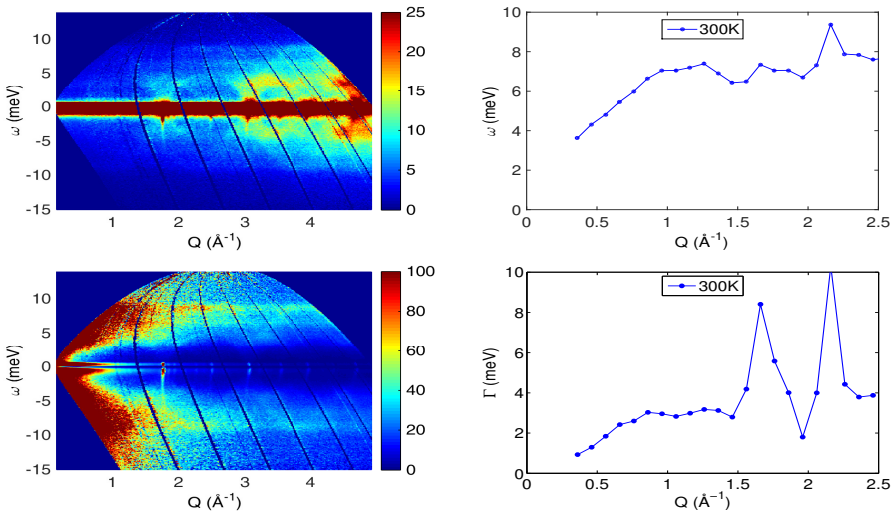

Figure 5: T = 300 K. Upper left: Collective excitation spectrum of Ba from INS experiments presenting the phonon frequencies over larger scattering vector regime. The colour map represents the intensity of scattered neutrons at every $\mathbf{Q}$ and ω. Bottom left: Collective excitation spectrum from INS experiments with intensity multiplied by $E^2/\mathbf{Q}^2$. Upper right: DHO fit of collective excitation spectrum from INS experiments with intensity multiplied by $E^2/\mathbf{Q}^2$ at the low and intermediate $\mathbf{Q}$ regime. Bottom right: Damping factor of the DHO fit.

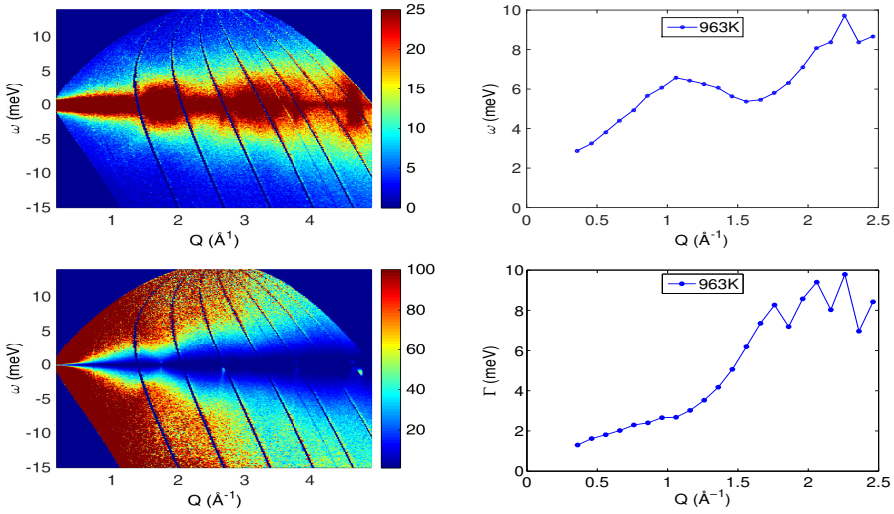

Figure 6: T = 963 K. Description as caption in figure 5.

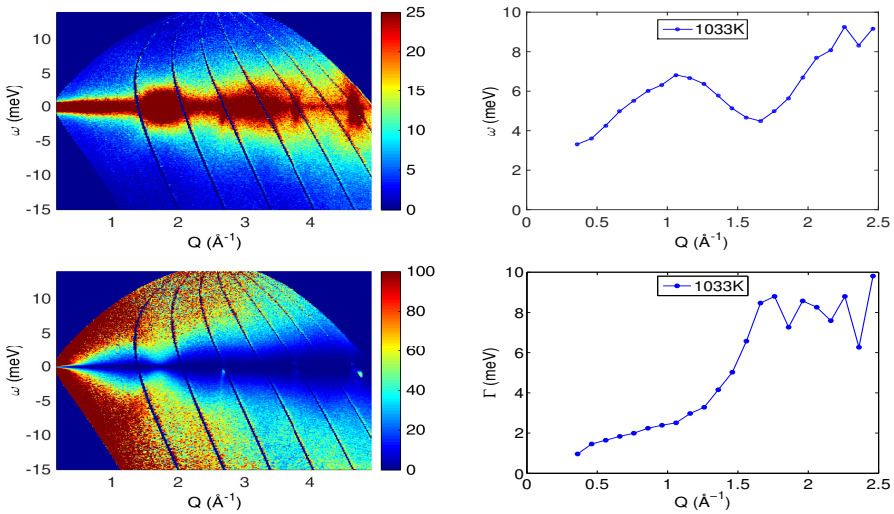

Figure 7: T = 1,033 K. Description as caption in figure 5.

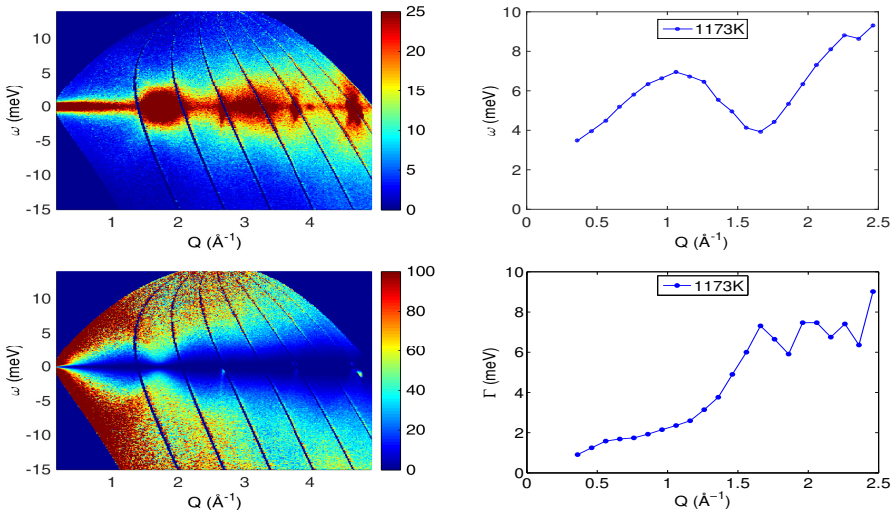

Figure 8: T = 1,173 K. Description as caption in figure 5.

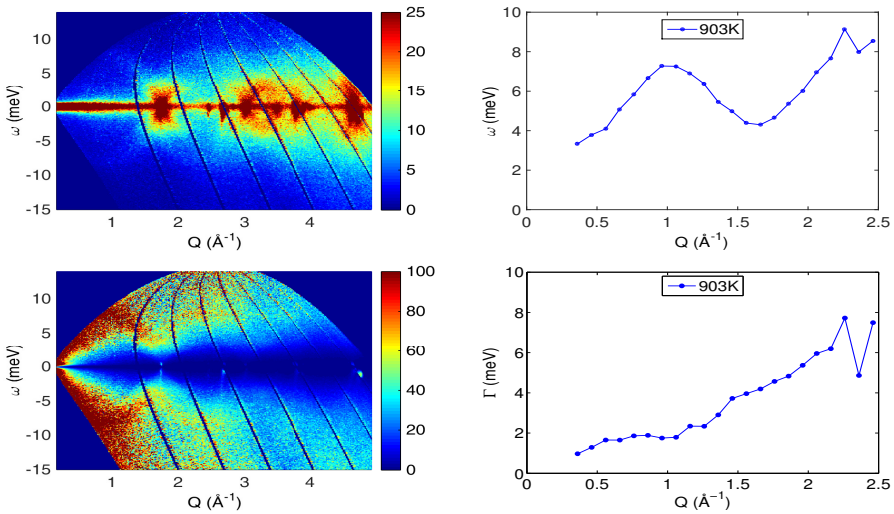

Figure 9: T = 903 K. Description as caption in figure 5.

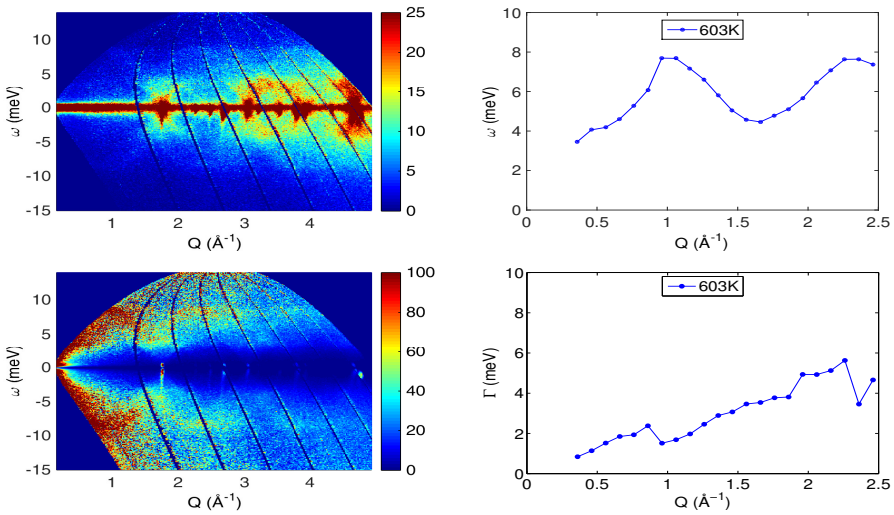

Figure 10: T = 603 K. Description as caption in figure 5.

3.3 Summary and discussion

The first theoretical calculation of barium's phonon dispersion curves was done by Animalu in 1967 [48] where he calculated the Gibbs free energy for body-centred cubic and face-centred cubic (fcc) materials at zero pressure and

temperature by using the Heine-Abarenkov model [49] to study phase transitions, showing that barium keeps the bcc formation even at absolute zero temperature, something that was also experimentally observed [50]. Later on Moriarty [51] presented results for barium's phonon frequencies by using the s-d hybridisation pseudopotential theory [52, 53]. Then Sharma [54] with his model, the linear potential [55], predicted the phonon dispersion curves of barium and he calculated its physical properties such as elastic constants and bulk modulus. All three Animalu's, Moriarty's and Sharma's results are in good qualitative match.

The first INS experiment for the calculation of barium's phonon dispersion curves was preformed by Buchenau *et al* [56] in 1984. The sample was polycrystalline barium and the results were taken from TOF INS and they were fitted with the Born-von Karman model up to third neighbour. These results present dispersion curves similar to the previous theoretical work but at slightly lower values, something that according to Moriarty [57] is due to the neglect of electronic d-state hybridisation in a simple model as is the Born-von Karman model. Although with this fit the estimated phonon frequencies exhibit a small error (2 to 3%) and quantitatively should not be compared with other results, qualitatively it describes well the phonon dispersion curves. As Buchenau *et al* comment, barium's longitudinal and transverse branches along the [1 0 0] direction degenerate, something that has been observed in other alkali metals.

Then Mizuki *et al* [58] performed similar calculation and they fitted the data up to sixth neighbour getting results in reasonable agreement. Mizuki *et al* discuss about the anomalous behaviour of the dispersion curves along the [1 0 0] direction of barium, where the frequencies of the longitudinal branch are lower than those of the transverse branch, something that remains even at higher temperatures. This contradicts initial theoretical studies [48, 51, 54] while in Buchenau *et al* work is not stated clearly.

Nevertheless, in all previously mentioned studies the minimum in the phonon spectrum at the longitudinal mode along the [1 1 1] direction for the crystalline phase is obvious. Other INS and IXS experimental studies on alkali metals, alkaline earth metals and other elements for the crystal and

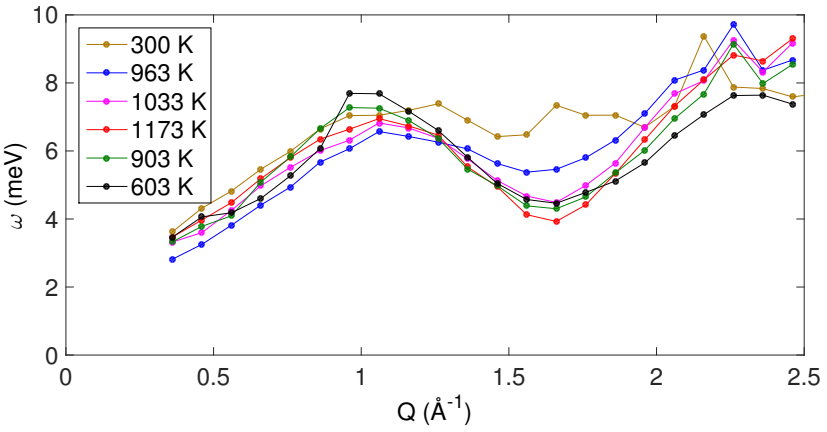

Figure 11: DHO fit graph of collective excitation spectrum of Ba from INS experiments at various temperatures. The intensity is multiplied by $E^2/\mathbf{Q}^2$ at the low and intermediate $\mathbf{Q}$ regime.

liquid phase show the existence of the phonon−roton minimum (e.g. bcc Na [59], bcc K [60], bcc Fe [61], bcc V [62], rare gas solids (fcc) [63], fcc Yb [64], fcc Ca [65], fcc Sr [56], bcc and liquid K [66], review on some bcc alkali metals [67], extended review on liquid metals [4], bcc and liquid Na [1]). Apart from the existence of the phonon−roton minimum, the published results verify the similarity of the crystal and liquid phonon spectra of the same material, at the low $\mathbf{Q}$ regime. The last two conclusions can also be verified by the INS experiments I performed on barium.

In figure 11 I present results from DHO fit of the collective excitation spectra of Ba from INS experiments multiplied by $E^2/\mathbf{Q}^2$ at the low $\mathbf{Q}$ regime at all different temperatures. As it is expected from the theory, the INS spectra for the crystalline phase should exhibit distinctive phonon dispersion curves. For the liquid and amorphous phases the specra is expected to exhibit and average over all dispersion curves. Thus, a fitting over all data, as is the DHO fitting, is expected to exhibit a rough curve for the crystalline phase, highly affected from the distinct dispersion curves, and a smooth curve for the liquid and amorphous phases. All phases, at the various temperatures, exhibit the phonon−roton minimum whilst at the same time the phonon collective excitations almost degenerate despite the large temperature difference. Ex-

ceptions are the curves that represent the 300 K and 963 K. We can see that these curves exhibit higher values at the point of the minimum. Although there is no clear indication, this anomalous behaviour can be justified due to experimental errors.

As I mentioned the first set of experiments was at 300 K and the second set was at various temperatures starting at 963 K. Barium is highly reactive with water and this is why it is stored under inert gas. Although all precautions were taken to keep the sample in dry environment the existence of moisture on the sample's surface can not be avoided. Moisture can react with barium's surface to create a thin layer of barium hydroxide or barium hydride molecules, something that gives different results during neutron scattering. Similar explanation can be given for the experiment at 963 K but perhaps due to higher temperature there is less moisture in the sample's environment.

A different explanation can be given due to high temperature. Bulk barium's melting point is at 998K which is 35 degrees higher than the 963 K, difference that could be easily covered due to experimental temperature reading error or due to sample's lower melting point because of the powder form. The DHO fit results at 963 K give a smooth curve that looks similar to the liquid's curve (at 1,033 K and 1,173 K), something that could be justified with the second argument but they exhibit phonon frequencies at values not that similar to the liquid's or crystal's frequencies, something that could be justified with the first argument. Since it is not clear what affects the sample during the first two experiments I decided to exclude them from any future discussion and conclusions. The rest of the results in figures 7, 8, 9 and 10 include the liquid and the re-crystallised barium phases and I am able to make safe conclusions for both solid and liquid state.

In figure 12 I present results of the damping factor from the DHO fittings of the collective excitation spectra at all different temperatures. For the initial linear part of the low $\mathbf{Q}$ regime in figure 11 we can observe that the damping factor in figure 12 is small but at higher $\mathbf{Q}$ values, where the first peak in figure 11 is, there is a rapid increase for Γ. Moreover we can see that Γ has a different behaviour for experiments at 903 K and 603 K where the sample is re-crystallised. The damping factor exhibits lower values and less

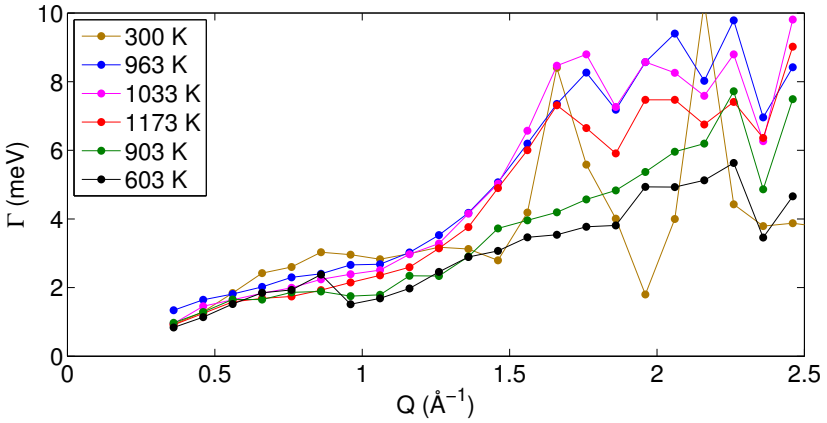

Figure 12: Damping factor of DHO fit of Ba collective excitation spectra from experiments multiplied by $E^2/\mathbf{Q}^2$ at various temperatures.

vibration along $\mathbf{Q}$, something which can be attributed to the structural phase and the lower temperature. We can see that in all experiments the damping factor follows a similar pattern apart from the first experiment at 300 K where at the high $\mathbf{Q}$ regime there is a big variation in the Γ values. This justifies the anomalous behaviour that is observed in the DHO fit at 300 K. At 963 K, the damping factor does not exhibit an anomalous behaviour but it has slightly higher value from the rest damping factors at different temperatures, higher or lower, and qualitatively is very similar to the damping factor curves of the liquid phase.

In metallic systems it has been found that the damping increases more rapidly with increasing temperature [68,69]. The general functional form for damping in this case is

$$\Gamma_{\text{metallic}} = \Gamma_m \mathbf{Q}(\mathbf{Q}^2 + \kappa^2) \tag{3.3}$$

where Γ_m is a material dependent constant and κ is a parameter related to the width of the phonon excitation, which has high temperature dependence

$$\kappa = \kappa_0 \left(\frac{T - T_{\text{C}}}{T_{\text{C}}} \right)^m \tag{3.4}$$

where κ_0 is the correlation length of the fuctuations at $T = 2T_C$, T_C is the critical temperature and m is a constant which is material dependent. Thus the behaviour of damping factor showing $\mathbf{Q}$ and temperature dependence in figure 12 can be explained from the equation 3.3.

To evaluate the results of the DHO fit I compare the results from the DHO fit with the experimental data. In figure 13 I present the intensity with respect of phonon frequency for two different scattering vectors at all different experimental temperatures. With green line and circles are the experimental data multiplied by $E^2/\mathbf{Q}^2$ and with blue line the fitted DHO curve. As it is usually the case the fitting of a straight curve produces low error results and the main challenge remains at points where the curve changes slope.

As we can see in figure 11 the two regimes from about 0.5 to 1.0 Å^{-1} and about 1.7 to 2.0 Å^{-1} the DHO fit shows a positive slope almost linear curve and the regime of about 1.1 to 1.5 Å^{-1} the DHO fit shows a negative slope almost linear curve. The points in the DHO fit and the points I selected to evaluate the fit are at $\mathbf{Q} = 1.0$ Å^{-1} (peak point) and at $\mathbf{Q} = 1.66$ Å^{-1} (bottom point). As we can see the fitted curve represents well the experimental data at all different temperatures, with the peak of the curve close to the highest intensity experimental points, for both different scattering vectors.

At $\mathbf{Q} = 1.0$ Å^{-1} we can see that the detectors' allocation at this incident energy allows the detection of neutrons with final energy of up to 10 meV. This is something that possibly affects the accuracy of the peak value of the DHO fit. At $\mathbf{Q} = 1.66$ Å^{-1} this is not the case and we can see that the detectors measure all scattered neutrons up to 14 meV, giving a smoother and more accurate fit.

In this figure there are two interesting points. The first point is the appearance of a sharp peak at low $\mathbf{Q}$ in the first set of experiments at 300 K, something that explains the anomalous behaviour of the DHO fit and verifies the earlier hypothesis that either the sample contained impurities or it was oxidised. The second point is in the plots with $\mathbf{Q} = 1.66$ Å^{-1}. In experiments at 300 K, 903 K and 603 K we can see a sharp peak at low phonon frequencies, something that can not be seen at higher temperatures or at $\mathbf{Q} = 1.0$ Å^{-1}, apart from the plot at 300 K.

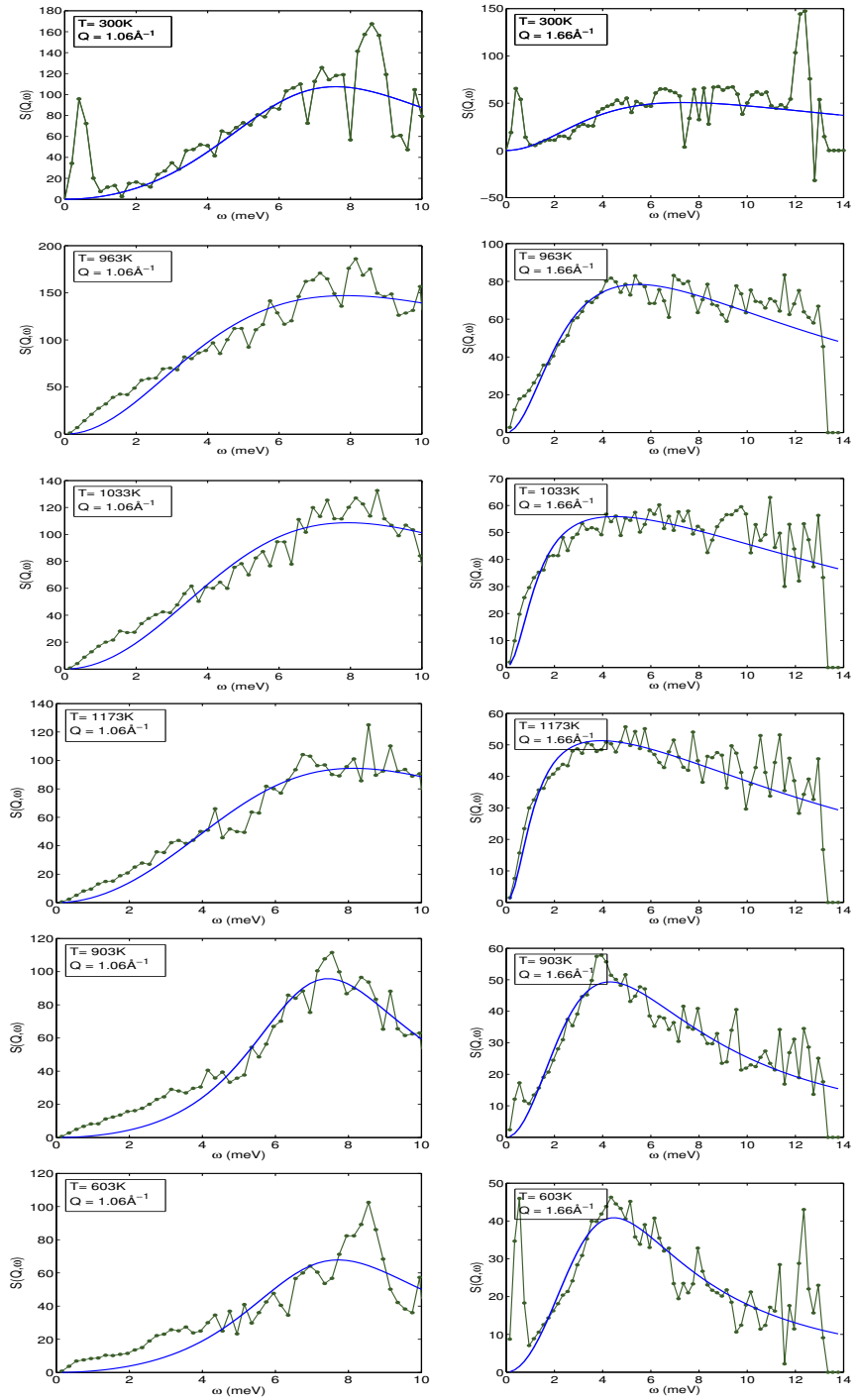

Figure 13: Intensity multiplied by $E^2/\mathbf{Q}^2$ with respect of energy at various temperatures for Ba at $\mathbf{Q} = 1.0\text{Å}^{-1}$ and $\mathbf{Q}$ =1.66Å^{-1}. With green line and circle are represented the experimental data and with blue line is the DHO fit.

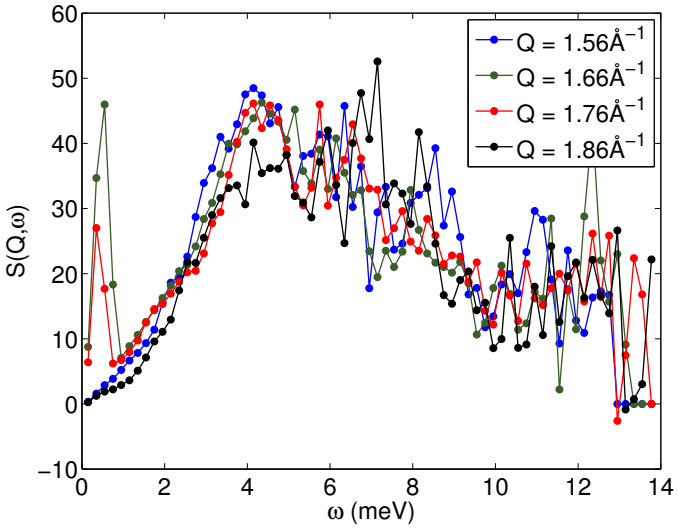

Figure 14: T = 603 K. Intensity from experimental data multiplied by $E^2/\mathbf{Q}^2$ with respect of energy at various values of **Q.**

For crystals the Bragg peaks are well defined and can be identified at characteristic points. For crystal barium a Bragg peak can be identified at **Q** = 1.77 Å^{-1} while for polycrystalline barium this value should be the same but due to various orientations of the polycrystals it is not easily identified. This can be seen in the collective excitation spectra of Ba from INS experiments at various temperatures in figures 5, 6, 7, 8, 9 and 10. This can also be seen in figure 14 where I present results for intensity from experimental INS at 603 K for various values of **Q** close to Bragg peak. We can see that the sharp peak at low phonon frequencies can be seen at both **Q** = 1.66 Å^{-1} and **Q** = 1.76 Å^{-1}. That means that these sharp peaks at 300 K, 903 K and 603 K possibly represent the Bragg peaks and the crystalline phase, while when there is no peak the sample is probably in liquid phase. This outcome explains the anomalous behaviour of the results in the experiment at 963 K and supports the explanation of an already molten material at this temperature.

In conclusion, I performed INS experiments on barium at various temperatures, covering both crystal and liquid phase. I presented results from these

experiments representing the collective excitation spectra of barium at various temperatures focusing more in the low and intermediate $\mathbf{Q}$ regime. Data analysis involves the DHO fit of the initial data multiplied by the $E^2/\mathbf{Q}^2$ factor in order to enhance the data at the low $\mathbf{Q}$ regime, the analysis of the damping factor at every temperature and the comparison of experimental and fitted data in order to evaluate the DHO fit. The fit was proved to represent accurately the experimental results.

Results from the DHO fit in figure 11 reveal that the first experiment at 300 K shows an anomalous behaviour that I attribute it in error during the sample's preparation. Similarly at 963 K the experimental error, either during the sample's preparation or during the experiment, affects the data and does not make them trustworthy to make any conclusion out of them. Results from experiments at 300 K and 963 K will not be discussed more and will not be used in the next chapters as comparison results between experiments, simulations and theory. The rest data exhibit the expected behaviour and we can see that the collective excitation spectra for the crystalline and liquid phase are in a good match and that the phonon−roton minimum can be seen in both structural phases. In the next chapter I will reproduce these results for various materials for the solid and liquid phase by performing INS simulations and I will compare them with the experimental results.

4 Computational approach

In this chapter I examine the theory and the procedure of the computational simulations I performed in order to reproduce experimental results and furthermore to examine topics that cannot be studied through experiments. I discuss how to represent inelastic neutron scattering by performing simulations and I analyse the results in similar way as in the INS experiments discussed in the previous chapter and compare. For the INS simulations the main study system is iron, which has similar physical properties with barium and the results can easily compare. Results from INS simulations of iron are also compared with results from INS simulations of argon in order to prove the validity of simulations over a simple system, which is often used as example, and describe the validity of the theory over a structurally different system.

Both iron and barium form a bcc structure and direct comparison or a model conversion can be made. More importantly iron's dispersion curves are very similar to barium's dispersion curves. Dispersion curves for both systems from theory, experiments and simulations can be found in literature (Ba: [48,51,54,56,58], Fe: [61,70–74]). The dispersion curves of both systems follow an almost identical pattern showing that dynamics of these two systems are highly comparable. As I explain in section 4.4, because of this similarity with the use of a simple model we can convert the values of energy and wave vector of the dispersion curves of iron and represent barium's dispersion curves.

In order to prepare the structure in crystalline, amorphous and liquid phase I performed classical molecular dynamics (MD) simulations. From the results I present analysis of the local structure analysis and atomic bonding in order to discuss the structural phases of various simple materials and be able to make a connection between the solid and liquid phase. All the studied materials are monatomic and form bcc structure in solid phase, thus direct comparison can be made. I present results from population analysis and angle between bonds analysis for all the materials I used for their short-range structure.

Simulations of barium are not easy to be performed due to absence of

interatomic potential parameters in order to perform molecular dynamics simulations. At the end of this chapter I present the method to develop the interatomic potential parameters for systems, focusing on barium. I analyse the quantum MD simulations and the fitting process and moreover I analyse the short-range structure of barium in a similar way as for the previous materials.

4.1 Molecular Dynamics simulations

The molecular dynamics method was initially introduced by Alder and Wainwright in 1957 [75] and the first MD simulation was performed in 1964 by Rahman for the simulation of liquid argon [76]. MD is a deterministic way to simulate the movement of the atoms. Classical molecular dynamics is a computational approach which predicts the behaviour of a system of particles in the course of time by solving the Newton's equation of motion.

$$\mathbf{F}_i = m_i \mathbf{a}_i = m_i \frac{\partial \mathbf{v}_i}{\partial t} = m_i \frac{\partial^2 \mathbf{r}_i}{\partial t^2} = -\frac{\partial V}{\partial \mathbf{r}_i} \tag{4.1}$$

$\mathbf{F}_i$ is the force applied along the Cartesian coordinates $\mathbf{r}_i$ on particle i with mass m_i, velocity $\mathbf{v}_i$, acceleration $\mathbf{a}_i$ and V is the potential energy of the system. With the use of force fields it is possible to describe the interactions between the atoms of a system. The MD simulations provide information of the dynamics of the system at the microscopic level.

The necessary input information is all atoms' positions and masses, and the force function that describes the interaction between atoms, the interatomic potential. The simulation is divided into a number of time steps, usually in the order of femtoseconds. For each time step all the new forces between all atoms are calculated from the equation 4.1 and then integrated to obtain new positions and velocities and this is iterated to the end of the simulation. Once the positions and velocities of each atom are known the state of the system can be predicted at any time in the future. During the time steps the system properties are calculated from the position, velocity and force equations.

For the majority of simulations I present I refer to classical molecular dynamics simulations. In the last subsection of this chapter I describe the development of interatomic potential parameters for barium and I perform *ab initio* molecular dynamics simulations. In classical MD all the quantum effects are not considered and everything that underlies the laws of quantum physics, as is the motion of electrons, is neglected. In classical MD the forces are calculated from a parameterised potential, either fitted to empirical data or to first principles calculations. An advantage of classical MD is that it is a faster method in comparison with *ab initio* molecular dynamics and large systems can be simulated fast and for long simulation time, in order to simulate processes like diffusion which require a long time to occur.

In *ab initio* MD simulations the motion of atoms is treated similarly to classical MD simulations but the interatomic forces are calculated differently. In classical molecular dynamics, a single potential energy surface is represented in the force field. During *ab initio* MD simulations the electronic behaviour is obtained by performing quantum calculations. With this method we can achieve higher accuracy in the representation of the electronic behaviour than with the empirical interatomic forces. Due to the cost of treating the electronic degrees of freedom, the computational cost of this simulations is much higher than classical molecular dynamics This implies that the *ab initio* MD simulations are limited to smaller systems and shorter periods of time.

The advantage of an empirically fitted potential is that it can be modified to study how the changes in the potential affects the physical properties of the system. Hence it can be a useful model to understand the underlying mechanics of the system. Still, the use of interatomic potentials poses various problems. Firstly because the potential is empirically fitted potential the results will never have the same accuracy as experiment results and there will always be compromises. One also has to decide what properties are most important to reproduce and which ones should be fitted to.

There is also the problem of transferability, since the parameters are fitted to experimental or first principles data for certain conditions. This means that it is difficult to know how accurate the potential is in an unknown

configuration or under various different conditions. As the goal is to predict properties that are unknown this is a severe limitation. So far for classical MD simulations there are various interatomic potential models that describe a large range of various systems accurately at many different conditions.

4.1.1 Interatomic potentials

Most of the simple models describing interatomic interactions are pair potential models, so they calculate the interactions between pairs of atoms. There are also more advanced models describing more accurately atom interactions between more than two neighbour atoms, usually dependent on the distance. All the interatomic potentials for my simulations are well known empirical anharmonic interatomic potentials, including the Lennard-Jones [77], Buckingham [78] and Morse [79] pair potentials, the Tersoff [80] many-body potential, the embedded atom model (EAM) [81, 82], the Finnis−Sinclair potential [83] and the extended Finnis−Sinclair potential [84]. The values I used for the interatomic potentials for each specific system can be found in the literature and are tested and published by other scientists.

Every type of potential is described by a different equation and functions better for different systems. The Lennard-Jones potential is defined as

$$U(r_{ij}) = 4\epsilon \left[\left(\frac{\sigma}{r_{ij}} \right)^{12} - \left(\frac{\sigma}{r_{ij}} \right)^{6} \right] \tag{4.2}$$

where ϵ is the depth of the potential well, σ is the finite distance at which the potential is zero and r_{ij} is the distance between atoms i and j. The term proportional to r_{ij}^{-12} models the repulsion due to the non bonded overlap of the electronic orbitals while the term proportional to r_{ij}^{-6} models the van der Waals dispersion forces caused by the dipole-dipole interactions due to fluctuating dipoles.

The Buckingham potential was proposed as a simplification of the Lennard-

Jones potential and is defined as

$$U(r_{ij}) = A \exp\left(-\frac{r_{ij}}{\rho}\right) - \frac{C}{r_{ij}^6} \tag{4.3}$$

where A and C are the coefficients of the repulsive and attractive terms respectively, r_{ij} is the interatomic distance and ρ is the repulsive index.

The Morse potential is defined as

$$U(r_{ij}) = E_0 \left(\{1 - \exp\left[-k\left(r_{ij} - r_0\right)\right]\}^2 - 1\right) \tag{4.4}$$

where E_0 is the well depth, k represents a variable that controls the width of the potential's well and r_0 is the equilibrium bond distance and r_{ij} is the interatomic distance.

The Tersoff potential is defined as

$$U(r_{ij}) = f_C(r_{ij})[f_R(r_{ij}) - \gamma_{ij} f_A(r_{ij})] \tag{4.5}$$

where $f_R(r_{ij}) = A_{ij} \exp(-a_{ij} r_{ij})$ and $f_A(r_{ij}) = B_{ij} \exp(-b_{ij} r_{ij})$ are the repulsive and attractive pair potential respectively and f_C is a smooth cutoff function, while γ expresses a dependence that can accentuate or diminish the attractive force relative to the repulsive force according to the local environment and r_{ij} is the interatomic distance.

The EAM is designed to simulate metals and is defined as

$$U_{tot} = F_\alpha \left(\sum_{i \neq j} \rho_\beta(r_{ij})\right) + \frac{1}{2} \sum_{i \neq j} \phi_{\alpha\beta}(r_{ij}) \tag{4.6}$$

where F_α is an embedding function that represents the energy required to move the atom i of type α, ρ_β is the contribution to the electron charge density from atom j of type β at the location of atom i, r_{ij} is the distance between the atoms i and j and $\phi_{\alpha\beta}$ is the repulsive pair potential.

The Finnis−Sinclair potential is a type of embedded atom potential, which incorporates the band character of metallic cohesion and allows to obtain correct values for the vacancy formation and cohesive energy. This is

given as

$$U_{tot} = U_P + U_N = \frac{1}{2}\sum_{ij} V(r_{ij}) - A\sum_i \sqrt{\rho_i} \tag{4.7}$$

where U_P is the repulsive pair potential and U_N is the N-body term, r_{ij} is the distance between atoms i and j. For $r_{ij} \leq c, V(r_{ij}) = ((r_{ij} - c)^2(c_0 + c_1 r_{ij} + c_2 r_{ij}^2)$, while for $r_{ij} > c, V(r_{ij}) = 0$. c, c_0, c_1, c_2 and A are fitting parameters. The density ρ_i is given as $\rho_i(r_i) = \sum_j \phi(r_{ij})$. For $r_{ij} \leq d, \phi(r_{ij}) = (r_{ij} - d)^2$ and for $r_{ij} > d, \phi(r_{ij}) = 0$. c and d describe distances between the second and third neighbour.

The extended Finnis−Sinclair potential is a more precise model than the original Finnis−Sinclair potential. The difference is that for $r_{ij} \leq c, V(r_{ij}) = ((r_{ij} - c)^2(c_0 + c_1 r_{ij} + c_2 r_{ij}^2 + c_3 r_{ij}^3 + c_4 r_{ij}^4)$ and for $r_{ij} > c, V(r_{ij}) = 0$ and $r_{ij} \leq d, \phi(r_{ij}) = (r_{ij} - d)^2 + B(r_{ij} - d)^4$ and for $r_{ij} > d, \phi(r_{ij}) = 0$. Similarly in this potential c, c_0, c_1, c_2, c_3, c_4, A and B are fitting parameters.

All the previous potentials are short-range potentials and describe interactions for a specific cut-off. Usually this distance is long enough to describe interactions between an atom and its second or third neighbour atoms. The long-range potential which describes the interactions for distances larger than the cut-off for all systems is the Coulomb potential.

4.1.2 MD features and methodology

In this section I describe the methodology I implement to perform MD simulations. The same methodology applies for all the simulations I describe in this thesis, not only in this chapter but also in chapter 6. Depending on the simulated system, I adapt the method and the parameters in order to describe accurately the system. Unless I state a different procedure, the following method and techniques were implemented.

To prepare the materials in order to perform simulations in various structural phases I expanded the unit cell of each material symmetrically towards all directions, following the periodicity of the system and by using periodic boundary conditions (PBC) in order to create a large enough bulk system. With PBC someone can study the bulk properties of a material since PBC

eliminate the surface and the surface effects, and the system is treated as infinite system. Using periodic boundary conditions implies that particles are enclosed in a box, which is imaginarily replicated to infinity by rigid translation in all the three Cartesian directions, completely filling the space. When a particle enters or leaves the simulation box, an image particle leaves or enters this box, such that the number of particles from the simulation region is always conserved. With the use of a potential with finite range (short-range or long-range potential) and the use of modern MD simulations code, possible double calculation of pair interactions is avoided.

The software I used to perform classical MD simulations is the DLPOLY software [85] which implements various well known techniques. For efficient use of the long-range potential in charged systems I used the Ewald summation [86]. For bulk systems a straightforward approach to calculate the long-range potential energy is the direct sum. The direct sum, although is a very simple method to implement is excessively computationally demanding. The Ewald sum is a faster method to compute electrostatic quantities such as energies or forces and this is because it handles differently the distances between atoms. This method allows the user to define the level of accuracy, which for my simulations is always set at 1e-5, which is considered to be highly accurate. Higher accuracy demands much more computationally intense calculations disproportional to the accuracy of the results, making the Ewald summation method equally demanding as the direct sum method. The Ewald summation is still considered by many the best method for computing long-range electrostatic interactions in periodic systems [87, 88].

After creating the structure, the system needs to be treated accordingly in order to relax and reach its equilibrium properties and represent more realistically the material. In MD simulations there are various ensembles that can be implemented during a simulation. Equilibration of a system can be achieved by simulating the system under constant pressure and temperature in order to allow the atoms in the system to move and self-arrange in the configuration. In my simulations I performed equilibration by using the NPT Berendsen algorithm, where NPT defines an ensemble under constant pressure and temperature while the energy and the volume are allowed to change.

The Berendsen thermostat [89] is an algorithm to re-scale the velocities of atoms in order to control the simulation temperature. The thermostat and barostat relaxation times are user adjustable and in my case I used 1.0 ps for both of them. Moreover I also used the NPT Hoover thermostat and barostat which I also used in my simulations is a canonical ensemble that uses the Nosé-Hoover algorithm [90, 91].

According to Gibbs [92], a microcanonical ensemble is the statistical ensemble that is used to represent the possible states of a mechanical system which has an exactly specified total energy. The system is assumed to be isolated in the sense that the system cannot exchange energy or particles with its environment, so that by conservation of energy, the energy of the system remains exactly known as time goes on. In the same sense, a canonical ensemble is the statistical ensemble that is used to represent the possible states of a mechanical system which is in thermal equilibrium with a heat bath [92]. The system is said to be closed in the sense that the system can exchange energy with a heat bath, so that various possible states of the system can differ in total energy.

The most common approach to study the motion of the atoms in a system and calculate various properties, as I do for C_{V} in Chapter 6, is the microcanonical NVE ensemble. The NVE is defined as an ensemble in which the volume and the energy of the system are constant and the temperature and the pressure are allowed to change. In my simulations I tested both NPT Berendsen and NVE with NPT Hoover and NVE Hoover respectively, without noticing any significant difference in the calculated macroscopic system properties.

By default the DLPOLY software integration algorithms are based on the Velocity Verlet scheme [93]. The Verlet algorithm [94] is a very simple algorithm that gives good long simulation time accuracy at the cost of a quite poor short simulation time accuracy by using other algorithms, something that leads to shorter allowed time steps. Moreover, the memory usage of this integrator is as small as possible. The positions $\mathbf{r}$ for the next time step are

generated by

$$\mathbf{r}(t+\delta t) = 2\mathbf{r}(t) - \mathbf{r}(t-\delta t) + \frac{\mathbf{f}(t)}{m}\delta t^2 \tag{4.8}$$

where $\mathbf{f}$ is the force, m the mass of the atom and t is the time step. The velocities are obtained by the equation

$$\mathbf{v}(t+\delta t) = \frac{\mathbf{r}(t+\delta t) - \mathbf{r}(t-\delta t)}{2\delta t} \tag{4.9}$$

The Velocity Verlet is a Verlet-like integrator that gives the same trajectories but also gives the velocities in a more straightforward way. The positions and velocities are given from the equations

$$\mathbf{r}(t+\delta t) = \mathbf{r}(t) - \mathbf{v}(t)\delta t + \frac{\mathbf{f}(t)}{2m}\delta t^2 \tag{4.10}$$

$$\mathbf{v}(t+\delta t) = \mathbf{v}(t) + \frac{\mathbf{f}(t+\delta t) + \mathbf{f}(t)}{2m}\delta t \tag{4.11}$$

With this method the velocity needs to be calculated in two steps, first for the current forces $\mathbf{f}(t)$ and then for the new forces $\mathbf{f}(t+\delta t)$ which are calculated from the new positions $\mathbf{r}(t+\delta t)$.

All the systems I simulated were equilibrated for 15 ps, something that is translated to 15,000 steps of 1 fs constant time-step of atomic jumps. I verified that this time is long enough in order the system to reach its equilibrium phase by analysing the system properties. The equilibration temperature was set at 300 K and the pressure at 1 atm, at which the simulated materials are in solid phase, by using the NPT Berendsen algorithm. For simulations with argon the initial equilibration temperature was at 10 K, since at 300 K the system is already transformed to gas. The lower cut-off parameter for long-range potential and the higher cut-off parameter for short-range potential calculations usually lie at a distance around the third neighbour distance. A longer distance will result to higher computational cost without providing any significant difference in the results, while shorter distance will decrease the computational cost but it will decrease the accuracy of the results.

After the equilibration, in order to prepare the structure in the solid

or liquid phase, depending on the material I set the temperature higher or lower for simulation time of 15 ps and under NVE ensemble. To prepare the system in the amorphous phase, after the initial melting, the system was cooled down rapidly. In order to be able to compare the simulations of the crystalline and the amorphous phase, the simulation temperature for both phases was set at 10 K. After the structure preparation and the necessary validation of my simulations I performed inelastic neutron simulations, as I describe in the following section, in order to study the collective excitation spectra for various materials.

4.2 INS simulations

The inelastic neutron scattering simulations were performed with the GULP software [95] and the phonon frequencies were calculated for each atom in the system over a wide **Q** range. A special module of GULP [96] was used to calculate the phonon dispersion curves for both crystalline and powder samples. GULP calculates the phonon density of states at a grid of points across the Brillouin zone by using the well known integration scheme developed by Monkhorst and Pack [97]. To calculate the phonon frequencies of a system, the starting point is the force constant matrix, given by the second derivative of the energy with respect to the atomic displacements in space. The forces were extracted from the MD simulations for each system in the solid, amorphous or liquid state.

Whilst the different phonon modes for single crystals are possible to be identified, the phonon modes from powder samples are considered to be very difficult or impossible unless during the refinement procedure there is a good starting model [98,99]. The critical factor for phonon density of states plots, apart from the resolution of the integration grid, is the system size. The continuous density of states curve has to be approximated by a series of finite regions of frequencies or boxes. Each phonon mode at each point in **k** space is assigned to the box whose frequency region falls into. The smaller the box size the better the resolution of the plot. However, more points are needed to maintain a smooth variation of number density.

4.2.1 Results

The two main materials I used in order to study the collective excitation spectra for the solid and amorphous phase are iron and argon. The system size was 1 Fe atom in bcc formation periodically repeated along all directions and 432 Fe atoms in amorphous phase. The phonon frequencies of the powder and the crystal were calculated for an already equilibrated system under constant volume conditions at very low temperature. The calculation for the crystalline phase was done over 100,000 different random **k** points and for the amorphous phase over 40,000 different random **k** points. For the crystal structure the orientation is known so there is no need for large statistical sample as there is in the amorphous and liquid structure. That makes the INS simulations of crystal structures less computationally demanding and much faster.

The interatomic potential I used to describe the atomic motion of iron is the extended Finnis−Sinclair model. The potential parameters for Fe and its elastic constants were found in the original extended Finnis−Sinclair potential publication [84]. The elastic constants for iron are very close to experimental ones and were used in the calculation of phonon frequencies in order to obtain more accurate results.

Similarly for argon, the system size was of 1 Ar atom in fcc formation periodically repeated along all directions for the crystalline phase and 256 Ar atoms in the amorphous phase. Again the phonon frequencies of the powder and the crystal were calculated for an already equilibrated system under constant volume conditions at very low temperature over 100,000 different random **k** points and for the amorphous phase over 10,000 different random **k** points. The interatomic potential used to describe the atomic motion of argon is the Lennard-Jones model and the potential parameters found in [20] and the experimental elastic constants were found in [100].

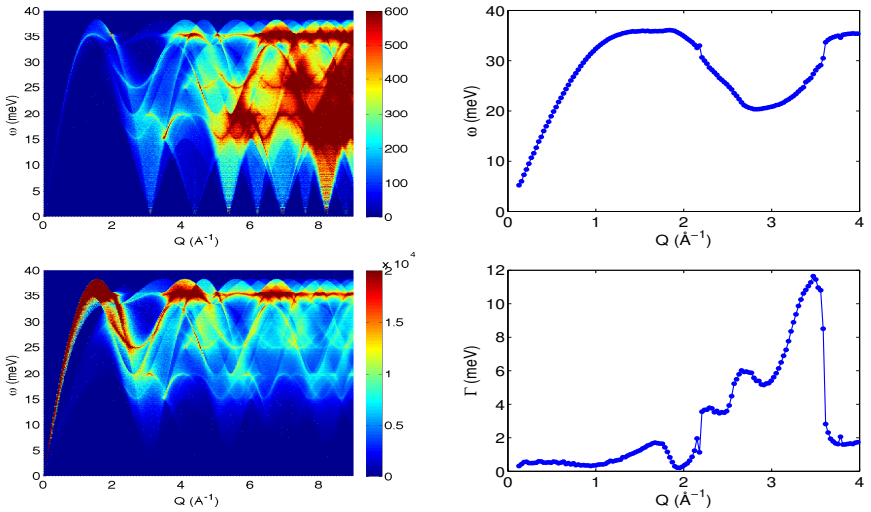

Figure 15: Fe bcc. Upper left: Collective excitation spectrum from INS simulations presenting the phonon frequencies over larger scattering vector regime. The colour map represents the intensity of scattered neutrons at every $\mathbf{Q}$ and ω. Bottom left: Collective excitation spectrum from INS simulations with intensity multiplied by $E^2/\mathbf{Q}^2$. Upper right: DHO fit of collective excitation spectrum from INS simulations with intensity multiplied by $E^2/\mathbf{Q}^2$ at the low and intermediate $\mathbf{Q}$ regime. Bottom right: Damping factor of the DHO fit.

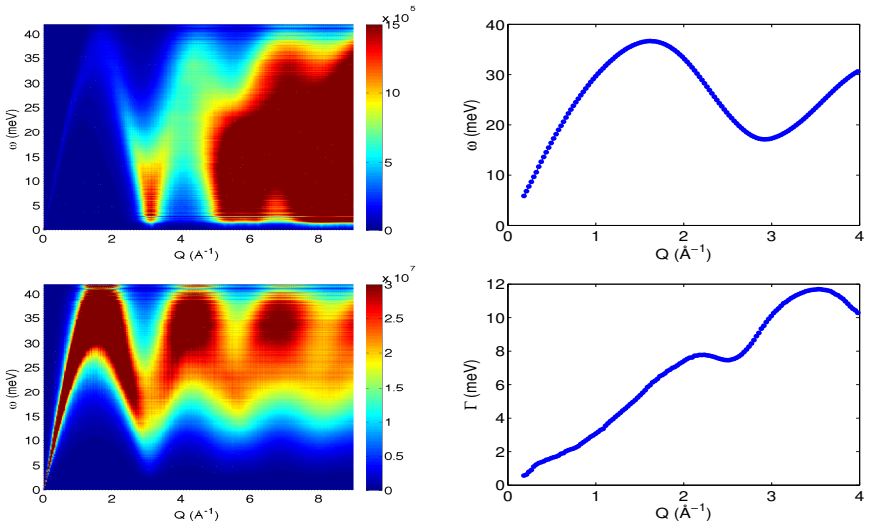

Figure 16: Fe amorphous. Description as caption in figure 15

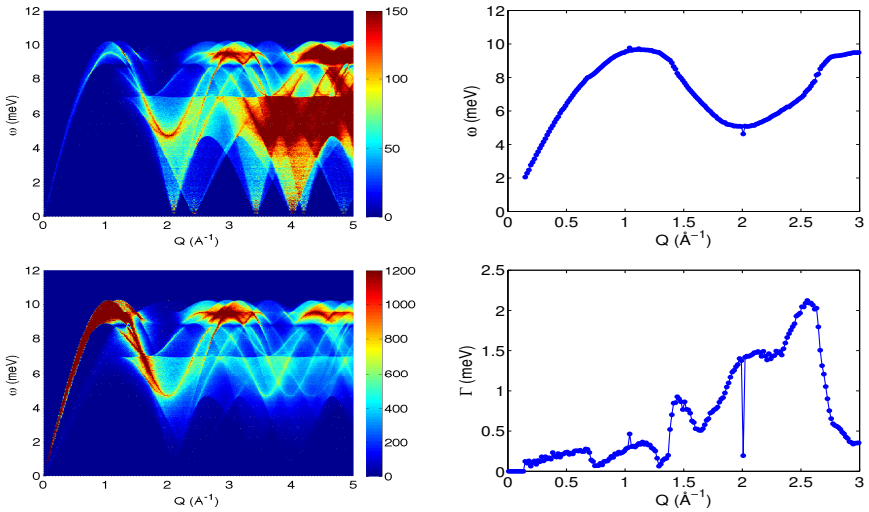

Figure 17: Ar fcc. Description as caption in figure 15

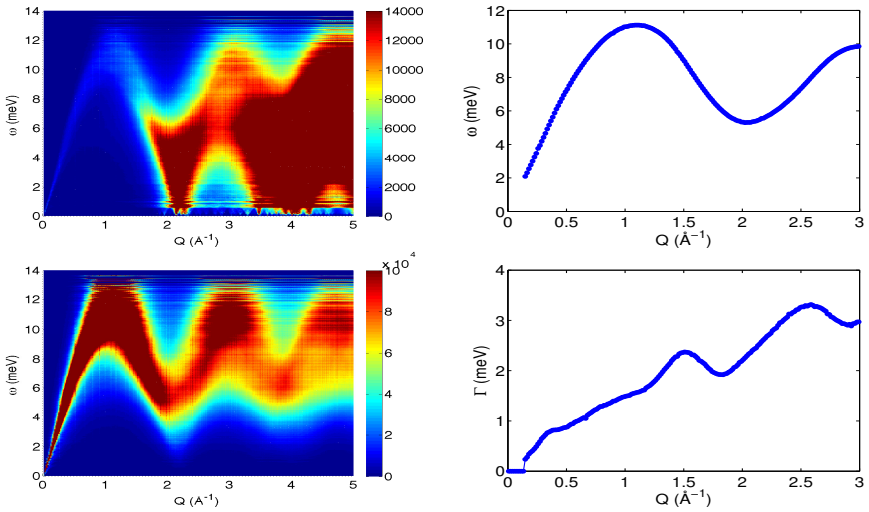

Figure 18: Ar amorphous. Description as caption in figure 15

The presented results follow the same sequence and similar analysis procedure followed in section 3.2 for the experimental INS results. In INS simulations the results come as 2-dimensional matrices of projections of the energy in the reciprocal space as function of momentum, $S(\mathbf{Q}, \omega)$, and there is no need for background subtraction. In figure 15 I present results for crystalline

iron, in figure 16 results for amorphous iron, in figure 17 results for crystalline argon and in figure 18 results for amorphous argon.

For all the previous figures, the upper left plot shows results of collective excitation spectra over a wide scattering vector range in a colour-scale map, as they were taken from INS simulations. The warmer colours represent higher intensity, which means more scattered neutrons for the specific combination of $\mathbf{Q}$ and ω, while the cold colours represent lower intensity. In contrast with results from INS experiments in section 3.2, only the positive energies were calculated and the energy loss part is waived as well as the elastic line at frequencies with zero value along the whole $\mathbf{Q}$ range. In the bottom left plot is the collective excitation spectra from INS simulations, with intensity $S(\mathbf{Q},\omega)$ multiplied by the $E^2/\mathbf{Q}^2$ factor. This is done to visualise better and obtain more intense results at the low $\mathbf{Q}$ region in order to study better the phonon−roton regime. The upper right plot shows the phonon frequencies from INS simulations, with the intensity $S(\mathbf{Q},\omega)$ multiplied by the $E^2/\mathbf{Q}^2$ factor, fitted with the DHO model at the low and intermediate $\mathbf{Q}$ regime, as I describe in section 3.2 and the equation 3.2. This equation involves the incident energy, the phonon energy and the damping factor which defines the damping of the fitted curve. The lower right plot shows the behaviour of the damping factor of the DHO fitting for the phonon frequencies at the low $\mathbf{Q}$ regime.

In INS simulations of crystalline iron, the system is treated as single crystal material. In single crystal materials the sample has specific orientation and it is easy to analyse the phonon dispersion curves and get clear results for each longitudinal and transverse wave along various directions. The phonon dispersion curves for Fe bcc from simulations are presented in figure 19. I used the GULP software to calculate the phonon frequencies for over 50 different $\mathbf{k}$ points along different planes, in order to plot accurately the dispersion curves. With Greek letters are denoted the intersection points, which are special $\mathbf{k}$ points that define the direction. Γ is the [0 0 0] point, H is the [1 0 0] point and N is the [1 1 0] point.

We can see that along the [0 0 ξ] direction from Γ to H there are two dispersion curves, one longitudinal and one transverse, with the longitudinal

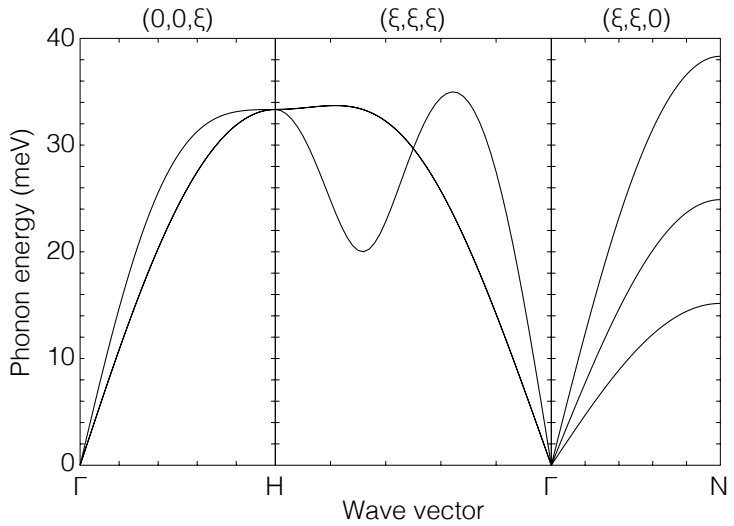

Figure 19: Phonon dispersion curves of Fe bcc system along various directions from INS simulations.

curve to be the one with slightly higher phonon energy over all points of the wave vector. Then is the (ξ ξ ξ) plane where the longitudinal dispersion curve initially creates a minimum and then it reaches energies higher than the transverse dispersion curve. As I discussed in section 3.3 and I will explain better in section 5.1 the two transverse acoustic modes have very identical frequencies and they are degenerate. As a result we can observe only one curve that describes both transverse acoustic modes. Finally, along the (0 ξ ξ) plane we can see two transverse dispersion curves and one longitudinal with higher energy than the two transverse curves. For the amorphous sample it is not possible to have a similar plot since the dispersion curves are not separated and a possible try for distinction would possibly lead to wrong results.

4.2.2 Summary and discussion

In INS simulations the intensity of the data depends on the number of **k** points in a similar way as experiments depend on the scattering time. Moreover in simulations there are no noise data and the results are clear,

even when the number of **k** points is small we can see results with better resolution than those from the INS experiments and better defined phonon dispersion curves. This can be seen especially in figures 15 and 17 where the crystalline samples are represented. For the amorphous phase we can see that the dispersion curves are not well defined but they are presented as an average of all dispersion curves. Still, high intensity simulations define clearly the characteristic areas of the dispersion curves, such as the initial linear increase at the low **Q** range and the phonon−roton regime after the first peak.

The DHO fit of the collective excitation spectra with intensity multiplied by the $E^2/\mathbf{Q}^2$ factor for both iron and argon give a well defined curve and exhibit clearly the photon-roton regime. Although for the amorphous samples the curves are smoother because of the averaging of all dispersion curves, the phonon−roton frequencies can be found at the same value of scattering vector as in crystalline samples. As we can see, the DHO fittings for the crystalline materials are not as smooth as those of the amorphous phase, something that can be attributed to the well defined dispersion curves that affect the fitting procedure. As I described in the previous chapter, the INS spectra for the liquid and amorphous phases provide an average over all dispersion curves and as a consequence the fitted data produce a smooth curve. Regardless of how smooth the curve is, the fitting is very accurate, something that is evaluated in figure 20 which I will analyse in the next paragraph.

The damping factor follows the same behaviour as in experiments in section 3.3. Γ has a **Q** dependance and it increases rapidly at higher **Q** values. For the INS simulations Γ exhibits much lower values with respect of the frequency than Γ calculated from the INS experiments. This verifies that the DHO fitting for results from INS simulations produces higher quality fitting than that of INS experiments. For simulations I do not discuss temperature dependance of Γ, since the simulations of the crystalline and the amorphous phase were performed at the same temperature.

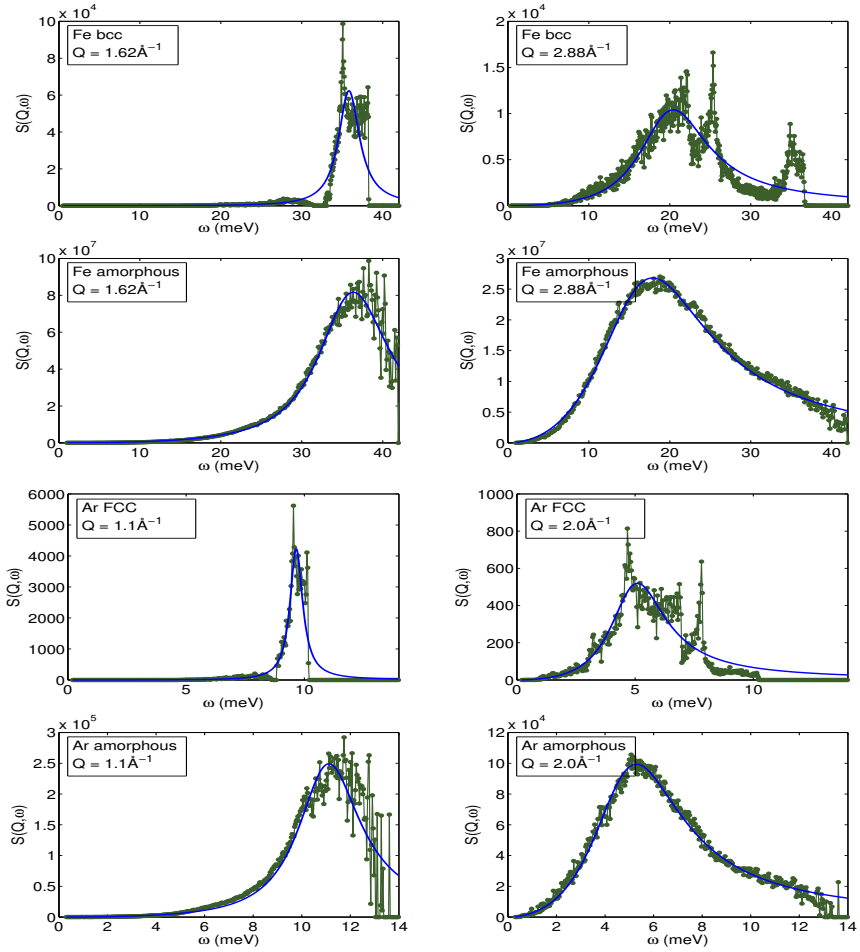

Figure 20: Intensity multiplied by $E^2/\mathbf{Q}^2$ with respect of energy for Fe at $\mathbf{Q}$ = 1.62 Å^{-1} and $\mathbf{Q}$ =1.88 Å^{-1} and for Ar at $\mathbf{Q}$ = 1.1 Å^{-1} and $\mathbf{Q}$ = 2.0 Å^{-1}. With green line and circle are represented the data from simulations and with blue line is the DHO fit.

In figure 20 I present results of the intensity with respect of phonon frequency for two different scattering vectors for both crystalline and amorphous phases of iron and argon. With green line and circles are the data from simulations multiplied by $E^2/\mathbf{Q}^2$ and with blue line is the fitted DHO curve. For iron the two chosen points are $\mathbf{Q}$ = 1.62 Å^{-1} and $\mathbf{Q}$ = 2.88 Å^{-1} and for argon are $\mathbf{Q}$ = 1.10 Å^{-1} and $\mathbf{Q}$ = 2.00 Å^{-1}. The first $\mathbf{Q}$ point for both iron and argon is the point where the DHO fit curve has its first maximum

and the second **Q** point is where the DHO fit curve has its minimum after the first maximum, where the phonon−roton regime is. For all eight plots of figure 20 we can see that the DHO fit represents very well the initial data. This verifies that the DHO fitted curves exhibit the phonon−roton minimum for both crystalline and amorphous phase and the minimum is at the same or very close **Q** point for the two phases, creating a connection between the crystalline, amorphous and liquid phase.

Further discussion about the phonon−roton minimum arises from figure 19. The dispersion curves of crystalline iron were drawn from results straight from simulations of phonon frequencies for various directions. The phonon−roton minimum is obvious along the [ξ ξ ξ] direction over the longitudinal dispersion mode. This is also verified from previous calculations of crystalline's iron phonon dispersion curves in literature, from INS experiments fitted with the Born-von Karman model [61,70], IXS experiments fitted with the Born-von Karman model [71,72] and simulations [73,74]. These results from literature verify the validity of my simulations since results for crystalline iron are not only qualitatively correct but also quantitatively accurate. This makes my simulations a good alternative tool to experiments to perform INS, getting at the same time higher intensity results about individual atoms, their motion and their structure.

To conclude for this section, I presented results from INS simulations for iron and argon for the crystalline and amorphous state. The amorphous state was used to describe the liquid state over the crystalline. Results for both iron and argon include collective excitations spectra from INS simulations, collective excitations spectra from INS simulations with intensity multiplied by the factor $E^2/\mathbf{Q}^2$ in order to present frequencies at the low **Q** regime more intense and be able to study the phonon−roton minima. Moreover DHO fits of the collective excitations spectra from INS simulations with intensity multiplied by the factor $E^2/\mathbf{Q}^2$ at the low **Q** regime, the damping factor, evaluation plots comparing the DHO fits with the initial data from simulations and for Fe bcc the phonon dispersion curves along various directions are included.

The results are in good agreement between the crystalline and amorphous

phases for various materials, including the calculation of the phonon−roton minimum at the same **Q** value. For the INS simulations the atomic structure used for describing the amorphous phase is identical with that of the liquid phase. As a consequence similar results can be extracted and direct comparison with the crystalline phase can be made. The existence of the phonon−roton minimum is verified for crystals as well as in the corresponding liquids, not only for specific materials but for a broad range of them.

In next chapter I present a theoretical explanation of this phenomenon and I discuss more about the origin of this minimum and how is related to specific systems. In the next paragraphs I present results verifying the connection between materials of different structures phases and explain their similarities. In the next section I present details from computational calculations for various materials, including Fe and Ar, about their local structure and population in order to discuss in depth the similarities of crystals and liquids.

4.3 Local structure analysis

In the previous section I discussed the connection between the crystalline state and the amorphous state regarding the similarity of their phonon−roton minima. I also concluded that the collective excitation spectra of the amorphous state is the same or at least very similar with the spectra of the liquid phase of the corresponding material. As I described in chapter 2, the connection between the amorphous and liquid state of the same material is based on the similarity in the structure, which for both is characterised by absence of long range order.

In this section I study the local structure of the crystalline, amorphous and liquid state of various materials and I describe how liquids keep similar local structure to the corresponding solid. This provides the relationship between the structure of the three phases and it gives a better understanding to what extend the connection of dynamics depends on the structure. Furthermore this comparison extends and justifies the model I propose in chapter 5 about the phonon−roton minimum of crystals to liquid systems.

Studying the local structure includes the study of both structural formation and the number of atoms in this formation. To get detailed results I performed classical MD simulations for various materials, studying the crystalline, amorphous and liquid structure. From MD simulations I will be able to study the short-range order and the local population in details. The materials I used for my calculations are argon, iron, potassium, molybdenum, tantalum and tungsten. As I already discussed, these materials (apart from argon) have similar crystalline structure and moreover exhibit clearly the phonon−roton minimum. Argon is being used as a comparison in order to verify that the procedure and the results are not structure dependent.

Every structure was prepared by using similar method as the one described earlier in section 4.1.2, starting with system equilibration under constant pressure and temperature conditions and then performing simulations under constant volume and energy conditions. For all materials the equilibration was performed at temperature at which each material is solid. Then I simulated the three different phases. For iron, apart from the standard equilibration method, another equilibration procedure was performed at higher temperature, at 4,000 K, where iron is melted. Then I simulated again the amorphous and liquid phase in order to understand how the equilibration method affects the structure.

The population and angle of bonds analysis do not require the simulation of large systems as in calculations of thermodynamical properties where the size of the system affects the results. The system size for all materials apart from argon is 432 atoms and for argon 256 atoms. All of the materials apart from argon form bcc crystalline structure while argon forms fcc crystalline structure. The interatomic potential for argon is the Lennard−Jones potential and the potential parameters found in [20]. The interatomic potential for iron, molybdenum, tantalum and tungsten is the extended Finnis−Sinclair potnetial and the potential parameters found in [84]. The interatomic potential for potassium is the Morse potential and the potential parameters found in [101].

The results for population analysis were extracted straight from the MD simulations with the DLPOLY software, while for the bond and angle analysis

special software was used. For all the simulations I performed, the results from population and bond analysis refer to the short-range distance. This is the same distance as that of the effective cut-off parameter of the interatomic potential, which usually lies between the second and third neighbour atom or further. Hence all the results extracted in this chapter are related to the local structure and the short-range order of the materials at the three different phases. Results for the long range order are not of interest in this chapter and might be very different from the results of the short-range order.

4.3.1 Population analysis

The population analysis includes results from pair distribution function (PDF) and the calculation of the nearest neighbour atoms (NNA). In section 2.1.1 I defined the PDF and explained its equation (equation 2.2). The NNA is defined as the definite integral of the equation 2.2 for a specific area, from r_1 to r_2.

$$n_{\mathrm{AB}}(r) = \int_{r_1}^{r_2} 4\pi r^2 \rho_{\mathrm{B}} g_{\mathrm{AB}}(r)\mathrm{dr} \tag{4.12}$$

where for two atom types A and B, n is the number of atoms of type B that can be found in a distance of radius r, ρ_{B} is the density of atoms B or the number of atoms per unit volume and $g(r)$ is the PDF. It is known that for bcc crystals the number of first neighbour atoms is 8 and the number of second neighbour atoms is 6, in total 14 atoms for the first two neighbour atoms. For fcc materials the number of first neighbour atoms is 12 and the number of second neighbour atoms is 6, in total 18 atoms for the first two neighbour atoms. For well defined structures, after MD simulations these numbers should be able to be reproduced accurately.

Results from PDF analysis for the crystalline phase should always exhibit sharp and well defined peaks. Every peak shows the number of neighbour atoms and the distance between them. The probability of finding a number of atoms at a distance is defined by the height of the peak and is a system related property. The distance between the peaks is defined as the distance between neighbour atoms and each peak and is characteristic for each material. The width of each peak shows the possible distances that each neighbour atom

can be found and it allows us to understand how the atoms in the system are aligned and how much freedom have to vibrate around a position.

In figure 21 I present results for iron. In the upper left plot I present results for the PDF for the three structural phases combined. As I mentioned earlier for iron I performed two different equilibration methods at two different temperatures. The amorphous and liquid phase that were initially equilibrated at 4,000 K are stated in the plot as amorphous "(liq. equil.)" and liquid "(liq. equil.)".

We can see that as it is predicted by the theory, for crystals the peaks are sharp and narrow which means that the structure is well defined and follows a pattern over the system. For the amorphous and liquid phase the peaks are not sharp and much lower than the crystalline peaks. The curves are very broad and they never go to zero as it happens with the crystalline curve. That means that there is not clear distinction between the nearest atoms, even though they exhibit peaks that show the higher possibilities to find the nearest neighbour atoms. The curve for the liquid phase is even lower than the one in the amorphous phase and the peaks even broader.

I should mention that the peaks for the crystalline, amorphous and liquid phase can be found around the same distance for the first peak. The amorphous and liquid state exhibit very broad peaks which cover more than one crystalline peaks, which means that include more than the first nearest neighbours. Nevertheless, we can observe that the amorphous and liquid phases follow a pattern similar to this of crystalline's phase. Moreover, we can observe that the equilibration temperature does not affect the results and the system keeps its properties even if the system is treated initially only with insignificant differences.

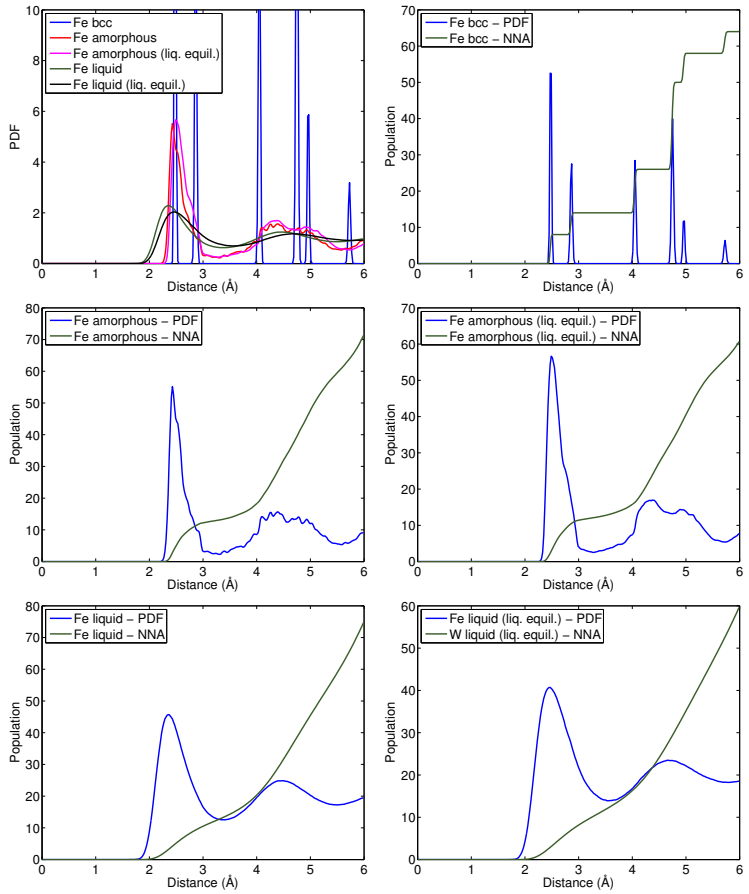

Figure 21: Population analysis for a system of 432 atoms of Fe. An equilibration of the system was performed at 10 K where the system is in solid phase and a different equilibration of the system was performed at 4,000 K were the system is in liquid phase. Results from the equilibration at higher temperature are noted as "(liq. equil.)". The upper left plot shows the pair distribution function (PDF) for the solid, amorphous and liquid phase for both different equilibrations. The PDF and the nearest neighbour atoms (NNA) are presented for the crystalline phase in the upper right plot, for the amorphous phase in the middle left plot, for the amorphous phase equilibrated at higher temperature in the middle right plot, for the liquid phase in the lower left plot and for the liquid phase equilibrated at higher temperature in the lower right plot. In plots where the NNA curve is present, the results for the PDF are multiplied by a factor of 2, 10 and 20 for the bcc, amorphous and liquid phase respectively.

The rest of the plots in figure 21 compare the PDF analysis with the NNA

analysis for the various structural phases. The data presented in the upper right plot are for the crystalline phase, in the middle left plot are for the amorphous phase for a system initially equilibrated at 300 K, in the middle right plot are for the amorphous phase for a system initially equilibrated at 4,000 K, in the lower left plot are for the liquid phase for a system initially equilibrated at 300 K and in the lower right plot are for the liquid phase for a system initially equilibrated at 4,000 K. In these plots the results presented for the PDF are multiplied by a factor of 2 for the crystalline phase, by a factor of 10 for the amorphous phase and by a factor of 20 for the liquid phase. This was done in order to visually compare easier the PDF with the NNA curve.

The upper right plot in figure 21 represents the bcc phase and the curve that describes the number of NNA has a steep increase at distances that the PDF exhibits peaks, while for the rest distances the NNA curve exhibits a plateau, showing that the number of nearest neighbour atoms is stable at these plateaus. Quantitatively the NNA curve shows that the material has bcc structure because the first plateau is at 8 atoms and the second at 14 atoms, following the theory for the case of bcc materials. The middle left and middle right plots in figure 21 present the PDF and the NNA curves for the amorphous phase. The NNA curve exhibits smoother transitions than the one for the crystalline phase without having steep increases and straight plateau. For distances around the first PDF peak, we can see a rapid increase of the number of nearest neighbour atoms and after that a much smaller increase, till the distances around the second PDF peak where there is again a rapid increase. This pattern is similar to the one of the crystalline's phase. Moreover, the NNA curve for the amorphous phase initially equilibrated as solid and the NNA curve for the amorphous phase initially equilibrated as liquid do not show any difference, verifying that the initial equilibration does not affect the properties of the system.

Similarly with the amorphous phase, the liquid phase in the lower left and lower right plots in figure 21 exhibit a very smooth curve related to crystalline phase. The NNA curve shows an almost linear increase, with minor distinctions in the change of the angle of the curve. Moreover, as it

was shown for the amorphous phase, the equilibration does not affect the results for the liquid structure. It is worth noticing that for all three phases the final population of the system at around 6 Å has the same value.

Another way to study if and how simulations at various temperatures affect the structure and if the system keeps a memory of its motion, is by studying the velocity correlation function (VCF) (also known as velocity autocorrelation function) of iron from simulations at various temperatures. The VCF is a time dependent correlation function and is important because it reveals information of the dynamical processes operating in a system and it describes the correlation of an atom's velocity with time. For a system of N atoms the VCF is defined as

$$G(t) = \langle \mathbf{v_i}(t_0) \cdot \mathbf{v_i}(t_0 + t) \rangle = \frac{1}{N} \sum_{i}^{N} \frac{1}{t_{\max}} \sum_{t_0=1}^{t_{\max}} \mathbf{v_i}(t_0) \cdot \mathbf{v_i}(t_0 + t) \qquad (4.13)$$

where $\mathbf{v_i}$ is the velocity of an atom i, t_0 is the initial step of the simulation, t is a future step and $t_{\max}$ is the final step.

According to Newton's law of motion, if an atom does not interact with the other atoms in the system then this atom will retain its velocity for all time. That would mean that the VCF would be maximum at all time, since the atom's velocity will not loose its correlation with the initial velocity. In high density systems, such as solids and liquids, there are strong interactions between the atoms. In these systems, the atoms by nature tend to be allocated in the most energetically stable state. At the stable state there is a balance between repulsive and attractive forces. In solids these locations are extremely stable and the atoms cannot escape easily from their positions. Their motion is described by an oscillation because the atoms vibrate towards the repulsive forces or towards the attractive forces, reversing their velocity at the end of each oscillation. The oscillations will not be of equal magnitude but will decay in time because there are remaining perturbative forces acting on the atoms disrupting a perfect oscillation and result in a damped harmonic oscillation. I should mention that the decay of the correlation function reflects the decay in the correlations in atomic motion

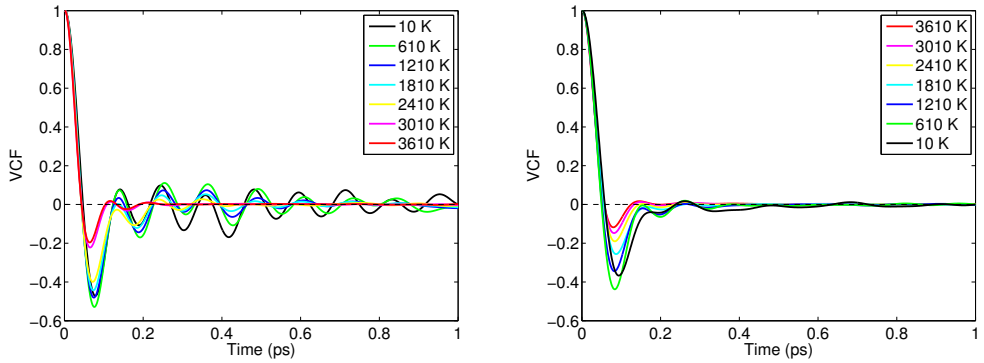

Figure 22: Velocity correlation function (VCF) for Fe. The left plot presents the VCF for simulations at increasing temperatures, for system initially equilibrated at 10 K (solid). The right plot presents the VCF for simulations at decreasing temperatures, for system initially equilibrated at 4,000 K (liquid)

.

along the trajectories of the atoms and not the decay in the amplitude of the velocity of the atoms.

In figure 22 I present the VCF for iron from simulations at various temperatures. As I described earlier the system of iron was equilibrated at two different temperatures, at 300 K and at 4,000 K, in order to describe an equilibration in solid phase and one equilibration in liquid phase. The results for the VCF for iron are for a system of 2,000 atoms, system bigger than the one used for the calculations of the population, which provides larger statistical sample and more precise results. In the left plot in figure 22 I present results for iron with initial equilibration at 300 K at various increasing temperatures in a range of 10 K to 3610 K. In this range the system changes from the crystalline to liquid phase. In the right plot in figure 22 I present results for iron with initial equilibration at 4,000 K at various decreasing temperatures in a range of 3,610 K to 10 K. In this range the system changes from the liquid phase to amorphous phase.

As we can see for both plots of figure 22 the VCF curves start at a maximum correlation of 1 at the initial simulation step and then decrease rapidly till they reach negative values and start oscillating from positive to negative values and back again behaving like a damped harmonic oscillator.

Finally the VCF curves tend to go to zero for long simulation time, something that was expected from theory and it means that any velocity correlation has been eliminated. From the left plot we can see that the damping is smaller than the damping in the right plot and the correlation in the velocity lasts for longer time. For both plots we can see that the correlation in velocity is higher at temperatures of 2,410 K or lower while at 3,010 K and over the damping is higher and the VCF curves tend to zero at less time. This is related to the structural phase of the material that changes at a temperature between 2,410 K and 3,010 K.

In my simulations, for the specific system of iron and with the specific interatomic potential the melting point of iron is around 2,800 K. Knowing that, we can conclude that the liquid phase loses memory of the atomic motion slightly faster than the solid phase. Also we can see that the VCF curves of the crystalline phase (left plot from 10 K to 2,410 K) and the VCF curves of the amorphous phase (right plot from 2,410 K to 10 K) are very similar. Nevertheless, even for the crystalline or amorphous phase where the correlation lasts longer, long enough simulations do not affect the structure since there are no remaining memory effects and any initial attributions are eliminated.

In figures 23, 24, 25,26 and 27 I present results from population analysis of argon, potassium, molybdenum, tantalum and tungsten respectively, showing the PDF and the NNA curves for the crystalline, amorphous and liquid phase. In these figures we can see similar results with those of figure 21, hence we can make similar conclusions. It is interesting to mention that the crystalline phase for K and Mo does not express results similar to these expected from theory. The PDF peaks for the crystalline phase are not sharp or narrow and they do not exhibit a zero value for distances between the first and second nearest neighbour atoms. Hence, I do not expect the other two phases to be described accurately.

This can be seen as well in the NNA curve of the bcc phase for these two materials, where the curve looks smoother and the area of rapid increase and the straight plateau is not well separated, as it is for argon, tantalum and tungsten. This is something that is attributed to the interatomic poten-

tial parameters that are not fitted to describe a system like this, relatively small and without surface. Nevertheless, even if these two systems are not described accurately the results are consistent for all three phases which is the main point of this study.

It is worth mentioning that the experimental melting temperature for Mo is at 2,896 K while the melting of the system in simulations was achieved for temperature over 14,000 K. During MD simulations, system's physical properties are expected to diverge from the experimental values and usually the smaller the system the higher the diversion. Still, this high difference as molybdenum's melting temperature was not observed in the simulations of the other materials.

To summarise, I performed MD simulations and examined the local population of various small systems in order to understand the similarities of the crystalline, amorphous and liquid phase. Results include pair distribution function analysis and the nearest neighbour atom analysis at short-range distances for all materials for all three phases. For the case of iron, the system was examined thoroughly to see if simulation parameters affect the results. I verified that the equilibration temperature and the simulation time do not affect the system and that the simulated system behaves very similarly for all three phases, exhibiting similar behaviour for the velocity correlation. The PDF curves of the amorphous and liquid phase show similar behaviour and both phases follow the behaviour of the PDF curve of the corresponding crystal but for broader range. Still, for short-range distances a system holds the same total number of neighbour atoms in all three phases, making clear that the local population for the crystalline, amorphous and liquid phase is the same and the three phases are strongly related.

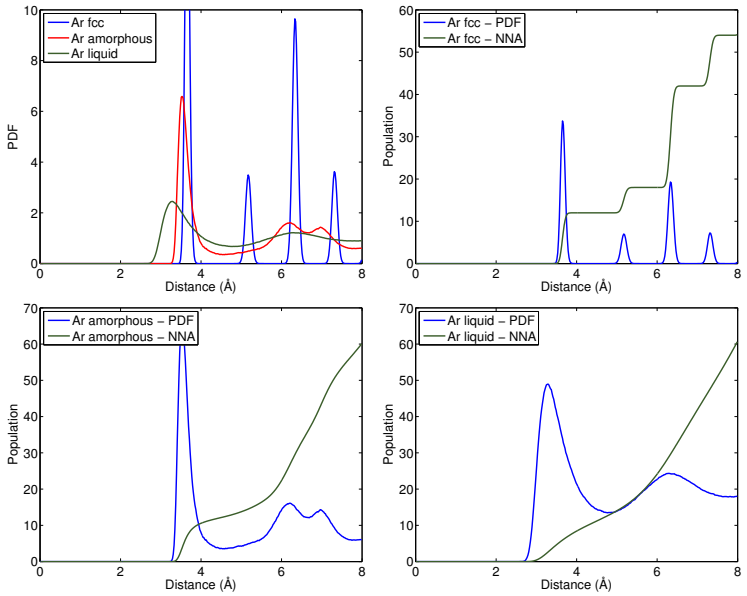

Figure 23: Population analysis for a system of 256 atoms of Ar. The upper left plot shows the pair distribution function (PDF) for the solid, amorphous and liquid phase. The PDF and the nearest neighbour atoms (NNA) curves are presented for the crystalline phase in the upper right plot, for the amorphous phase in the lower left plot and for the liquid phase in the lower right plot. In plots where the NNA curve is present, the results for the PDF are multiplied by a factor of 2, 10 and 20 for the bcc, amorphous and liquid phase respectively.

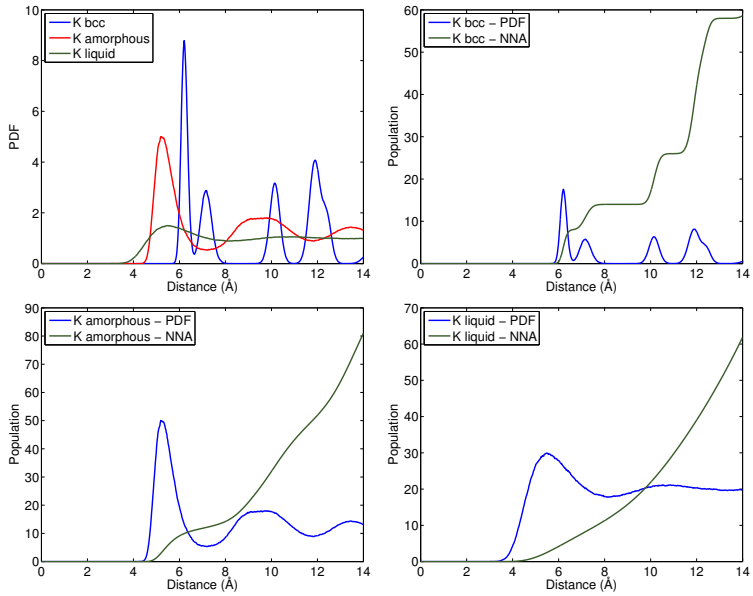

Figure 24: Population analysis for a system of 432 atoms of K. Description as caption in figure 23.

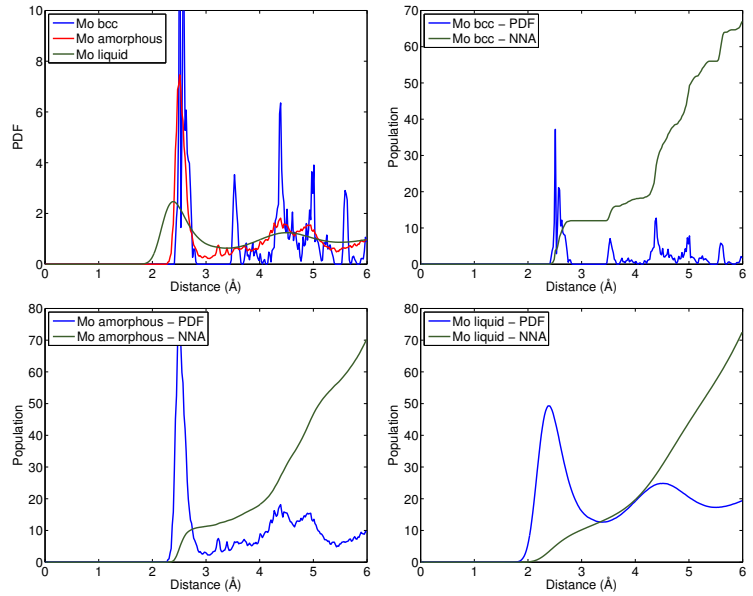

Figure 25: Population analysis for a system of 432 atoms of Mo. Description as caption in figure 23.

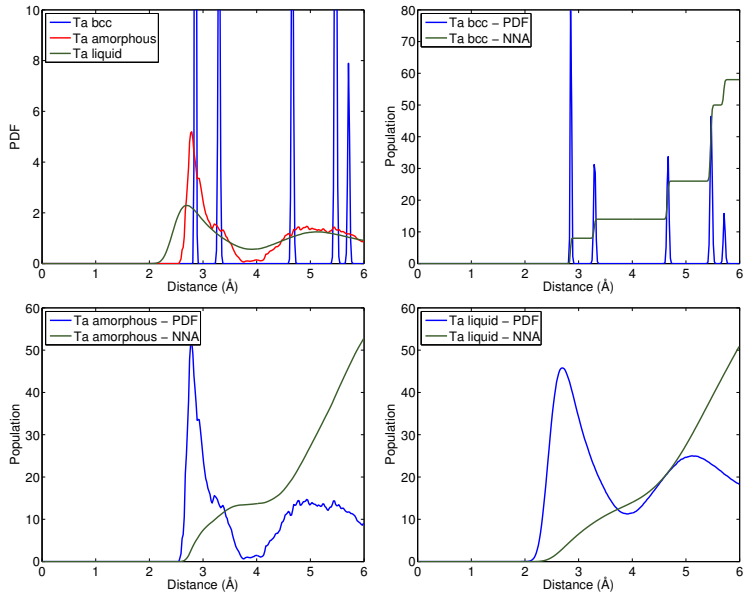

Figure 26: Population analysis for a system of 432 atoms of Ta. Description as caption in figure 23.

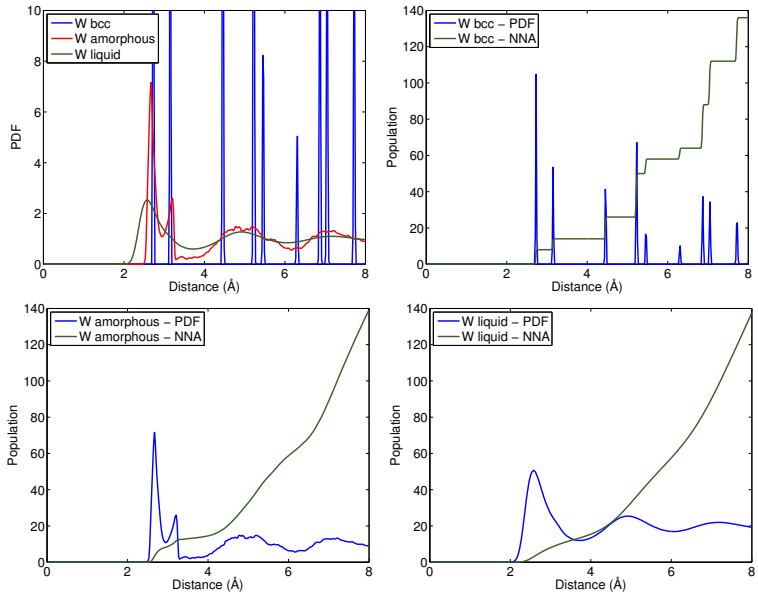

Figure 27: Population analysis for a system of 432 atoms of W. Description as caption in figure 23.

4.3.2 Angle analysis

The population analysis gives a good estimation of how crystals, amorphous and liquid structures of the same material keep the same number of atoms in short-range distances. To investigate further I analysed the local structure to understand if the short-range structure remains the same for the three phases. If the crystal structure is known for a material it is easy to calculate the angle between two bonds of an atom along the various directions for a 3-dimensional system. The angles for a crystalline material are characteristic and they are being repeated since there is periodicity in the system. From the population analysis it is clear that the local population is very similar for the three phases, so if the bonds between atoms along various directions for all phases form the same angle then we can conclude that in short-range distances a material has very similar local structure for the three phases.

For the seven systems I discussed in the previous section I used the data2config software, provided by Prof Martin Dove, to calculate the angles between two pairs of atoms of specific distance. The cut-off for this distance was estimated from the PDF for the crystalline phase and it corresponds to the first neighbour atoms distance. The same cut-off was used to calculate the angle between the two pairs of atoms in the amorphous and liquid phase for the same material. That means that the calculated angle is between an atom and its two closest atoms. For bcc materials an atom in the unit cell has 8 neighbour atoms. Taking as a starting point any of these 8 neighbour atoms, the middle atom will form 3 characteristic angles between the initial atom, itself and the rest 7 neighbour atoms. The angles are 70.53°, 109.47° and 180.00°. Similarly for a fcc system, any atom has 12 nearest neighbour atoms. The angles that the initial atom with its closest neighbour atom and the rest first nearest atoms are 60.00°, 90.00°, 120.00° and 180.00°.

The previous values are for ideal crystals. After MD simulations, where the atoms are allowed to move for long time, the angles between atoms in crystals are expected to be similar to the theoretical angles but usually they are not exactly the same. That means that even for the crystalline phase the

expected angles will have some degree of freedom and they will vary close to the theoretical value. This degree of freedom will be higher for amorphous materials and liquids since the atoms have higher degree of freedom in their motion.

In figures 28, 29, 30, 31, 32 and 33 I present histograms of the characteristic angles between two bonds of nearest atoms and the value of the cosine of these angles for iron, argon, potassium, molybdenum, tantalum and tungsten respectively. The left histograms in all figures show the angle that the pairs of bonds in the system form and how many pairs of bonds being formed for every angle. The two pairs of bonds include one atom and its two nearest neighbour atoms and the calculation was done for the whole system and all possible bonds. All the angles in the system are calculated for a range from 0° to 180°.

All the right histograms in all figures show the same results as the left histograms but the horizontal axis presents the cosine of the angle in range from -1 to 1. For my studies the cosine of an angle gives a better representation of the characteristic angles between atoms. As I explained, due to atomic vibration during MD simulations the atoms are displaced from their equilibrium position. As a result the angle between atoms are very close to the angles predicted from theory but not the same. The calculation of the cosine of the angles summarises all the similar angles and provides results for small groups of angles and gives a better understanding about the main angle that the atoms move around.

The figure 28 shows results for a system of 432 iron atoms. The first row of histograms presents the angle and the number of pairs of bonds that form this angle for the crystalline phase. The second row of histograms presents the amorphous phase for iron initially equilibrated in solid state, the third row presents the amorphous phase for iron initially equilibrated in liquid state, the forth row presents the liquid phase for iron initially equilibrated in solid state and the fifth row presents the liquid phase for iron initially equilibrated in liquid state.

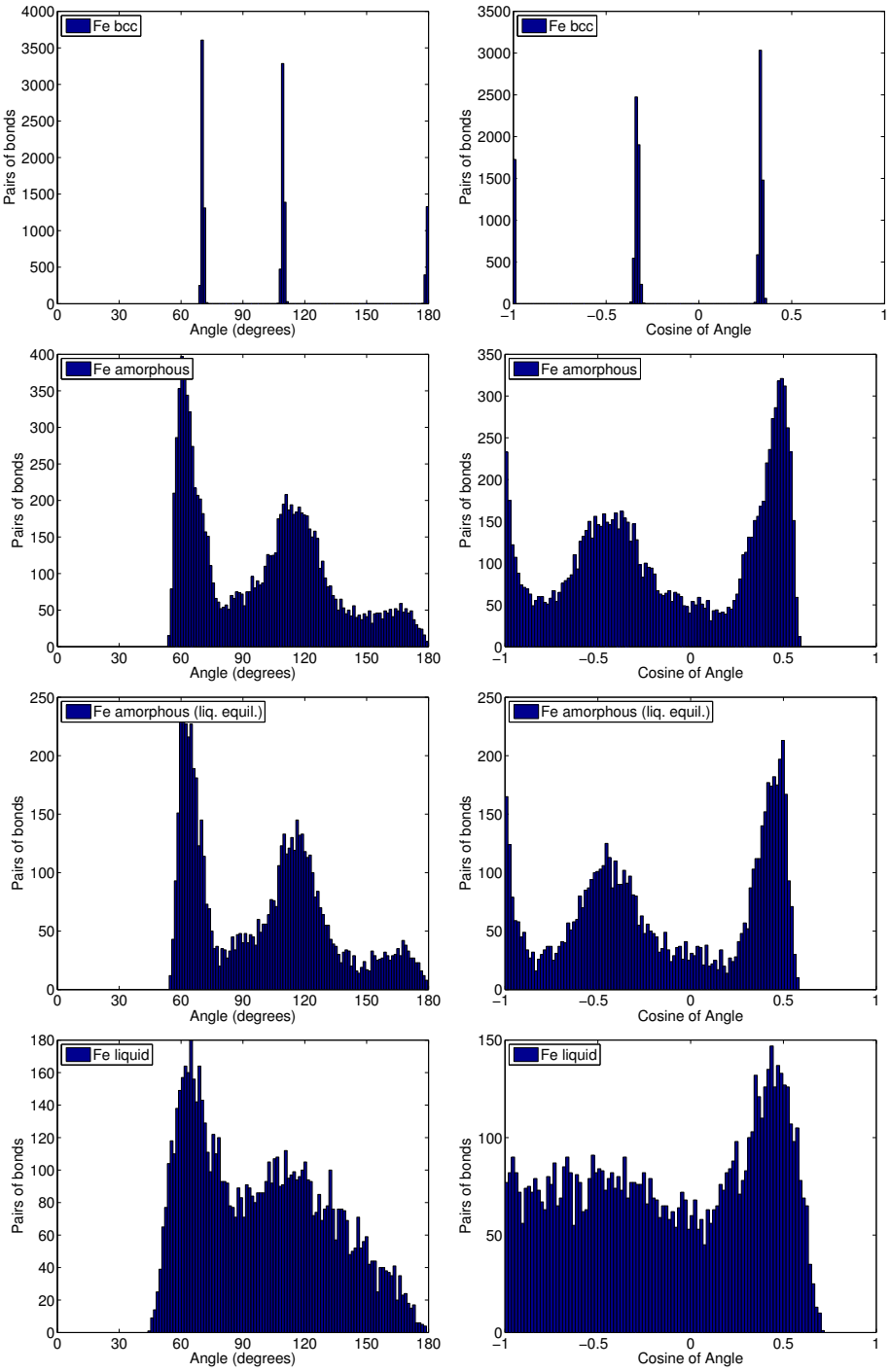
Fe bcc
Pairs of bonds
Angle (degrees)
Fe bcc
Pairs of bonds
Cosine of Angle
Fe amorphous
Pairs of bonds
Angle (degrees)
Fe amorphous
Pairs of bonds
Cosine of Angle
Fe amorphous (liq. equil.)
Pairs of bonds
Angle (degrees)
Fe amorphous (liq. equil.)
Pairs of bonds
Cosine of Angle
Fe liquid
Pairs of bonds
Angle (degrees)
Fe liquid
Pairs of bonds
Cosine of Angle

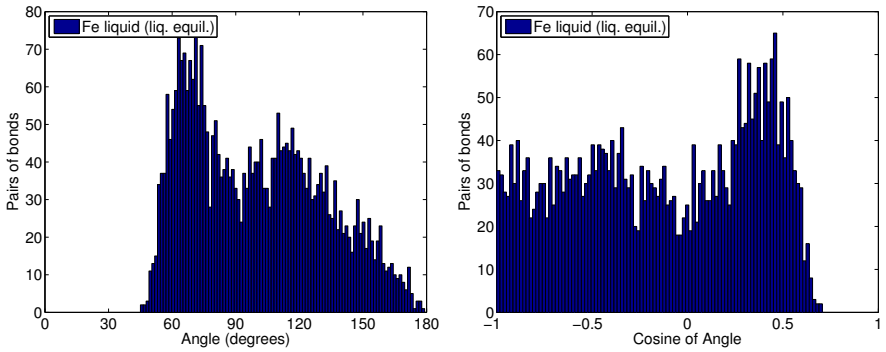

Figure 28: Characteristic angles between pairs of nearest Fe atoms in a system. The left histograms present the angles between pairs of bonds form in the system and the right histograms present the value of the cosine of these angles. The first row of histograms presents results for the crystalline phase, the second row presents results for the amorphous phase, the third row presents results for the amorphous phase for iron initially equilibrated as liquid, the fourth row presents results for the liquid phase and the fifth row presents results for the liquid phase for iron initially equilibrated as liquid.

We can see that for the crystalline phase the results exhibit very sharp peaks and they exhibit only three different angles, similar to the ones predicted from theory for bcc materials. For the amorphous phase we can see that the results show many different angles. We can see two main broad peaks of which the majority of bonds form angles that are similar to the angles of the crystalline phase. The importance of the calculation of the cosine of the angle can be seen in the amorphous phase where angles of 180° are not obvious because of the broader range of angles. By calculating the cosine of the angle we can see that there are three peaks formed for values similar to the crystalline phase and the results are comparable. For the amorphous phase initially equilibrated as liquid we can see very similar results but perhaps the peaks are slightly less broad. Still the characteristic angles are very similar to the amorphous phase initially equilibrated as solid and to the crystalline phase.

The liquid phase shows results of much broader angles than in the amorphous phase. For angles between 0° and 180° we can see two main peaks and even after calculating the cosine of the angles there are no well defined peaks

apart from one. Nevertheless we can see that the number of pairs of bonds for the liquid phase follow a pattern similar to the one for the amorphous phase. Very similar results we can see for the liquid phase initially equilibrated as liquid but again as for the amorphous case, the peaks now are slightly less broad and they form better defined peaks.

Similar is the description for figures 29, 30, 31, 32 and 33 for Ar, K, Mo, Ta and W respectively for the crystalline, amorphous and liquid phase. The only difference is that all the systems were equilibrated only in the solid phase, as described in the previous section. Results for crystalline Argon in figure 29 show all four characteristic angles between bonds of nearest neighbour atoms. For the amorphous phase, due to the broadening of the angle spectrum the two angles corresponding to 90° and 120° are not well separated. For the liquid phase the peaks corresponding to 90° and 120° are not obvious and only one peak closer to 120° is obvious. Again, the calculation of the cosine of the angle helps to exhibit better the angle at 180°.

In figure 30 I present results for potassium. The crystalline phase exhibits well defined characteristic angles for bcc materials between pairs of bonds of the nearest neighbour atoms, although the peaks are broader than expected. The amorphous phase exhibits even broader peaks but still well defined, something that is easier to understand from the right-hand side graphs of the cosine of the angles. It is clear that in the calculation of the angles there are more than just the nearest neighbour atom bonds included. From the liquid phase we cannot extract clear results since the angles do not follow a pattern.

In figure 31 we can see that results for molybdenum are not the expected ones, notably for the crystalline phase. For a bcc material only three different angles were expected and not five as can be seen in the histogram. Although it is not very clear it can be seen as well for the amorphous and the liquid phase, showing a consistency in this anomalous behaviour. These anomalous results additionally to the anomalous results from the population analysis of Mo in the previous section verify the bad quality potential parameters that do not describe accurately the system.

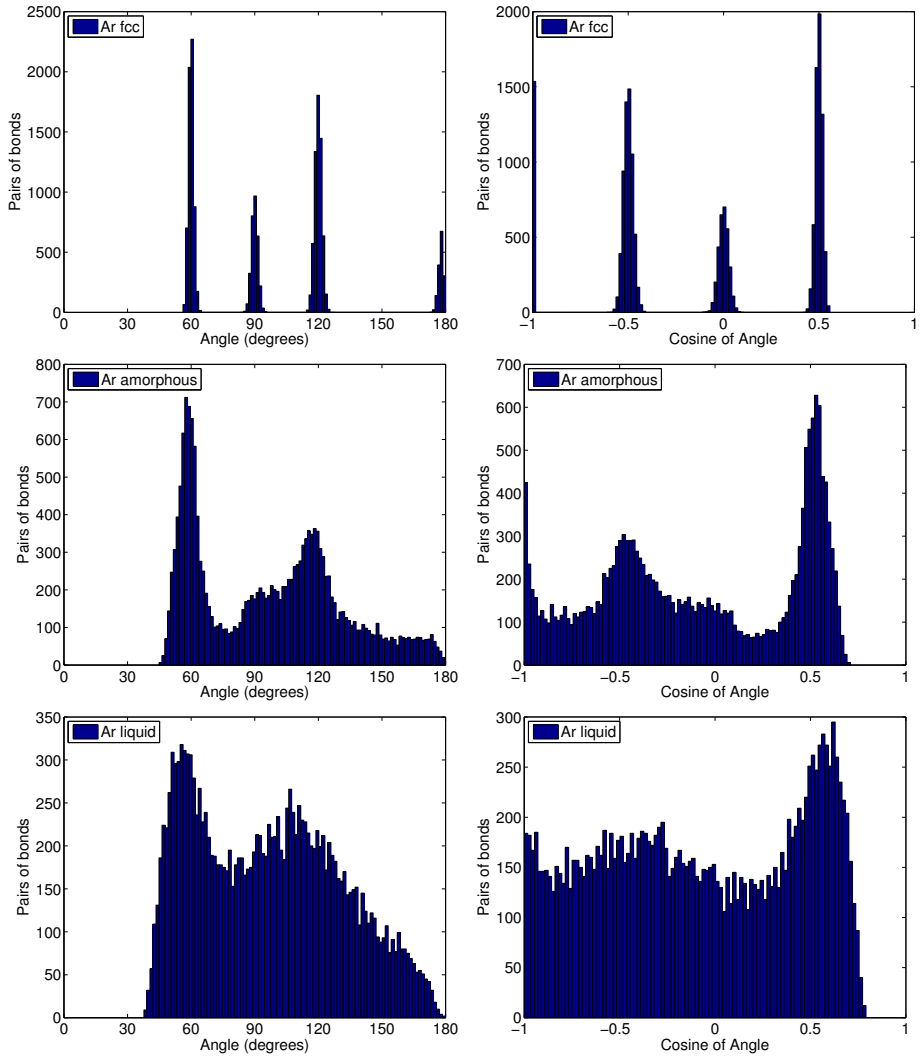

Figure 29: Characteristic angles between pairs of nearest Ar atoms in a system. The left histograms present the angles between pairs of bonds form in the system and the right histograms present the value of the cosine of these angles. The upper histograms presents results for the crystalline phase, the middle histograms presents results for the amorphous phase and the lower histograms presents results for the liquid phase.

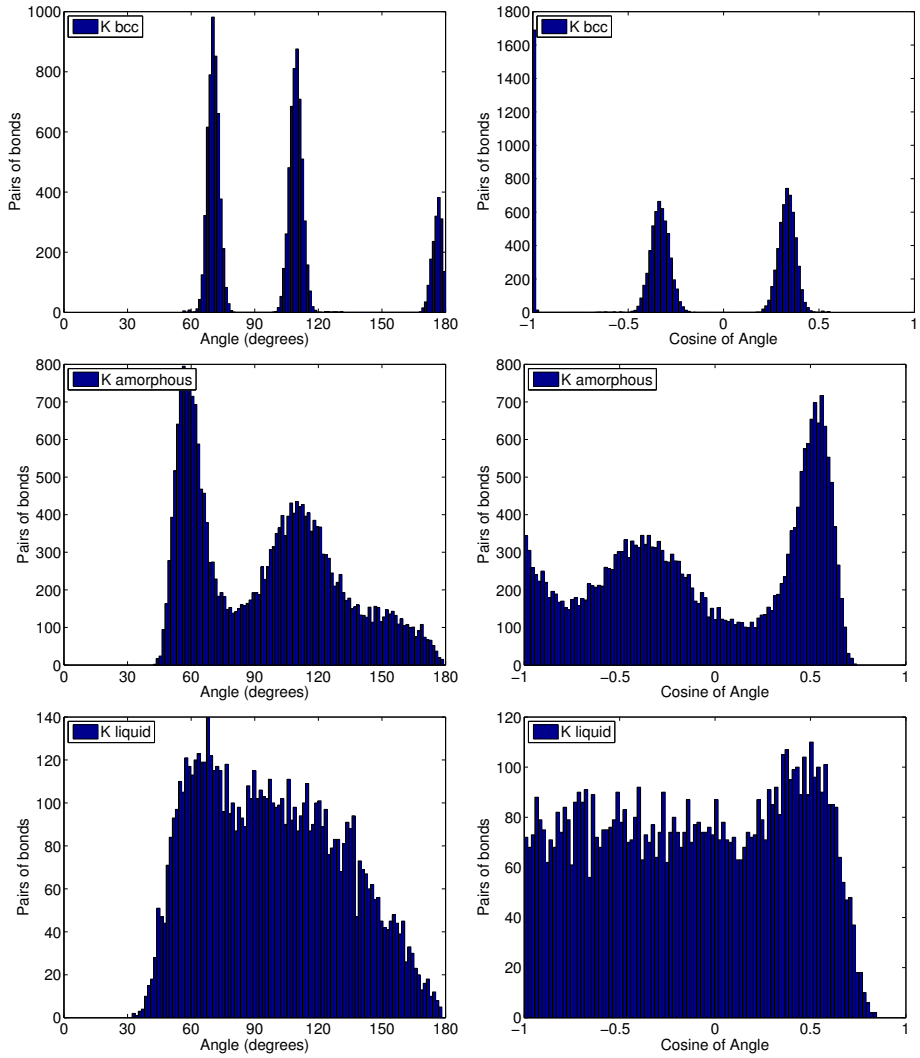

Figure 30: Characteristic angles between pairs of nearest K atoms in a system. Description as caption in figure 29.

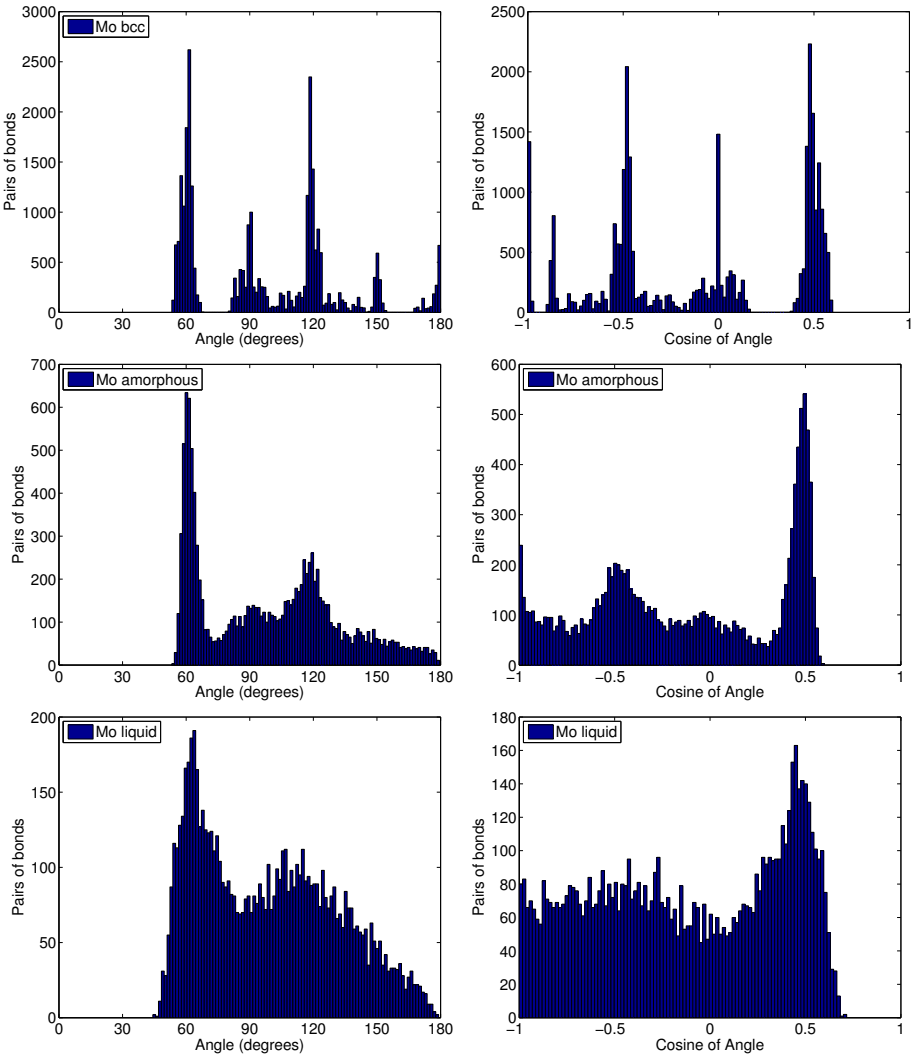

Figure 31: Characteristic angles between pairs of nearest Mo atoms in a system. Description as caption in figure 29.

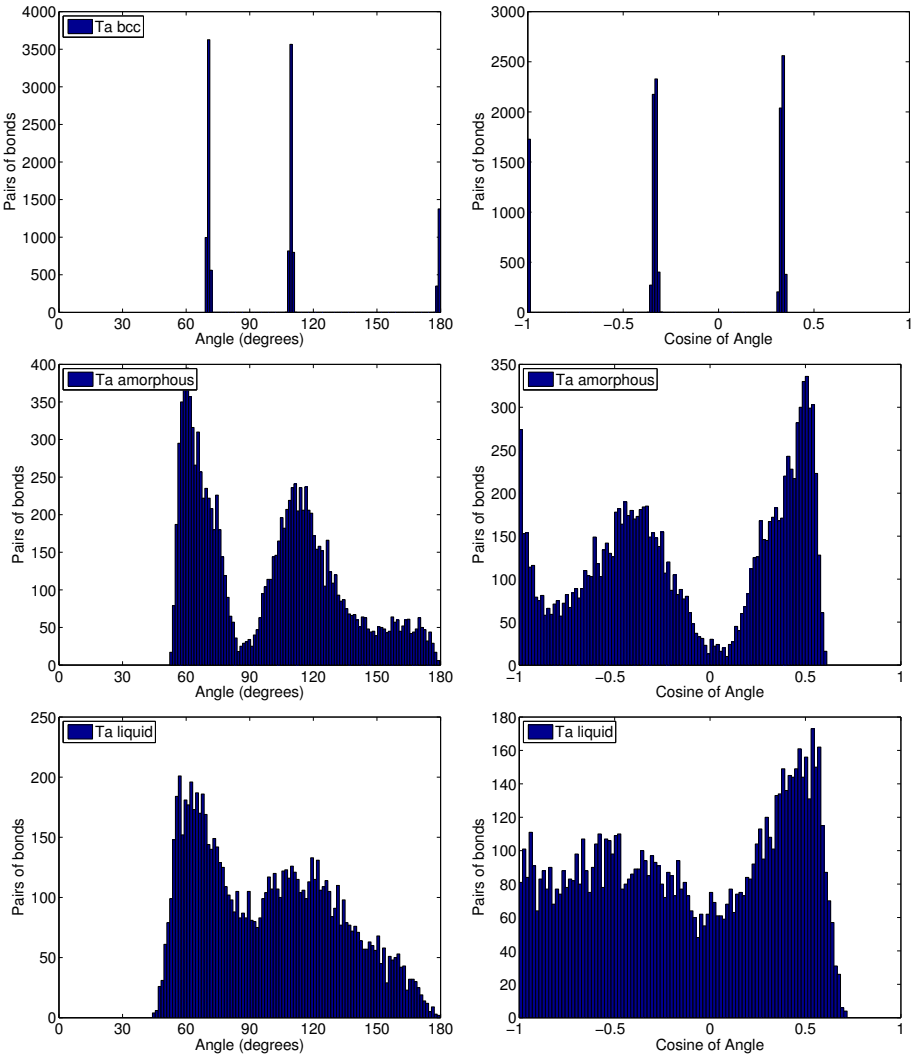

Figure 32: Characteristic angles between pairs of nearest Ta atoms in a system. Description as caption in figure 29.

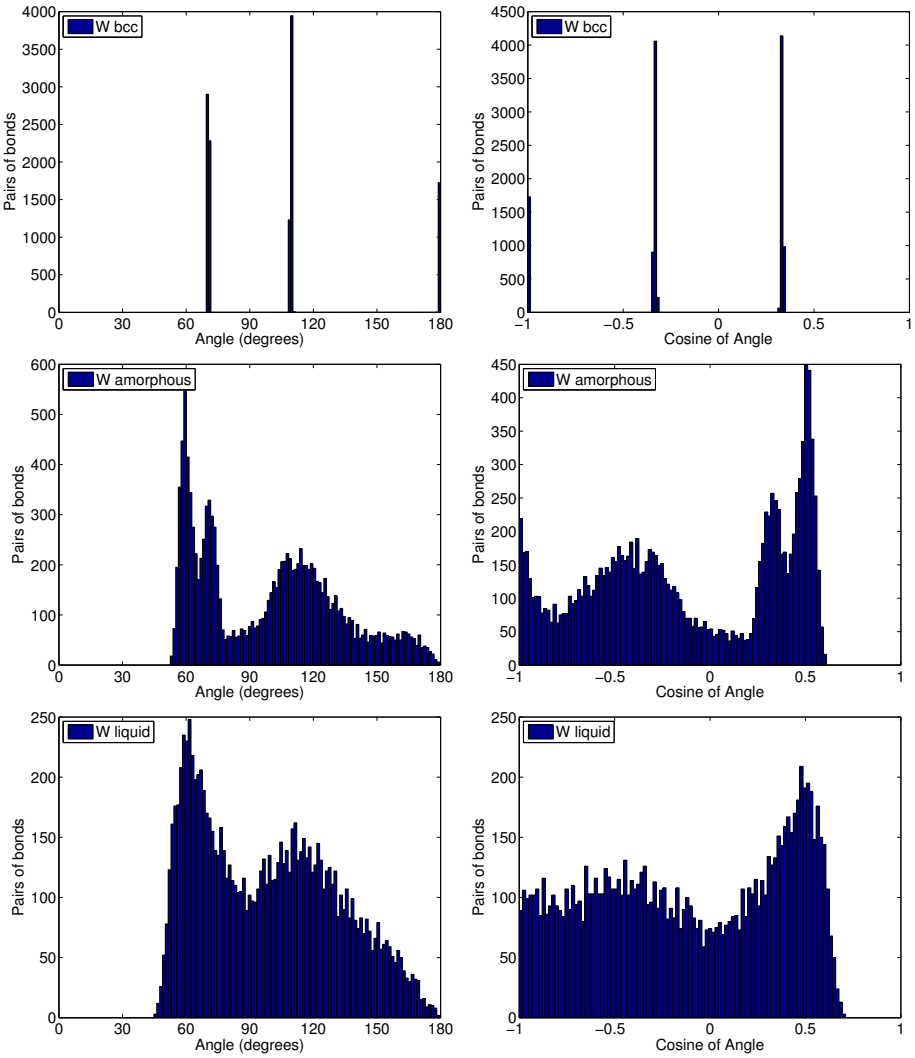

Figure 33: Characteristic angles between pairs of nearest W atoms in a system. Description as caption in figure 29.

In figure 32 tantalum behaves as it is predicted from theory. The crystalline phase has well defined angles between pairs of bonds for the nearest neighbour atoms. The amorphous phase exhibits a broader spectrum of angles but still the three peaks correspond to similar angles as in crystalline phase. For the liquid phase the angle spectrum is broader and although not all the peaks are well defined, the number of pairs of bonds tend to follow a trend similar to that of the amorphous and crystalline phase.

In figure 33 crystalline tungsten exhibits well defined peaks for the characteristic angles. For the amorphous phase, we can see that there is one extra peak next to the first peak, something that is not obvious for the liquid phase. The liquid phase follows similar pattern to that of the amorphous phase, but without exhibiting the extra peak. This extra peak can be attributed to extra nearest neighbour atoms in the local structure after melting and resolidifying the system that contributes to the extra peak in the histogram for the amorphous phase.

To summarise, I examined the local structure of various small systems by analysing the angle between two pairs of nearest neighbour atoms. For all systems I presented results for the crystalline, amorphous and liquid state and for the case of iron I also presented results for the amorphous and liquid state initially equilibrated as liquid. The point of this analysis was not to quantitatively study the angles between two pairs of bonds but to understand the similarities in the local packing within the various phases.

The figures 28, 29, 30, 31, 32 and 33 present results for the characteristic angles and the cosine of these angles in order to reproduce clearly the formed angles. In these figures we can see similar behaviour for the crystalline, amorphous and liquid phase for most materials. The initial equilibration in liquid state might slightly affect positively the results. This is because the system after melting has less restrictions and the system has more degrees of freedom to reform. The amorphous and liquid state have more degrees of freedom, something that we can see from the broad spectra of angles in the histograms in respect of the crystalline state that the characteristic angles are well defined.

4.3.3 Summary and discussion

In this section I studied the local structure of various materials in their crystalline, amorphous and liquid phase. I examined the local population and the local order in order to make conclusions about the three states and to understand the behaviour of the local structure and the memory mechanism. I analysed the local population by calculating the pair distribution function

and the number of nearest neighbour atoms. Moreover, I analysed the angles that two pairs of nearest neighbour atoms form in order to understand the local order.

The materials I used are small systems of iron, argon, potassium, molybdenum, tantalum and tungsten. I performed MD simulations in order to prepare the structure of each material in three different phases. Specifically for iron I performed two different equilibrations at different temperatures, one equilibration where the system was solid and another one where the system was liquid. After the simulations I analysed all the systems in the same way and I presented similar figures.

I examined the results from MD simulations for the various systems and I validated that the followed procedure does not affect the results. This can be verified from figure 22 where I showed that the memory effects in velocity are being eliminated after short time of simulation. Moreover, the simulations with different equilibration temperature exhibit similar results during the population or structure analysis. The minor differences can be explained due to different preparation of the structure that for the case of the initial equilibration as liquid the sample was melted and re-solidified. Despite the fact, simulations from both different equilibrations show similar qualitative and quantitative results.

After thoroughly studying the results from all previous figures in this section we conclude that specific characteristics for each material, such as the PDF peaks and the characteristic angles for crystals, can be seen clearly in the crystalline phase. For the amorphous and liquid phase these characteristics can still be seen but usually less intensively. The results for the amorphous and liquid states are most of the times very similar and comparable. Moreover we can see that these materials exhibit similar and comparable results in all three phases, even for cases as molybdenum where the crystalline phase does not exhibit a bcc structure as it was expected.

As I proved from MD simulations, the local population and the local order for a material in the amorphous and liquid phases are coherent and similar results can be extracted. Moreover, both these phases exhibit characteristics that can be seen in the crystalline phase. This verifies previous predictions

that refer to memory mechanisms in the short-range structure and that the amorphous and liquid phases maintain local order similar, to some extent, to this of the crystalline phase. This can explain various similarities between the solid and liquid phases as I mentioned in previous sections where I presented results from INS experiments and simulations for the solid and liquid phases and it can justify the comparison between the amorphous and liquid phases.

The previous results prove the connection between the solid and liquid state at short-range distance but they do not explain where this correlation originates from. This is something that I will discuss in chapter 5 where I will explain the origin of the phonon−roton minimum by discussing the interatomic forces of materials. The results from this chapter will help me explain the origin of the phonon−roton minimum by using as study system a crystalline material. Having as a starting point that the local crystalline and liquid structures are highly connected and exhibit very similar features, this model can be extended to liquid systems.

4.4 A model for barium

Earlier in this chapter I made a connection of the solid and liquid phases using as example various materials and I managed to extract similar conclusions for INS experiments and INS simulations. This helps to understand the universality of the methods and the theory I used which do not depend on a specific system but they apply to any system and material. Of course a direct comparison of the same material from experiments and simulations would be desirable.

One method of direct comparison of INS results from experiments and from simulations is the mathematical conversion of the model from simulations in order to represent the barium system. As I discuss in section 2.3 about neutron scattering and the equations 2.21, 2.28 and 2.29 where I define the phonon energy from inelastic neutron scattering, the phonon energy depends on the neutron mass and on the scattering vector. The scattering vector depends inversely to the wavelength, $|\mathbf{k}| = 2\pi/\lambda$, which from Bragg's law depends on the interatomic distance of every material, $\lambda = 2d\sin\theta$. In

this way we can get a rough model for the calculation of the dispersion curves for any material if we know its crystalline order and its interatomic distance and convert results from neutron scattering experiments or simulations of other materials.

Following the steps of the previous model I can estimate roughly the phonon−roton minimum for barium from results from INS simulations of iron. Iron and barium have the same crystalline structure so there is no need to make any other conversion apart from converting the scattering vector by using the lattice constants for these two materials. From the damped harmonic oscillator fitting of iron in section 4.2 I found that the phonon−roton minimum is located at around $\mathbf{Q}_{\mathrm{Fe}} = 2.88$ Å^{-1}. By combing Bragg's law and the wave vector we can convert the scattering vector $\mathbf{Q}$ at every different angle for barium as

$$\mathbf{Q}_{\mathrm{Ba}} = \mathbf{Q}_{\mathrm{Fe}} \frac{\lambda_{\mathrm{Fe}}}{\lambda_{\mathrm{Ba}}} = \mathbf{Q}_{Fe} \frac{d_{Fe}}{d_{\mathrm{Ba}}} \tag{4.14}$$

Thus, by knowing that the lattice constant for iron is 2.87 Å and for barium is 5.02 Å we can calculate the phonon−roton minimum for barium at $\mathbf{Q}_{\mathrm{Ba}}$ = 1.65 Å^{-1}. As we can see this value is very close to the experimental value for barium at $\mathbf{Q}_{\mathrm{Ba}} = 1.66$ Å^{-1} as it was calculated from the DHO fitting. A similar method can be used for the calculation of the phonon frequencies of barium.

This method is good enough method to have good qualitative results but not quantitative results. The experimental data are low resolution data and they include much background noise data. The simulation data have higher resolution and no background noise data but for both experimental and simulation data the phonon frequencies were extracted from collective excitation spectra that includes the averaging of all dispersion curves and they were well fitted to a model. Thus this model can only provide a good understanding of the area of the phonon−roton minimum but we cannot expect to have accurate results.

The most accurate method to compare INS simulations and INS experiments and understand the differences and similarities is to compare results from the same material. Although experiments with barium can be very

expensive and without high resolution results, the experimental procedure is simple. The computational INS simulations of barium are not straightforward as essential parameters are missing from the literature. A model interatomic potential for barium does not exist and classical MD and INS simulations cannot easily be performed.

Although the alkaline earth metals can be considered as simple metals in regard of the electronic aspect, they are certainly the less studied elements among the metals not only experimentally but computationally as well. A search in literature shows that transition metals are the most studied materials while alkali and alkaline earth metals less. Nowadays there are many publications studying computationally various metals either by performing *ab initio* or classical simulations. For barium, the publication list is restricted and people studied barium computationally only by performing *ab initio* simulations but not classical simulations due to the absence of classical interatomic potential describing barium.

It is interesting that for most of the elements of the periodic table there are accurate interatomic potentials describing the motion of atoms but nobody developed a potential for barium. To my knowledge, there is not any publication dedicated to development of interatomic potential for barium, but also publications that include the development of interatomic potential for many similar systems, or groups of materials such as bcc or alkaline earth metals (e.g. [83, 84, 102–105]), barium is never included. That clearly states the need for development of an interatomic potential for this simple element. In the next sections I will explain the method I used to develop an interatomic potential for barium in order to fill the gap in literature and perform classical MD simulations and INS simulations.

4.4.1 Quantum theory

All the previous simulations refer to classical molecular dynamics simulations and interactions between atoms in a system. Quantum simulations provide more accurate calculations than classical simulations and they are suitable for the development of an interatomic potential for use in classical

simulations. I used the CASTEP software [106] to perform quantum simulations in order to get detailed information of the atomic positioning, the interatomic interactions and the system properties, and be able to reproduce parameters for the extended Finnis−Sinclair type interatomic potential for barium. The method I used for fitting the parameters is the force-matching method through the GULP software.

In principle, all information about a system can be obtained by solving the quantum mechanical wave function. This is obtained by solving the Schrodinger equation of the complete many-electron system. However in practice solving such an N-body problem proved to be impossible. For this reason it is necessary to use the density functional theory (DFT) developed by Kohn and Sham [107] based on the theory of Hohenberg and Kohn [108] which in principle is an exact ground state theory. As the name suggests, the fundamental variational parameter is the electron charge density rather than the electronic wavefunctions. In this formalism, the N-electron problem is expressed as N one-electron equations where each electron interacts with all other electrons via an effective exchange-correlation potential. These interactions are then calculated by using the local-density approximation (LDA). Plane wave basis sets and total energy pseudopotential techniques are then used to solve the Kohn−Sham one electron equations. The Hellmann−Feynman theorem can then be used to calculate the forces required to integrate the ionic equations of motion within a molecular dynamics simulation.

The forces of both electrons and ions are of the same order of magnitude and consequently their momenta are comparable. However since the ions are so massive in comparison to the electrons, the kinetic energy of the ions is much smaller than those of the electrons. This idea forms the basis of the Born−Oppenheimer approximation. The electrons are assumed to respond instantaneously to the motion of the ions. For any ionic configuration in the system, we assume that the electrons are in the instantaneous ground-state and calculate the total energy of the system. Varying the ionic positions defines a multi-dimensional ground-state potential energy surface, and the motion of the ions can then be treated as classical particles moving in this

potential.

Hohenberg and Kohn [108] proved that the total energy of a system including that of the many-body effects of electrons, the exchange and correlation energy, in the presence of static external potential is a unique functional of the charge density. The minimum value of the total energy functional is the ground state energy of the system. The electronic charge density which yields this minimum is then the exact single particle ground state energy. It was then shown by Kohn and Sham [107] that it is possible to replace the many electron problem by an exactly equivalent set of self consistent one electron equations.

In the Kohn−Sham DFT, the intractable many-body problem of interacting electrons in a static external potential is reduced to an easier problem of non-interacting electrons moving in an effective potential. The effective potential includes the external potential and the effect of the Coulomb interactions between the electrons, such as the exchange and correlation interactions, something that is difficult to calculate. The simplest approximation for solving this problem is the LDA, which is based on the exact exchange and correlation energy for a uniform electron gas. Non-interacting systems are relatively easy to solve as the wavefunction can be represented as a Slater determinant of orbitals. A Slater determinant is an expression that describes the wavefunction of a multi-fermionic system that satisfies anti-symmetry requirements and consequently the Pauli principle by changing sign upon exchange of two electrons (or other fermions). Furthermore, the kinetic energy functional of such a system is known exactly. The exchange-correlation part of the total-energy functional remains unknown and must be approximated.

In physics the most widely used approximation is the LDA, where the functional depends only on the density at the coordinate where the functional is evaluated. Another approximation is the generalized gradient approximation (GGA). The GGA is local, as the LDA, but also take into account the gradient of the density at the same coordinate. It gives very good results for molecular geometries and ground-state energies reducing LDA approximation errors by a factor of 5 [109].

The handling of infinite number of interacting electrons moving in the

static field of an infinite number of ions includes two main difficulties. A wavefunction has to be calculated for each of the infinite number of electrons which will extend over the entire space of the solid and the basis set in which the wavefunction will be expressed will be infinite. As we know the ions in a perfect crystal follow a periodic arrangement. Therefore the external potential related to the electrons will also be periodic. With the use of Bloch's theorem, it is possible to express the wavefunction of the infinite crystal in terms of wavefunctions at reciprocal space vectors of a Bravais lattice. The Bloch's theorem uses the periodicity of a crystal to reduce the infinite number of one-electron wavefunctions to be calculated simply by the number of electrons in the unit cell of the crystal. By using Bloch's theorem, the problem of the infinite number of electrons is now mapped onto the problem of expressing the wavefunction in terms of an infinite number of reciprocal space vectors within the first Brillouin zone of the periodic cell, at $-\mathbf{k}$ to $+\mathbf{k}$ This problem is dealt with by sampling the Brillouin zone at special sets of $\mathbf{k}$-points.

With the use of Bloch's theorem a plane wave energy cut-off in the Fourier expansion of the wavefunction and careful $\mathbf{k}$-point sampling the solution to the Kohn−Sham equations for infinite crystalline systems is faster. Nevertheless a plane wave basis set is usually very poorly suited to expanding the electronic wavefunctions because a very large number of $\mathbf{k}$-points is required to accurately describe the rapidly oscillating wavefunctions of electrons in the core region.

It is known that most physical properties of solids are dependent on the valence electrons to a much greater degree than that of the tightly bound core electrons. It is for this reason that the pseudopotential approximation is introduced. This approximation provides a simplified solution that uses this fact to remove the core electrons and the strong nuclear potential and replace them with a weaker pseudopotential which acts on a set of pseudo wavefunctions rather than the true valence wavefunctions. In fact, the pseudopotential can be optimised so that in practice it is even weaker than the frozen core potential [110].

DFT is an accurate method for performing calculations with results that

can be compared with experimental results. Although there are various approximations, the DFT MD is often more precise than classical MD, although the small system size that is being used in DFT MD is an important drawback of this method. The DFT calculations start with an initial random charge density and then solve the equation of the pseudopotential and the Kohn−Sham equation during various iterations in order to calculate the new realistic density and then calculate the new forces and energies of the atoms. As I will explain in the next section I preform DFT calculations in order to achieve highly accurate results for the calculation of the parameters of the interatomic potential for barium. I will describe the procedure of obtaining these parameters and I will discuss the fitting method and the calculated results.

4.4.2 DFT simulations

To obtain information about the atomic positioning, forces and energies for barium in order to calculate the parameters for the interatomic potential I preformed DFT calculations. As I explained earlier DFT calculations provide accurate results but they are highly computational demanding and only small systems, of the order of hundreds of atoms, are allowed to be studied. Especially for the case of DFT MD simulations the need of HPC computing is needed. For all the *ab initio* calculations I report in this section I used the CASTEP software which follows the previously discussed theory of DFT calculations.

In order to prepare the interatomic potential parameters to describe barium in both solid and liquid phase I initially used a liquid structure to obtain the fitting data. A crystalline structure would fail to provide data for randomly allocated atoms as in amorphous and liquid systems, resulting a state-depended potential. The preparation of the system in the liquid state can be done in two ways. The straightforward method is to perform a long DFT MD simulation in order to equilibrate the system and then another DFT MD simulation to obtain the fitting data. The method I used is to choose a material with similar structural properties as barium, then perform classical

MD simulation in order to prepare the molten system and then convert the results to represent barium.

The first method requires to perform a MD simulation under NPT ensemble to equilibrate the system and then perform a MD simulation under NVE conditions in order to melt the system at high temperature. Both simulations would require many time-steps in order to eliminate any correlation effects. This method, despite the small system of 128 Ba atoms, requires exceptionally high computational demand. In the method I used, the material I chose is bcc iron consisted of 128 atoms. I performed classical MD simulations in order to equilibrate the system and then melt it and get a liquid configuration, in similar way as I explained earlier in this chapter. I initially converted this molten configuration by using as a scaling factor iron's and barium's density in their bcc phases, in order to alternate the size of the system and then I replaced all the iron atoms with barium atoms.

At first instance this method is valid since the simulations I performed are under constant volume so the system size remains constant and moreover the atoms in the system remain the same. In this way the density of the crystalline phase is the same as in the melted phase. Moreover, in a melted system the atoms are randomly allocated in the configuration, losing any correlation with the initial system, so the replacement of the atoms will not affect the results. This method is much faster since it involves only classical MD simulations of a very small system of 128 atoms.

For the scaled system I performed geometry optimisation (GO) in order to equilibrate the system and then I performed MD simulations in order to obtain all the necessary data. During the GO procedure I tested the system with various different pseudopotentials, functionals, cut-off and accuracy parameters in order to choose the combination that reproduces accurately the physical properties of barium. Most of the used parameters for the DFT calculations are the CASTEP 6.01 version default parameters. The pseudopotential I used can be found in literature [111] and it is based on the PBE functional [112]. The GO optimisation was performed by using the BFGS minimisation.

I performed the MD simulations by using periodic boundary conditions

at zero temperature under NPT ensemble, using the Andersen−Hoover barostat algorithm [91, 113] and the Nosé−Hoover thermostat algorithm [90, 91] for a total of 10 ps of simulation time. I focused on the high precision of calculations using accuracy of about 0.1 eV per atom. For barium, which is metallic system the Fermi surface smearing scheme I used is the Gaussian smearing scheme with smearing width 100 K and 50 % extra bands in addition to the number of occupied bands.

The electronic structure of a periodic crystal is represented by the band structure. In DFT calculations metals are systems with unoccupied states very close to the Fermi level, so there are partially filled bands. For this reason a large number of **k**-points is necessary. Metals have bands very close in energy to the valence band, so the energy minimisation will take a long time to remove them from the trial wavefunction and by including higher, unoccupied bands we can improve the convergence. In order to improve the convergence with a large number of **k**-points the step function is replaced with a smearing function.

In the next section I describe how to treat the data from the DFT MD simulations in order to obtain results for the interatomic potential parameters for barium. These parameters correspond to the extended Finnis−Sinclair potential [84] which is a type of EAM potential. The Finnis−Sinclair potential and the extended Finnis−Sinclair potential were initially developed for bcc metallic materials as barium and they describe them more accurately than other potentials, as the pair potentials. The fitting method I chose to fit the DFT data is the force-matching method [114].

4.4.3 Force-Matching method

It is known that classical pair potentials fail to describe metals or semiconductor materials and there is need for more sophisticated potentials such as the EAM potential. The basic reason is that in a pair (two-body) potential the strength of each bond is by definition dependent only on the distance between the two atoms involved and the positions of all the other atoms are not relevant. In practice, however, the strength of the bond between two

atoms is affected by the environment as determined by the other atoms in the proximity. If a molecule has more atoms, the bond strength will generally decrease as a result of Pauli repulsion between electrons, so there is need for the potential to be environment dependent and adapt to different conditions. The EAM potential involves density dependent terms, such as angular forces or moment expansions and it can adapt to different conditions providing a realistic description of the system. A typical EAM potential is thus constituted by a number of functions combined in a complex way, and often nested one into another.

For each material the analytical expressions have to be fitted differently by using experimental data. Of course the experimental data are measured at specific conditions and a potential fitted to these data will behave better to these specific conditions. The force-matching method is a fitting procedure capable of dealing with the complexity of multifunction potentials and exploit effectively their modelling power by making use of very large amounts of information obtained by *ab initio* calculations such as DFT calculations. This method is based on trying to match as closely as possible the first principles forces with those obtained from the potential. The optimisation is performed by carrying out a minimisation in a relatively large parameter space.

This method is nowadays a well established method for fitting data for interatomic potentials. There are many publications in literature using the force-matching method in a variety of fields, with very good results (few examples are: Al [114, 115], Mg [116], Si [117], Ni [115], Cu [118], SiO_2 [119], Fe [120], Ta [121], H_2O and CH_4 [122], Au [123], Cu-Zr and CuZr-Al [124], 14 fcc metals [125], biomolecules [126]). As I discussed earlier this method focuses on metal potentials and it is expected to behave well for the barium case. However, obtaining accurate and realistic interatomic potentials constitutes a very challenging task.

For the barium case, the system consists of 128 atoms in liquid formation and data were taken from DFT MD simulation of total 10 ps. The fitted data are interatomic positions and forces for every atom and the system's energy and stress values. In order to include different geometries and increase the potential's transferability I included data of configurations from the DFT

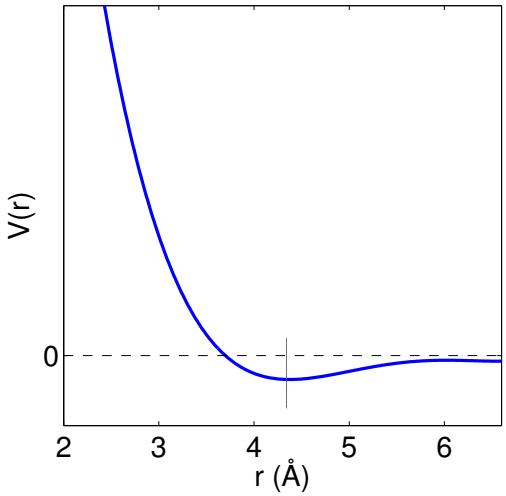

Figure 34: Qualitative representation of extended Finnis−Sinclair potential for barium.

MD simulations every 200 steps, which corresponds to atomic movement of 0.2 ps.

In the beginning of this chapter I defined the extended Finnis−Sinclair potential. The fitting parameters include five coefficients of the fifth order polynomial fitting equation, two cut-off parameters, a parameter for the functional and a parameter for the electron density function. The two cut-off parameters are the only two parameters with physical meaning and they lie in a distance between the second and third neighbour atoms in a system. Yet, examples in the original extended Finnis−Sinclair publication show that the two parameters are not the same and for some materials the one parameter is higher than the other while for other materials is the opposite. So, although an approximate value can be used as initial value the two cut-offs need to be fitted.

In figure 34 I present a plot of the extended Finnis−Sinclair potential that represents qualitatively barium. The plot, described from the equation 4.7, represents the potential as a function of distance. For very small distances the value of the potential tends to infinity, something that is normal since the repulsion of the atoms when they are getting closer is getting higher.

Then the curve forms a minimum point (well's minimum). It is known from theory, that the minimum point defines the nearest neighbour interaction, where the highest attraction can be found. At larger distances the potential tends to zero and follows asymptotically the horizontal axis till infinite.

The range of polynomial parameters I used, expands from very large negative values to very large positive values with random incrementation. Similarly I treated the functional and density parameters, while for the two cut-offs the variation of the values was smaller. I tested numerous sets of parameters following various patterns of increasing or decreasing the values accordingly, or following random patterns and using arbitrary numbers. Since I use realistic data from *ab initio* simulations the set of fitted parameters should be able to adjust to the data without any manipulation and describe the system realistically. All the fits were performed under constant pressure.

The fitting software I used is the GULP version 4.2 [95]. By default GULP uses a Newton-Raphson functional minimisation approach. The quality of the fit can be understood by the sum of squares which measures how good the fit is. The sum of squares is defined as the sum of the squared difference of the calculated value minus the observable value multiplied by a weighing factor. Ideally this should be zero at the end of a fit but in practice this will only happen for trivial cases where the potentials can be guaranteed to completely reproduce the data. As it is known there is no unique fit as there are infinite possible fits depending on the choice of the weighting factors. The choice of weighting factor for each observable depends on several factors such as the relative magnitude of the quantities and the reliability of the data.

The fitting process consists of various test cases. The parameters that varied are the number of configurations I used as input data, the weight of the interatomic forces, the energy and stress values of the system and the values of the potential parameters. Although the weighting was higher usually for the values of the stress of the system, I alternated the weight between the input values in order to obtain accurate data without underestimating the rest of the fitted variables. For the potential parameters (I presented the extended Finnis−Sinclair potential in equation 4.7 and its following paragraphs) I used arbitrarily values, most of them similar to the values of other bcc materials

described in the original extended Finnis−Sinclair publication [84]. As cut-off parameters I used various values, with most of them to lie in a distance between the second and third neighbour atoms. The rest of the parameters do not correspond to any physical value but only to a fifth order polynomial equation with dependencies on the cut-off distances, the density equation and the functional, so there is no restriction or guidance of what value they should have.

Further to the fitting process I performed various independent evaluation processes. A first indication, as mentioned above, is the value of the sum of squares where the smaller the value the better the fit. Moreover a visualisation in a plot of the initial and the calculated values of the the fitted data provides a fast evaluation of the quality of the fit. Furthermore I performed single cell geometry optimisation by using the already fitted parameters. I did this in order to get a good indication of how the fitted parameters treat the crystal cell and if they reproduce accurately the crystal lattice, the elastic constants, known from literature [56, 58, 127], and the phonon frequencies. Additionally, for some sets of parameters I performed a self-consistent evaluation in which I fit the parameters by using only half of the input configurations and then I use the fitted parameters with the second half of input configurations to understand the consistency of the results. Finally, I chose some sets of parameters in order to perform classical MD simulations and test how they treat the motion and the properties of the system.

For various testing cases and different parameters I got good results in different properties. For the sum of squares, the weight of the variables highly affects the minimum value. Even when the minimum value tends to zero the system does not necessarily exhibit the best fitting but the closer to the best fitting of the highest weighted values. As it was often the case during the fitting procedure, high weighting in the forces results to good force fitting but bad or intermediate energy and stress fitting, and *vice versa*, showing that there is a clear contradiction between these sets of values. In any of these cases, or even in cases of intermediate fitting of all values, the results that represent the physical properties were calculated with large error factor, regarding theoretical or experimental values.

The main physical properties, known from literature, that I used as evaluation for my fit is the crystalline lattice constant, the elastic constants and the phonon dispersion curves. During the single cell geometry optimisation process, by using different potential parameters and cut-offs the crystal cell volume indeed reached the theoretical value having at the same time good results for the phonon dispersion curves. Thus, the elastic constants were the most difficult reproducible physical property with very high error during the calculations, even if the elastic constants were highly weighted.

During the self-consistent evaluation various potential parameters were used. The output fitted parameters from the first set of configurations were used to fit the second set of configurations. Some sets of the fitted parameters were reproduced during the fitting with the second set of configurations. This shows that the method I am using is consistent and mathematically correct. Still, the physical properties calculated from both sets of data exhibit high inaccuracy.

I used some of the sets of parameters with good fit of the initial and final data, which were also able to reproduce closer the physical properties of barium, to perform classical MD simulations. These parameters were used for the simulation of both small and large systems, following the same process as with all the previously described classical MD simulations. Among other configurations I used the initial configuration of 128 atoms of iron that I used for the preparation of the DFT MD simulations. Results from the MD simulations showed either high expansion or high contraction of the system during the equilibration process, or unphysical representation of the interatomic forces, not being able to describe the motion of the system. These phenomena are known to appear during simulations with bad interatomic potentials.

The sets of parameters that reproduce accurately a physical property, as the crystal lattice constant or the elastic constants, largely vary in a way that there is no pattern to be followed and lead to an optimisation of the parameters. As I explained earlier these parameters have no physical meaning and if the fitting procedure fail then they cannot be adjusted manually in a logical way. Therefore none of the sets of parameters I used describe

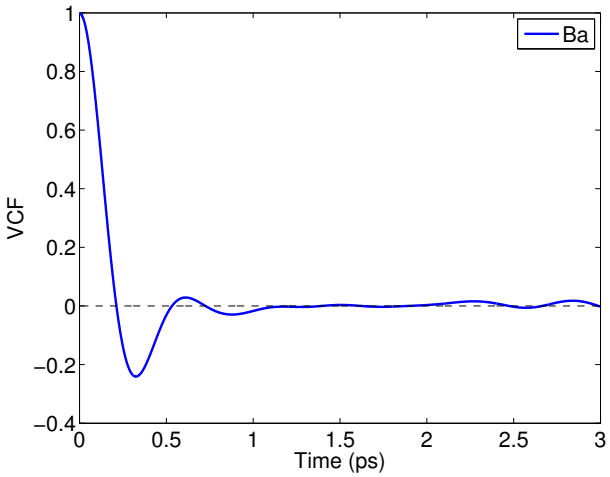

Figure 35: Velocity correlation function (VCF) for Ba in amorphous phase.

accurately all three physical properties of barium, lattice constant, elastic constant and phonon dispersion curves. As a result of the fitting procedure, potential parameters of extended Finnis−Sinclair type for barium could not be extracted.

4.4.4 Local structure analysis

Results from the DFT MD simulation are characterised by high accuracy, similar to experimental values and can be used for further analysis. Similarly to the analysis of results from classical MD simulations which I described earlier, I performed population and bond analysis. The systems consists of 128 barium atoms in amorphous configuration.

In figure 35 I present the velocity correlation function for barium from results from 10 ps of MD simulations. Similarly to figure 22 for iron, the VCF for barium starts with a maximum value for the initial configuration and it follows a damped oscillation till it goes to zero after many simulation steps. As we can see any correlation to the initial structure is lost after about 1 ps of simulation time. The results from this figure are comparable to those of figure 22 for iron initially equilibrated at 10 K, but the pattern of the correlation is similar to results of figure 22 for iron initially equilibrated at

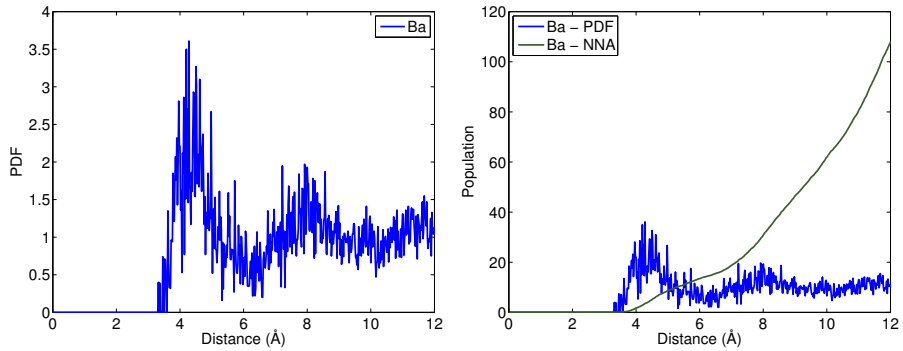

Figure 36: Population analysis for a system of 128 atoms of Ba in amorphous phase. The left plot shows the pair distribution function (PDF) and the right plot shows the PDF multiplied by a factor of 10 and the nearest neighbour atoms (NNA) curve.

4,000 K. That can be explained from the fact that the initial structure was already melted and there is no periodicity in the system. The fact that the correlation remains for longer time, comparable to this of crystal structures, can be attributed to the higher amount of statistics involved during the DFT MD simulations than during the classical MD simulations.

In figure 36 I present results from population analysis of the study system. In the left plot I present results of the PDF. As we can see, the system exhibits a characteristic pattern of amorphous, or liquid, phase with broad and not well defined peaks which at large distances tends to 1. In the right plot of this figure, I present the results of the PDF multiplied by a factor of 10 in order to be visually comparable with the NNA curve. The NNA curve for barium does not exhibit well defined plateaus but it is clear that at the points where the curve changes slope in the areas of the first and second peaks, the NNA curve has values of around 8 and 14, which are characteristic values of the bcc phase.

In figure 37 I present results for the bonds between two nearest neighbour atoms in the amorphous barium system. The description and analysis of this figure is similar to that of the previous figures 28, 29, 30, 31, 32 and 33. The three rows of histograms present the angle analysis for the same system at three different simulations times, at 0 ps which is the initial configuration,

at 5 ps and at 10 ps.

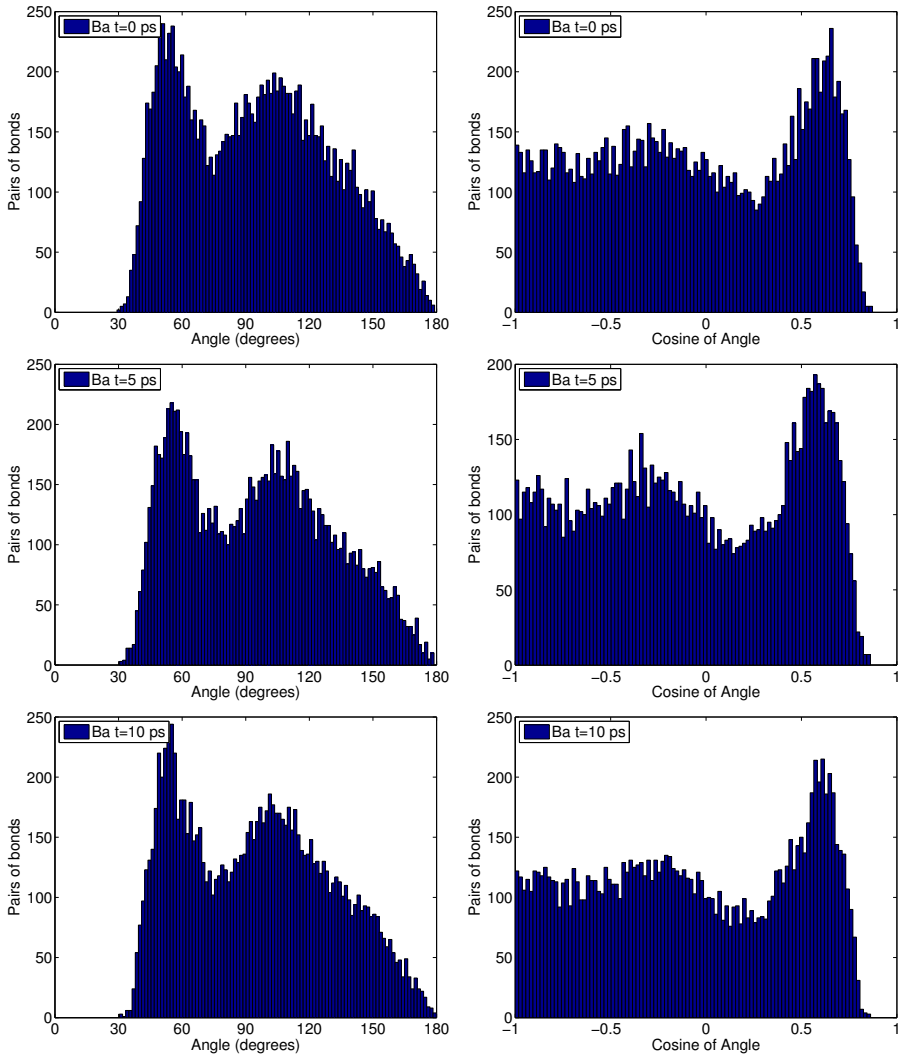

Figure 37: Characteristic angles between pairs of nearest Ba atoms in the amorphous phase. The left histograms present the angles between pairs of bonds in the system and the right histograms present the value of the cosine of these angles. The histograms present results from configuration of the DFT MD simulation at 0 ps, 5 ps and 10 ps.

As we can understand better from the cosine of angle histograms in figure 37, the amorphous phase exhibits three main angles, at around 55°, 110° and 180° (roughly cosine of 0.6, −0.4 and −1 respectively). That means that

the amorphous barium exhibits angles similar only to the two characteristic angles for bcc systems, while there is a declination for the angle of 70.53°. Although the analysis is the same as in section 4.3.2, the expected angle disagrees with the resulted angle. Moreover, this declination is exhibited during the whole simulation showing a consistency regardless of the simulation time.

4.4.5 Summary and discussion

In this section I discussed a simple way to convert existed INS data to represent barium, how to perform quantum simulations of barium, the fitting process for fitting the parameters for its interatomic potential and its local structure analysis. The model for converting INS data is a very simple model, good only for qualitative comparison of INS spectra. This model uses as a conversion factor the lattice constant of every element in order to visualise INS spectra for other materials. Due to the high similarity of the dispersion curves of iron and barium, as I explained in the beginning of the chapter, the model is expected to work fairly well, but still it should be used only as a guide for the expected results.

For more accurate results I performed molecular dynamics simulation using the density functional theory. During the quantum calculations I tested various parameters and I performed geometry optimisation in order to obtain high quality results during the MD simulation. The MD simulation lasted for 10 ps, time long enough for the system to lose any memory effects as I show in figure 35. From the MD simulation I obtained high accuracy results for the system, such as atomic positioning, interatomic forces and the system's energy and mechanical properties. I used these data in order to obtain parameters for the interatomic potential for barium.

The fitted interatomic potential is of the form of extended Finnis−Sinclair potential. This potential has 9 parameters to be fitted, including 2 cut-offs with physical meaning, while the rest parameters describe the model and have only mathematical meaning. As I discussed I examined a large range of values for these parameters and different weighting factors during the fitting process. The evaluation of the fitting was done in various ways using

as main judging factor the good reproduction of the physical properties of barium, something that was achieved to some extend but without getting the desirable results.

This problem might be explained by the local structure analysis. Although the NNA analysis exhibits results characteristic to the bcc structure the angle analysis does not exhibit the expected results. As I presented in the previous section, amorphous and liquid materials hold a structure similar to this of the corresponding material's crystalline structure. In the angle analysis of barium from the DFT MD simulation showed that the local structure exhibits two out of three characteristic angles of a bcc material, something that remains for the whole MD simulation.

The origin of this problem is not easy to be identified. During the fitting process, the fitting parameters describe the extended Finnis−Sinclair potential, a potential which is proved to describe well atomic motion and system properties in other similar systems. Something that might concern the whole procedure is the small system size. Still, in literature there are potential fitting examples with most systems to vary from 64 to 256 atoms. Something that might be worth noting is that all the tested with extended Finnis−Sinclair potential materials have smaller lattice constant than barium.

Apart from the system size and the potential, a possible origin of the variation in the exhibited angles, might arise from the procedure before the MD simulation. An initial error during the geometry optimisation of the system would be vanished after a long MD simulation, since the atoms vibrate for long enough time to be allocated accordingly as their motion and their interactions described by the pseudopotential. If the pseudopotential is faulty then it would not provide good results during the geometry optimisation procedure. Still a combination of tolerance in inaccuracy of the results and a not high quality pseudopotential might affect the system during the geometry optimisation procedure without being noticed.

The initial target of producing high quality parameters for an interatomic potential that describes barium was not achieved. Despite the numerous fitted potential parameter sets and the high accuracy of the calculations, the

potential parameters did not manage to describe precisely barium's physical properties. Thus classical MD simulations and calculation of the INS spectra for barium cannot be performed.

In the next chapter I will provide a theoretical explanation of the interatomic interactions in a bcc system and I will describe the origin of phonon−roton minimum that can be seen in the acoustic modes. By using the results extracted from this chapter I can reasonably extend the theory from crystalline systems to liquid systems. This theoretical explanation will be compared with the presented results from INS experiments and simulations, for both the solid and liquid phase.

5 The origin of phonon−roton minimum

In chapters 3 and 4 I presented results from inelastic neutron scattering and I emphasise at the small and intermediate wave vector regime. This regime corresponds to the initial linear increase and the first minimum of the acoustic phonon dispersion curves, known as phonon−roton minimum. The phonon−roton minimum is the area of phonons with specific energy and in collective excitation spectra is located in between the two areas where phonons have maximum energy, also known as maxons. This minimum describes the reduced energy ω of phonons at specific wave vector. The phonon−roton minimum can be seen clearly in collective excitation spectra for solids and liquids, something that contradicts the initial theory about roton minimum.

The roton minimum was initially introduced by Landau [2] in order to describe the elementary excitations in superfluid ^{4}He. The theory of superfluidity played an important role in the explanation of the behaviour of the superfluid phase of ^{4}He. A superfluid is a liquid in motion without friction resulting in a non-viscous flow. This can happen in liquids below the critical temperature (T_c). For velocity of motion above a specific maximum velocity, the critical flow velocity, the superfluid behaviour is not explained. Landau, in order to explain the superfluid behaviour, suggested that the phonon excitation should not be monotonic but it starts with a longitudinal phonon branch with linear increase, then reaches a maximum and then forms a deep minimum. At this minimum the phonon energy is equal to the wave vector times the critical flow velocity.

The roton minimum was initially identified in superfluid helium by Feynman in 1954 [3] while a few years later Feynman and Cohen [128] used a trial wave function to describe the elementary excitations spectrum. This wave function suggests that the roton is a kind of quantum-mechanical analog of a microscopic vortex ring, of diameter about equal to the atomic spacing. Later on more scientists studied the superfluid liquid helium in order to accurately define the minimum at $\mathbf{Q} = 1.93$Å [129–132]. Feynman, following Landau's initial theory, discussed the origin of roton minimum and he con-

cluded that the roton minimum is related to local vorticity. The vorticity enters ^{4}He by quantised vortex lines or by quantum vortex rings. A quantum vortex is a topological defect, which in superfluids is a hole with the superfluid circulating around the vortex axis. The inside of the vortex contains excited particles, the rotons. As it is known nowadays, this model gives only qualitative agreement with the experiments.

Apart from the quantum vortices other theories aimed at understanding the nature of the roton excitation. In 1990, by making use of the microscopic theory, Glyde and Griffin related rotons with the existence of a Bose condensate [133]. This is related to Landau's idea that the sound wave and other excitations could equilibrate with one another and flow separately from the rest, something known as the Bose condensate.

Glyde and Griffin presented the roton as a renormalised single-particle excitation (as initially presented by Miller, Pines, and Nozières in 1962 [134] and Burke, Major and Chester in 1967 [135]) mixed with the density fluctuation spectrum for $T < T_\lambda$, where T_λ is the superfluid transition temperature. Therefore one might expect distinct changes in the excitation spectrum on passing through T_λ. Furthermore, these changes are expected to be such that they signal the appearance of a new excitation in the fluid when one enters the superfluid phase. The different temperature behaviour of the neutron scattering in the phonon and in the roton region has motivated Glyde and Griffin to propose that the phonon−maxon−roton excitation curve arises from two quite distinct processes, a zero sound mode at small scattering vector and a single particle mode beyond the maxon scattering vector. The suggested model by Glyde and Griffin has been used extensively to analyse neutron scattering results for liquid ^{4}He [132, 136, 137], but there are cases with qualitative disagreement with this model [138].

Two interesting theories on the origin of roton minimum and the physical mechanism of its formation was pointed out by Schneider and Enz in 1971 [139] and Celli and Ruvalds in 1972 [140]. In reference [139], the authors refer to roton as a soft mode which leads to the dynamic instability. Several years later this minimum is referred as a soft mode which is responsible for creating new phase for calcite [141]. In reference [140], the authors

mention that the roton minimum is not characteristic of ^{4}He only but it is observed in other non-superfluid materials as well, during the liquid-solid phase transition, making clear that any theory on rotons should apply to phonons and maxons as well. Based on the conclusions of the previous two publications, Galli, Cecchetti and Reatto in 1996 [142] and later Nozières in 2004 [143] stated that the origin of the roton minimum arises from the strong correlations dominating in the system and that the roton is not behaving exactly as a single particle excitation. Interestingly enough, Nozières discusses superfluid ^{4}He and the roton minimum by starting from the solid phase rather than the dilute gas as before.

In reference [142] the authors refer to the absence of identification of the role of interference between different particles which modifies the properties of the collective excitation along the wave vector. They performed calculations based only in the law of interatomic interaction and they explain roton as similar to a single particle excitation but for wave vector larger than the roton minimum regime where the excitation is quite distinct from a single particle excitation due to interference effects between atoms. Furthermore, they assert that at the roton minimum there is a simple dipolar flow of the local momentum of atoms due to backflow, similar to a small vortex ring.

Following Nozières' ideas, Kalman *et al.* in 2010 [144] studied the roton minimum and strong correlations in classical systems. They performed classical MD simulations of the dynamics of a classical system in order to represent its dispersion curves, focusing on the longitudinal phonon dispersion curve, and compared them with results from quantum simulations. Their results showed that there is no major difference in the dispersion curves from quantum and classical systems and they refer to roton minimum as a classical phenomenon. They argue that dispersion curves that have been explained through strong correlations in a classical system cannot be described by vortices or single-particle excitation. Their explanation is that the roton minimum is a classical process and its origin is due to strong interatomic interactions. Based on this and on results of collective excitation spectra that exhibit the roton minimum, from various publications and for various materials from the literature (I presented examples of simple solids and liq-

uids that form the phonon−roton minimum in section 3.3) they discuss a universal effect not restricted to ^{4}He.

Although Kalman *et al.* were the first to comment about the universality of the phonon−roton minimum across many materials, before them Tozzini and Tosi in 1999 [137] studied the phonon dispersion curves for crystalline helium and commented about the good extent phonons and rotons of the superfluid ^{4}He reflect the longitudinal and transverse phonons in the corresponding crystal. From Tozzini's and Tosi's results, as well as from results from references in their paper (*e.g.* [145]), on solid and liquid helium we can see the existence of roton minimum in both solid and liquid phases of helium. The summary of Kalman *et al.* and Tozzini and Tosi comments is that the roton minimum, or more general the phonon−roton minimum, is a classical phenomenon. It exists for both crystalline and liquid phase of a material and not just for liquid helium or superfluid materials but for a wide variety of strongly coupled materials.

5.1 Dispersion curves

Following the conclusion of the previous section I will describe how the interatomic interactions affect the formation of the phonon−roton minimum. To explain the interatomic interactions I will initially simplify the problem by describing an 1-dimensional monatomic system in linear formation. Later I will extend the problem to a 3-dimensional lattice with bcc structure in order to describe the interatomic forces along the longitudinal acoustic mode.

The simplest way to describe interatomic interactions is by using the linear chain model. In this model all the atoms N with mass m are allocated in a linear formation separated by distance a, which also defines the unit cell length. If we assume that we have a harmonic system and every atom interacts only with its closest neighbours, then the energy that describes the system is

$$E = NE_{\text{bond}} + \frac{1}{2}J\sum_{n=1}^{N}(u_n - u_{n+1})^2 \tag{5.1}$$

where E_{bond} is the energy between two neighbour atoms, u_n is the displace-

ment of the n-th atom from its equilibrium position and J is the force constant at the equilibrium position and it is defined as

$$J = \left.\frac{\partial^2 E}{\partial u^2}\right|_{u=0} \tag{5.2}$$

If we focus on the acoustic mode, the dispersion curve at small wave vector forms a linear line. The dependence of the angular frequency on the wave vector $\mathbf{k}$, at small wave vector, is given as

$$\omega = v_{\text{sound}} k = \left(a\sqrt{\frac{J}{m}}\right) k \tag{5.3}$$

The equation 5.3 connects the angular frequency with the unit cell length and the force constant J which is defined by the second derivative of the energy of the system. I extrapolate equation 5.3 in details in appendix A.

If we extend the theory to larger wave vectors, the energy of an atom n is given as

$$E_n = \frac{1}{2}J(u_{n+1} - u_n)^2 + \frac{1}{2}J(u_n - u_{n-1})^2 \tag{5.4}$$

and the angular frequency as function of the wave vector which describes the dispersion curve of the atom n, is

$$\omega_k = \sqrt{\frac{4J}{m}}\left|\sin\left(\frac{ka}{2}\right)\right| \tag{5.5}$$

When $\mathbf{k}$ tends to zero the equation 5.5 transforms to equation 5.3. In order to include more interactions than just the nearest neighbour interaction and describe the dispersion curve of all atoms in the system we can use the equation of energy that describes the whole (linear) system

$$E = N\sum_p \phi_p(r_p) + \frac{1}{2}\sum_{n,p} J_p(u_n - u_{n+p})^2 \tag{5.6}$$

where $\phi_p(r_p)$ is the energy between the n-th atom and its p-th neighbour,

which are in a distance $r_p = pa$. The force constant J_p is defined as

$$J_p = \frac{\partial^2 \phi_p}{\partial r_p^2} \tag{5.7}$$

Consequently, the angular frequency (or dispersion curve) of the system as function of wave vector is defined as

$$\omega_k = \sqrt{\sum_p \frac{4}{m} J_p \sin^2\left(\frac{kpa}{2}\right)} \tag{5.8}$$

Both equations 5.5 and 5.8 are derived in details in appendix B. All the previous equations refer to the linear chain model and for interaction between two nearest atoms, or as proved in equation 5.8 interactions between more atoms, in a system with the same type of atoms.

Now that I defined the angular frequency for a monatomic linear system I will try to explain the forces constant and the dispersion curves for a 3-dimensional system. For simplicity I will discuss only the bcc case but similar results can be extracted for other symmetries such as the fcc or more complicated formations. As I did for the linear system, similarly for the 3-dimensional system I will discuss a monatomic system. A system with more than one atoms in three dimensions is possible to be described but it requires a complicated solution.

As we know from theory, there are two orthogonal directions perpendicular to the wave vector, so there are two transverse acoustic modes and only one direction parallel to the wave vector, so there is one longitudinal acoustic mode. Using as a typical example for a bcc material figure 19 in section 4.2.1 which describes the dispersion curves of bcc iron, we can see that along the [1 0 0] direction we can see only one TA and one LA. The two TA are degenerate due to the high symmetry of the system along the [1 0 0] direction. Moreover for this direction the LA and the TA have very similar frequencies.

To explain why along the [1 0 0] direction the two TA are degenerate and why the TA and the LA have very similar frequencies, I will try to explain the interatomic interactions between planes. The atomic force constant (K)

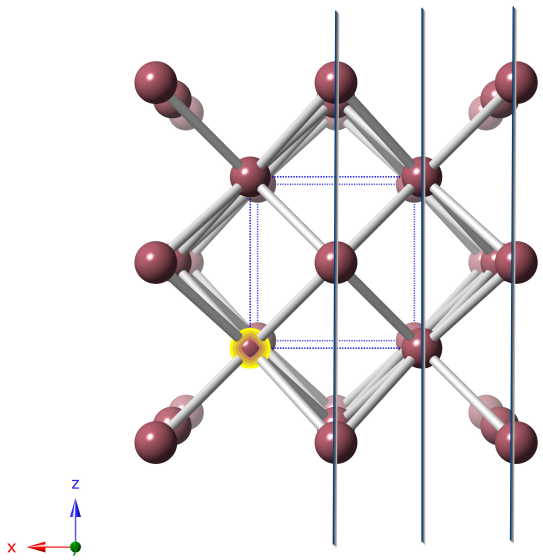

Figure 38: A bcc crystal at [1 0 0] direction parallel to the paper.

acts along the direction of the distance between atoms and is defined as

$$K = \frac{\partial^2 \phi}{\partial r^2} \tag{5.9}$$

where ϕ is the interatomic energy and r is the interatomic distance. In order to calculate the force constants for the displacement along x, y, z axis we need to sum over all interatomic interactions between their planes, so we need to have knowledge of the atomic positioning in the 3D space. The (1 0 0) plane and the first parallel plane include four nearest neighbour atoms with vectors $\mathbf{a}(1/2, 1/2, 1/2)$, $\mathbf{a}(1/2, 1/2, -1/2)$, $\mathbf{a}(1/2, -1/2, 1/2)$ and $\mathbf{a}(1/2, -1/2, -1/2)$. With the use of equation 5.7 for the interatomic vector $\mathbf{r}$ = (x, y, z) we can define the interatomic force constants along the x, y, z axis over all interactions for one atom and it nearest neighbours along the (1

0 0) plane as

$$J_{\mathrm{x1}}^{[100]} = \sum_j \frac{\partial^2\phi}{\partial x_j^2} = \sum \frac{x_j^2\partial^2\phi}{r^2\partial r^2} = \frac{4}{3}K \ ,$$
$$J_{\mathrm{y1}}^{[100]} = \sum_j \frac{\partial^2\phi}{\partial y_j^2} = \sum \frac{y_j^2\partial^2\phi}{r^2\partial r^2} = \frac{4}{3}K \ , \qquad (5.10)$$
$$J_{\mathrm{z1}}^{[100]} = \sum_j \frac{\partial^2\phi}{\partial z_j^2} = \sum \frac{z_j^2\partial^2\phi}{r^2\partial r^2} = \frac{4}{3}K$$

Arbitrarily I define as J_{x} the force constant for the longitudinal mode and J_{y} and J_{z} the force constants for the two transverse modes. The number 1 in the subscript denotes the first neighbour interactions. K is the atomic force constant for the nearest neighbour atoms interactions. Hence we can understand why the two transverse dispersion curves are degenerate. Still in figure 19 we can see that the TA and LA have very similar frequencies but not the same and from the calculations in equation 5.10 the force constants for the TA and LA are the same. The minor difference between the TA and LA is because of the second nearest neighbour interatomic interactions that involves the distance of one unit cell length a and it only contributes to J_{x}, hence it only affects the LA.

Realistically, for the calculation of the dispersion curves for the whole system we need to consider interactions for distances larger than only the first nearest neighbour distance. If we take into account distances up to second neighbour distances, which is the length of one unit cell parameter a, we can see that atoms contribute only in the longitudinal acoustic mode, since there are no second nearest atoms to contribute in the transverse acoustic modes. For distances larger than the second neighbour, the interactions follow the same pattern due to the symmetry of the system. If we use the equation 5.8 to calculate the interactions in the system for larger distances we will also be able to calculate mathematically why the LA has higher frequencies than the two TA.

This can be easily understood from figure 38 where I illustrate a 3-dimensional bcc crystal with the (1 0 0) plane vertical to the page. The bonds between atoms show the nearest neighbour interactions and the three

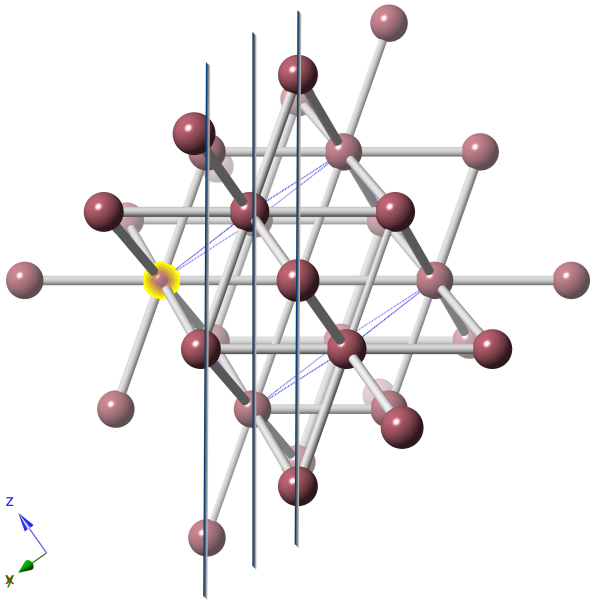

Figure 39: A bcc crystal at [1 1 1] direction parallel to the paper.

vertical lines represent the first three neighbour planes parallel to the (1 0 0) plane of the highlighted atom. The blue dotted lines represent the primitive unit cell for the bcc crystal. As we can see the highlighted atom interacts with four neighbour atoms with its first nearest plane. Because of the high symmetry the two TA and the one LA have the same force constant.

Similarly I can explain the dispersion curves along the other directions for the longitudinal and transverse acoustic modes. In order to explain the phonon−roton minimum I will focus on the explanation of the longitudinal acoustic mode along the [1 1 1] direction of a bcc material. In figure 39 I illustrate a bcc crystal with the (1 1 1) plane vertical to the page. The bonds between atoms show the nearest neighbour interactions and the three vertical lines represent the first three neighbour planes parallel to the (1 1 1) plane of the highlighted atom. The blue dotted lines represent the primitive unit cell.

As we can see in figure 39 the interactions between the highlighted atom

and the first neighbour plane include interactions with three nearest neighbour atoms. As we observe the projection of the atoms on the plane of the highlighted atom are at a wide angle making conceivable that the interaction with these atoms along the [1 1 1] direction are not that strong. The second neighbour plane does not involve any interaction with first neighbour atoms but only with second neighbour atoms, making the force constant between the initial atom and the atoms in the second neighbour plane weaker than the interactions of the the initial atom and the first neighbour plane. Interactions other than the nearest neighbour atom interactions do not strongly affect and their contribution can be neglected. The third neighbour plane does involve interactions with one first neighbour atom. As we can see from the figure this interaction is normal to the plane and we can understand that the contribution of this interaction to the longitudinal force constant along the [1 1 1] direction will be high, and more specifically even higher than the contribution of the interactions of the first plane to the highlighted atom. This can be understood physically if we try to compress the three planes towards the plane of the highlighted atom. The nearest neighbour atom on the third plane will collapse directly on the initial atom while atoms from the first plane will just come closer to the initial atom. This makes clear that the contribution of the interaction of the atom located on the third plane is the largest.

Mathematically this can be explained if we analyse the positions of the nearest neighbour atoms and their projections on the (1 1 1) plane. The first neighbour plane contributes with three nearest neighbour atoms. All three atoms are with an angle from the [1 1 1] direction. The formed angle, as discussed in the previous chapter, is either 70.53° or 109.47°. The absolute values of the cosine of both angles is equal to 1/3, making the distance to be 1/3 of the nearest neighbour atoms distance. So the projection of every nearest neighbour atom from the first plane on the [1 1 1] direction is $(x/r_{\mathrm{NNA}})^2 = (1/3)^3 = 1/9$. Similarly, the contribution of the nearest neighbour atom from the third plane is $(r_{\mathrm{NNA}}/r_{\mathrm{NNA}})^2 = 1$. Then, by using equation 5.9 similarly as in the calculation of equation 5.10 the interaction of the three nearest neighbour atoms of the first plane and the interaction of

the one nearest neighbour atom of the third plane along the [1 1 1] direction are

$$J_{\mathrm{x1}}^{[111]} = \frac{K}{3}, \quad J_{\mathrm{x3}}^{[111]} = K \tag{5.11}$$

Equation 5.11 demonstrates how much stronger is the interaction between the (1 1 1) plane with its third neighbour parallel plane.

From equation 5.8 I will calculate the phonon dispersion curve of the longitudinal acoustic mode for the [1 1 1] direction of a bcc system along the first three planes. If I define the distance between the planes as d then the phonon frequency for any bcc system along the first three planes

$$\omega_{\mathrm{LA}} = \sqrt{\frac{4}{m} J_{\mathrm{x1}}^{[111]} \sin^2\left(\frac{kd}{2}\right) + \frac{4}{m} J_{\mathrm{x3}}^{[111]} \sin^2\left(\frac{3kd}{2}\right)} \tag{5.12}$$

For a bcc system the distance of three planes is equal to the first neighbour atom distance. The first neighbour atom distance for a bcc material is $r_{\mathrm{NNA}} = a\sqrt{3}/2$ with a being the lattice constant, so $d = r_{\mathrm{NNA}}/3 = a\sqrt{3}/6$. Including the results from (5.11) and substituting the interplanar distance for bcc systems the equation 5.12 is equal to

$$\omega_{\mathrm{LA}} = \sqrt{\frac{4K}{3m} \sin^2\left(\frac{\sqrt{3}ka}{12}\right) + \frac{4K}{m} \sin^2\left(\frac{\sqrt{3}ka}{4}\right)} \tag{5.13}$$

From the last two equations it is easy to calculate that the contribution to the dispersion curve of the first plane minimises for the first time at $k = 4\sqrt{3}\pi/a$ and for the third plane $k = 4\sqrt{3}\pi/3a$.

In figure 40 I present the longitudinal phonon dispersion curves along the [1 1 1] direction of bcc barium as function of the wave vector times the unit cell length as described from equation 5.13. With blue curve I represent the dispersion curve from interactions only from the first nearest plane parallel to (1 1 1) plane and with green curve the dispersion curve from interactions only from the third nearest plane parallel to (1 1 1) plane. With the black curve I show the longitudinal dispersion curve for the system along the [1 1 1] direction as it is formed as a sum of interactions from the first three nearest

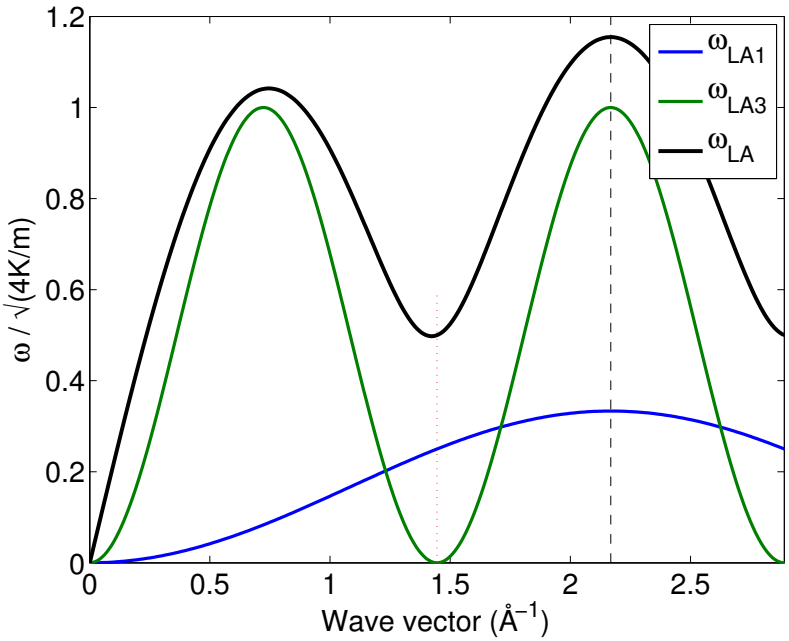

Figure 40: Longitudinal acoustic dispersion curves along the [1 1 1] direction for bcc barium. With blue and green line I represent the dispersion curves for the first and third nearest plane parallel to the (1 1 1) plane respectively, formed from interactions of the nearest neighbour atoms. The black line represents the sum of the previous two longitudinal dispersion curves along the [1 1 1] direction.

neighbour planes. With the black dashed line I represent the first Brillouin zone boundary for the (1 1 1) plane at

$$k_{\mathrm{ZB}} = \frac{\pi}{d} = \frac{2\sqrt{3}\pi}{a} \tag{5.14}$$

The figure 40 represents qualitatively any bcc system.

The dispersion curves for the first and third plane follow a sinusoidal wave pattern with minimum and maximum points as described in equation 5.13. The black curves which represents the sum of the previous two curves exhibits a similar pattern with minimum and maximum points. As we can see from figure 40 the black curve forms a minimum that does not go to zero. It is very interesting the similarity between the green and the black curve.

As we can see the first maximum point of the black curve is very close to the first maximum point of the green curve, but with higher magnitude, and the first minimum point of the black curve concurs with the minimum point of the green curve, but again at higher magnitude. This minimum point of the black phonon dispersion curve, which represents the phonon−roton regime, is highly affected from the interaction with the third neighbour plane atom, while the blue curve affects less the black curve contributing mostly in its magnitude.

Summarising the previous paragraphs, we can understand that the nearest neighbour interaction from the third parallel plane to the (1 1 1) plane affects the total longitudinal acoustic dispersion curve along the [1 1 1] direction. The nearest neighbour interactions from the first plane parallel plane to the (1 1 1) plane negligibly affects the dispersion curve. The third plane interactions affect the most due to geometry, since the nearest neighbour atom in the third plane is along the [1 1 1] direction and it involves a direct compression of the nearest neighbour bond. Interactions from the first plane involve three nearest neighbour atoms but the atoms are positioned at an angle to the [1 1 1] direction, so the projection of these atoms to the (1 1 1) plane is much smaller. Therefore interactions other than the nearest neighbour interactions are negligible and they do not drastically affect the longitudinal dispersion curve along the [1 1 1] direction.

The explanation I provided is universal and it applies to all monatomic bcc materials. The monatomic bcc case is a very basic and simple crystal formation and the calculation of the dispersion curves along the various directions is easy. Similarly someone can calculate the dispersion curves along various directions for other systems that exhibit the phonon−roton regime. Due to different geometry and higher complexity of various systems, such as non-monatomic systems, the calculations might be too complicated to be solved by hand. Nevertheless, if a similar approach will be followed similar results will be extracted, specific for each different system.

5.2 Summary and discussion

It is clear nowadays that the general belief about rotons and the roton minimum is that it is a phenomenon not strictly related to superfluid helium as it was initially believed. The phonon−roton regime can be seen in many non-superfluid materials and moreover not necessarily in liquids but in solids as well. So far there is no clear answer what creates the phonon−roton minimum but there are five major theories as I discussed in the beginning of this chapter. The first theory describes rotons as a quantum vortex, the second theory bases the formation of the minimum on single particle excitations, the third theory describes roton minimum as the stability point, the fourth theory includes changes in the lattice due to strong correlations and the fifth describes rotons as phonons highly affected by interatomic interactions at specific wave vector.

In section 5.1 I provide an extension of the theory of the phonon−roton minimum by discussing interatomic interactions in monatomic bcc materials. As I discussed, after a comprehensive calculation of the interatomic forces in crystals, I proved the connection between the formation of the phonon−roton minimum and the interatomic interactions in local structure. More specifically I showed how the local order in a crystal along the direction which the phonon−roton minimum is formed affects the interactions of the system so the minimum is formed. I focused on the example of a monatomic bcc crystal, where the phonon−roton minimum can be observed on the longitudinal acoustic mode along the [1 1 1] direction. For this case I showed that the third neighbour plane interactions of the nearest neighbour atoms affect most the system, providing the strongest interaction and forming a local minimum at the wave vector were the phonon−roton minimum is exhibited.

Although the explanation I provide is based on a monatomic bcc crystal this theory can be expanded to more complicated systems. It is important to note that more complicated systems require more complicated solutions. Moreover, the interactions for various crystals depend on the order of the crystal and a 3-dimensional solution requires computational solution through a more generic model. Also, the calculation of interatomic interactions of

a non-crystalline material, such as amorphous or liquid materials, would require statistical solution (such as averaging of distances and interactions), leading to not very clear or accurate results. The key point of identifying the minimum is the study of the atomic motion in the longitudinal direction, where the interactions are stronger.

In all previous chapters I discuss the correlation of the local order of crystals, amorphous and liquids. More specifically in chapter 4 I studied the population and the angles between bonds in local structure, showing that amorphous and liquids hold very similar structure as this of the corresponding material. Moreover, in chapters 3 and 4 I presented results from INS from experiments and simulations for materials in crystalline, amorphous and liquid phase which exhibit similar spectra at low and intermediate values of the wave vector, showing a clear connection between the dynamics of three phases. Therefore it is reasonable to conclude that the interatomic interactions in short range order of the three phases can be compared, especially interactions from the nearest neighbour interactions which are the strongest in the system. As a conclusion, I can say that the presented theory on the formation of the phonon−roton theory for the monatomic bcc crystal can be expanded to the corresponding amorphous and liquid system.

Although there is a connection of the local structure of a material in the three different phases, the interactions are not exactly the same. This is something known from theory and can be seen in the results in sections 4.3.1 and 4.3.2 on the population and angles between bonds in the local structure analysis. Nevertheless, the interactions are very similar and it is logical to conclude that the theory on the formation of the phonon−roton minimum for liquids can be treated as an approximation of the theory for crystals. The study of phonon dispersion curves of amorphous or liquid materials include approximations and rough averaging of phonon frequencies so it is very difficult to evaluate the theoretical results.

The difficulty of the evaluation of the theory for liquids can be seen if I compare results from previous chapters with the theoretical results. Using as case study results from crystalline barium, the phonon−roton minimum is defined at the point where the interaction with the nearest neighbour atom

of the third plane in the longitudinal direction tends to zero. This is at

$$\mathbf{Q}_{\text{theory}}^{\text{crystal}} = \frac{4\sqrt{3}\pi}{3a_{Ba}} = 1.45\text{Å}^{-1} \tag{5.15}$$

while the phonon−roton regime is roughly defined from $\mathbf{Q}_{\text{theory}}^{\text{crystal}} = 1.40$ Å^{-1} to $\mathbf{Q}_{\text{theory}}^{\text{crystal}} = 1.50$ Å^{-1}. The results from INS from experiments for barium are not clear. Calculating straight from the colour map of collective excitation spectra for the re-crystallised barium in figures 9 and 10 the phonon−roton regime is roughly defined from $\mathbf{Q}_{\text{exp}}^{\text{crystal}} = 1.43$ Å^{-1} to $\mathbf{Q}_{\text{exp}}^{\text{crystal}} = 1.58$ Å^{-1}. Similarly for the liquid case from figures 7 and 8 the phonon−roton regime is roughly defined from $\mathbf{Q}_{\text{exp}}^{\text{liquid}} = 1.42$ Å^{-1} to $\mathbf{Q}_{\text{exp}}^{\text{liquid}} = 1.63$ Å^{-1}. By using the conversion factor from Fe to Ba as in equation 4.14, the results straight from the inelastic spectra for iron from simulations, for the crystal from figure 15 the phonon−roton regime is roughly defined from $\mathbf{Q}_{\text{sim}}^{\text{crystal}} = 1.39$ Å^{-1} to $\mathbf{Q}_{\text{sim}}^{\text{crystal}} = 1.68$ Å^{-1}, while for glass from figure 16 the phonon−roton regime is roughly defined from $\mathbf{Q}_{\text{sim}}^{\text{amorphous}} = 1.37$ Å^{-1} to $\mathbf{Q}_{\text{sim}}^{\text{amorphous}} = 1.82$ Å^{-1}.

It is clear enough that the estimation of the of the phonon−roton minimum regime from collective excitation spectra is very rough and should be avoided. Despite the fact, as we can see from the previous estimations the results from theory for the crystal are a subset of the results from experiments and simulations, for all three states. Although this does not provide a clear evaluation of the theory, it shows that the theoretical values are included to those from experiments and simulations making the theory valid for the simple case of barium. This theory needs to be extended and verified for more complicated cases but it is expected to work similarly as in the simple bcc case.

6 The heat capacity of matter beyond the Dulong−Petit value

In this chapter, I focus on the heat capacity (C) of solids and liquids and the unsolved problem of the of heat capacity of liquids. I will present a literature review on approaches to calculate the heat capacity of solids and liquids, where I will mention their predictive power and their limitations. This chapter is not directly connected to previous chapters but it contributes in the understanding of macroscopic connection of dynamics between solids and liquids.

My approach involves a theoretical approach based on Trachenko's and Brazhkin's theory [6] on heat capacity at the glass transition and a computational approach using atomistic MD simulations for various crystalline, amorphous and liquid systems. In this theory the authors introduce a new equation for the calculation of heat capacity under constant volume (C_{V}) in order to explain various physical phenomena. In the original paper [6] the authors propose an new explanation of the heat capacity jump at the glass transition temperature (T_g). They discuss time-dependent effects of glass transition and identify three distinct regimes of relaxation. They study how elastic, vibrational and thermal properties on liquids change on cooling and they explain the widely observed logarithmic increase of T_g with the quench rate and the correlation of the heat capacity jump with liquid fragility.

Furthermore, this theory extends and contributes in more topics. Such are the subject of spin glass transition [146] where they introduce the structural glass transition as entirely dynamic procedure and they correlate it to the spin glass transition. Moreover to the subject of duality of glasses [147] where they explain how liquid thermodynamics are comparable to solid thermodynamic properties and how liquid flowing is very close to gas flowing. Furthermore to the subject of supercritical fluids [148] by studying the thermodynamic properties of the supercritical state and the subject of phonon theory of liquids [149] where they study thermodynamic properties of liquids at low temperatures and they propose a new phonon approach that avoids common problems in previous theories.

Moreover, this theory has been used for the estimation of the effect of anharmonicity in the calculation of liquid [150] and solid [151] heat capacity, which is the main subject of this chapter. I will test this theory by doing classical molecular dynamics simulations for various materials and I will present results that are in a good agreement with the theory. Finally I will try to explain the interesting behaviour of the liquid heat capacity.

6.1 Introduction to heat capacity

Thermodynamics is the part of physical sciences that is related to the heat and its relation to other forms of energy and work. It defines macroscopic variables, such as temperature, entropy and pressure, that describe average properties for every system and explains how they are related and by what laws they change. Heat capacity is a thermodynamic property easily accessible through experiments.

Heat (Q) is defined as the energy transferred from one system to another by thermal interaction. By definition, heat capacity (C) is the heat that is required to produce a given change in temperature. Heat capacity belongs to the most important thermo-physical properties of matter. It is closely related to the temperature dependence of fundamental thermodynamic functions and it links thermodynamics with structure and dynamics.

The internal energy (U) of a closed system changes either by adding or subtracting heat to the system or by the system's performing work (W) $\mathrm{d}U = \delta Q + \delta W$. As a result of an increase of system's volume, the change in work can be written as $+\delta W = -P\mathrm{d}V$. Under constant volume conditions, the second term of internal energy (δW) vanishes and heat becomes equal to energy. The heat capacity under constant volume is defined as

$$C_V = \left(\frac{\partial U}{\partial T}\right)_V = \left(\frac{\partial Q}{\partial T}\right)_V \tag{6.1}$$

When the total energy of a system is equal to system's internal energy then C_V is simply defined as

$$C_V = \left(\frac{\partial E}{\partial T}\right)_V \tag{6.2}$$

In the same way, a change in the enthalpy (H) of a system is given by $dH = \delta Q + VdP$ and under constant pressure conditions heat capacity under constant pressure (C_{P}) is defined as

$$C_P = \left(\frac{\partial H}{\partial T}\right)_P \tag{6.3}$$

Both C_{V} and C_{P} are property relations and are therefore independent of the type of process. These two properties are connected by using this equation

$$C_P - C_V = VT\frac{\alpha^2}{\beta_T} \tag{6.4}$$

where α is the coefficient of thermal expansion and β_T is the isothermal compressibility.

The coefficient of thermal expansion of a system refers to the dimensional (volume) change of a system as a function of temperature. For isotropic materials, where all their properties are the same in all directions, α has the same value for the whole system [152–154] and is defined as

$$\alpha = \frac{1}{V}\left(\frac{\partial V}{\partial T}\right)_P \tag{6.5}$$

The compressibility is a measure of the relative volume change of a fluid or solid as a response to a pressure or mean stress change. Isothermal compressibility is defined as

$$\beta_{\mathrm{T}} = -\frac{1}{V}\left(\frac{\partial V}{\partial P}\right)_T \tag{6.6}$$

The inverse of isothermal compressibility is called bulk modulus (B), which is a measure of the resistance of a crystal against compression and is defined as

$$B_{\mathrm{T}} = -V\left(\frac{dP}{dV}\right)_T \tag{6.7}$$

All the above properties are highly related to heat capacity and I will extensively use them in the next paragraphs. α is a key parameter in my theory

in order to explain the effect of ahnarmonicity in a system's heat capacity.

6.2 Theories on the prediction of heat capacity

6.2.1 Heat capacity of solids

Heat capacity has extensively been studied since the beginning of the 19^{th} century. Many models for the theoretical estimation of C_{V} exist and they give a good approximation under specific conditions. The most common models include the Dulong and Petit model [21] which is the first one, the Einstein model [155] and the Debye model [156] which is the most famous model at present.

In the harmonic approximation, where a crystal is treated as harmonic, if $u_{l,\alpha}$ describes a component of the vector displacement ($\alpha = x, y, z$) of the l atom from its equilibrium position, the energy can be expressed as a Taylor expansion

$$\begin{aligned} E = E_0 + \frac{1}{2} \sum_{\substack{l,l' \\ a,a'}} \frac{\partial^2 E}{\partial u_{l,\alpha} \partial u_{l',\alpha'}} u_{l,\alpha} u_{l',\alpha'} + ... \\ + \frac{1}{n!} \sum_{\substack{l^1,...,l^n \\ a^1,...,a^n}} \frac{\partial^n E}{\partial u_{l^1,\alpha^1} ... \partial u_{l^n,\alpha^n}} u_{l^1,\alpha^1} ... u_{l^n,\alpha^n} + ... \end{aligned} \tag{6.8}$$

where E_0 is the equilibrium lattice energy. In this expansion there is no first-order term because by the definition of equilibrium all residual forces are zero. The second-order term is called harmonic energy. All higher-order terms are classed together as the anharmonic energy, which are neglected in the harmonic approximation.

The harmonic model is useful for lattice dynamics properties but not for other features as the thermal expansion [157]. In the harmonic model the forces produce simple harmonic motion, in which there is a constant exchange of energy between kinetic and potential. From the concept of the equipartition theorem, a system with $3N$ atoms has average kinetic energy of $\langle KE \rangle = \frac{3}{2} N \mathrm{k_B} T$. The mean value of the potential energy (P_E) is equal to

the mean value of the kinetic energy

$$\langle E \rangle = \langle K_E \rangle + \langle P_E \rangle = 3N\mathrm{k_B}T \tag{6.9}$$

From this equation we can calculate the heat capacity under constant volume

$$C_V = \frac{\mathrm{d}}{\mathrm{d}T} 3N\mathrm{k_B}T = 3N\mathrm{k_B} \tag{6.10}$$

This corresponds to the classical treatment of the vibrations of the atoms at high temperatures. The equation 6.10 can also be transformed to $C_V = 3N\mathrm{k_B} = 3\mathrm{R}$, where R is the gas constant. This result is the Dulong and Petit law that it was empirically noted in 1819 and it equals to 24.94 $\mathrm{Jmol^{-1}K^{-1}}$.

This law implies that the heat capacity of solids at high temperatures is constant and depends only on the number of atoms of the system and not on the temperature. At high temperatures this law is well satisfied for common materials but experimentally it has been noticed that the law is not satisfied at low temperatures and near zero temperature the heat capacity is zero. According to Walton [158] this failure originates from the inability of classical mechanics to describe correctly the motions of bound atoms.

The first approach that tried to surpass the Dulong and Petit's law failure came many years later from Einstein, in 1906. Einstein made three assumptions in his model for the heat capacity of solids. Firstly, he assumed that each solid is composed of a lattice structure consisting of N atoms and each atom was treated as moving independently in three dimensions within the lattice so there are 3 degrees of freedom. This means that the entire lattice's vibrational motion could be described by a total of $3N$ motions, or degrees of freedom. That proved to be accurate and experimental data supported his hypothesis. Secondly, he assumed that the atoms inside the solid lattice do not interact with each other. The second point is not accurate and a simple explanation is that if atoms inside a solid could not interact, the sound or heat could not propagate through it. Thirdly, he treated the N atoms in a crystal as $3N$ simple harmonic oscillators, all having the same angular frequency (ω) and this highlights the main difference between Einstein's and Debye's model.

The Einstein model provides a good qualitative description of a solid's heat capacity at high temperatures, but it is not used because it does not reproduce accurately the behaviour at very low temperatures. This is because at low temperature the energy of the Einstein phonon, $\hbar\langle\omega\rangle$ is significantly above the thermal energy, which is equal to $\mathrm{k_B}T$, and is barely excited. Moreover, a crystal has also acoustic modes with small wave vectors, with phonon energies lower than the thermal energy. So, the actual failure of the Einstein model is the inability to describe the contribution of the acoustic modes to the thermodynamic functions at low temperatures. This problem was surpassed by Debye's model on heat capacity of solids.

The Debye model is a method developed in 1912 to estimate the phonon contribution to the heat capacity of a solid. The Debye model for heat capacity explains better the problem of representing the contribution of the acoustic modes. Debye's observation is that there is a maximum number of vibrational modes in a solid. This model treats the vibrations of the atomic lattice as phonons in a box, in contrast to the Einstein model, which treats the solid as many individual, non-interacting quantum harmonic oscillators.

Moreover, the Debye model treats the coupled vibrations of the solid in terms of $3N$ normal modes of vibration of the whole system, with each one having its own frequency. The lattice vibrations are therefore equivalent to $3N$ independent harmonic oscillators. For low frequency vibrations, which are defined as vibrations with wavelength much greater than the atomic spacing, $\lambda \gg a$ or very small wave vector, the crystal may be treated as a homogeneous elastic medium. The normal modes are the vibrations of the standing waves that exist in the solid. The phonon energy as defined by Debye is

$$E = \int_0^{\omega_\mathrm{D}} \frac{3V\omega^2}{2\pi^2 v_{\mathrm{sound}}^3}\hbar\omega \frac{1}{\exp\left(\hbar\omega/\mathrm{k_B}T\right)-1}\mathrm{d}\omega \tag{6.11}$$

where ω_D is the effective cut-off Debye frequency, V is volume of the system and v_{sound} is the speed of sound. By deriving the energy with temperature the heat capacity for the Debye model is defined as

$$C_V = \int_0^{\omega_\mathrm{D}} \frac{3V\omega^2}{2\pi^2 v_{\mathrm{sound}}^3}\hbar\omega \frac{\partial n}{\partial T} d\omega \tag{6.12}$$

n is the phonon number and is defined as $n = (\exp(\hbar\omega/\mathrm{k_B}T) - 1)^{-1}$. The ω_D can be adjusted to give the best agreement with experiment, obtaining a value of ω_D for each temperature. The equation 6.12 is a common way to represent the heat capacity of solids.

When substituting $x = \hbar\omega/\mathrm{k_B}T$ in the equation 6.11, thus $\omega^3\mathrm{d}\omega = (\mathrm{k_B}T/\hbar)^4\, x^3\mathrm{d}x$, the energy takes the form

$$E = \frac{3V\hbar}{2\pi^2 v_{\mathrm{sound}}^3}\left(\frac{\mathrm{k_B}T}{\hbar}\right)^4 \int_0^\infty x^3(e^x - 1)^{-1}dx \tag{6.13}$$

and knowing that the integral is of a standard form that results to $\pi^4/15$, the equation 6.13 is equal to

$$E = \frac{V\pi^2(\mathrm{k_B}T)^4}{10(v_{\mathrm{sound}}\hbar)^3} \tag{6.14}$$

and the heat capacity is

$$C_V = \frac{2V\pi^2\mathrm{k_B}}{5(v_{\mathrm{sound}}\hbar/\mathrm{k_B})^3}T^3 \tag{6.15}$$

For N atoms and by including the Debye temperature $\theta_\mathrm{D} = (\hbar\omega_\mathrm{D}/\mathrm{k_B})$, the Debye's heat capacity can be written as

$$C_V = \frac{12\pi^4 N\mathrm{k_B}}{5}\left(\frac{T}{\theta_\mathrm{D}}\right)^3 \tag{6.16}$$

That gives an important conclusion that the heat capacity is proportional to cubic temperature ($C_V \propto T^3$). In the low temperature limit, the limitations of the Debye model mentioned earlier do not apply, and it gives a correct relationship between heat capacity, temperature, the elastic coefficients and the volume per atom. Although the Debye model is well satisfied in all temperatures for monatomic solids, it fails for more complex systems [159–168], something that makes it a non-universal model. Dulong and Petit law, Einstein model and Debye model are the three most discussed models for theoretical prediction of heat capacity under constant volume but they all have temperature or system limitations that make them unrealistic and

unreliable models.

The previously mentioned models describe harmonic crystals, something that is unrealistic [169, 170]. In reality all crystals behave anharmonically. The word anharmonic describes any oscillator with generalised forces that deviate from linearity with generalised coordinates, thus the deviation of a system from being a harmonic oscillator. Anharmonicity plays an important role in determining the thermodynamic properties of crystals. As it has been observed, amongst the thermodynamic properties the most greatly affected properties due to anharmonicity are entropy and heat capacity [171]. These are particularly sensitive to changes in low vibrational frequencies, which are frequently the most heavily affected by anharmonicity and mode coupling. Anharmonicity is responsible for the deviation of the specific heat from the Dulong and Petit law at high temperatures and also for other thermodynamic properties such as the thermal expansion.

As I mentioned earlier, experimentally it is known that C_{V} is almost never $3\mathrm{Nk_B}$, not even at the classical limit $\hbar\omega_{\mathrm{D}}/\mathrm{k_B}T \ll 1$, where ω_{D} is the Debye frequency. Many authors agree that this behaviour is attributed to the anharmonicity of interatomic interactions [172–178]. On general grounds the harmonic approximation for describing the vibrational properties of solids becomes less adequate with increasing temperature, as the vibrational amplitudes increase. However, the harmonic theory is still not completely adequate even at low temperatures (when $T < \theta_{\mathrm{D}}$) . The existence of anharmonicity is observed even at absolute zero [179, 180] because of zero-point vibrations.

If there were no anharmonic effects many physical properties could not be described. For example there would be no thermal expansion. The force and elastic constants would be independent of temperature and the specific heats at constant pressure or volume would be equal. Moreover a phonon−phonon interaction could not be defined and a crystal would vibrate infinitely. Also properties as thermal conductivity could not be explained with the harmonic approximation [181].

The thermal expansion can be described using the harmonic phonon theory in which the harmonic frequencies are assumed to be functions of volume, by involving the Grünesien approximation. The Grünesien parameter

is a very useful experimental quantity for the quasi-harmonic approximation [182]. The word quasiharmonic accounts for the effects of thermal expansion on phonons, effects that are not strictly harmonic. An implicit assumption of the quasiharmonic theory is that an oscillation has a well-defined, long-lived, harmonic-like frequency that changes modestly and predictably with changes in temperature and pressure [183]. In this approximation the softening of the phonon frequencies is quantified via the mode Grüneisen parameter (γ), which is equal to

$$\gamma_i = -\frac{V}{\omega_i}\left(\frac{\partial \omega_i}{\partial V}\right)_T \tag{6.17}$$

This equation is a simple function, free of adjustable parameters and provides direct calculations. Nevertheless, the C_V was never calculated so far through the Grünesien approximation. In the section 6.3 I will review these methods and I will describe a new simple method to evaluate the effect of anharmonicity on heat capacity.

6.2.2 Heat capacity of liquids

While there are many theories and a good theoretical understanding of the heat capacity of both solids and gases, a general theory of the heat capacity of liquids is absent. The heat capacity of liquids should be a very simple property to calculate since it requires very few assumptions. Most of the approaches for liquids' heat capacity calculation have been made through gas phase theories or solid phase theories but none of them have a explicit theory for liquids.

As, it has been noticed by Frenkel [184], there are similarities of liquids and solids near the melting point, so the molecular organisation in liquid at these temperatures is similar to the corresponding solid, so is C_V. Also, at high temperatures, the rotation and translation may approach the conditions of a gas, which is almost free. In this case the C_V of liquids at high temperature approaches that of the corresponding gases [185]. The lack of prediction of C_V for liquids is more obvious for temperatures between T_m and

T_c, where T_m is the melting temperature and T_c is the critical temperature. Experiments on simple [186, 187] and complex [188] liquids show that C_V of liquids decreases with temperature from the classical Dulong−Petit value of $3k_BN$ to $2k_BN$ at high temperature, something that can not be explained through theories for solids or gases.

The most common approach for the calculation of C_V of liquids comes from the gas phase. For the calculation of liquid energy one can use the kinetic energy of a gas plus the potential energy of interatomic interactions for solids ($E = K + U$). For gases, the atoms move much faster than the liquid atoms and the interactions between atoms for gas are weak while for liquids are much stronger. Additionally, the interatomic interactions depend on each system, thus the calculation of the liquid energy becomes system depended. Thus, this approximation can not describe a realistic liquid model but only dense gases. A different approach for the direct calculation of C_V for simple materials such as noble gasses at high temperature, was based on the Dulong−Petit equation, $C_V = 3Nk_B + \delta C$, where according to Brillouin [189] δC is the change in C_V and it takes values from 0 to $-R$ when going from T_m to T_c, as the shear waves are lost. This explanation is not always correct since it was noticed that δC for lower temperatures close to T_m is often positive [190].

Approaches from the solid phase usually use the interstitial theory which provides a model that unifies crystalline, glassy and liquid states. According to this theory, simple liquids are presented like crystals that contain a small percentage of crystal cells in thermal equilibrium or they are presented like glasses that are frozen liquids. These theories can predict that the heat capacity of liquids decreases exponentially with temperature at a specific rate, something that is well satisfied with experimental data [191]. Yet, this theory focuses on simple materials and does not apply for more complex ones.

A different approach for the calculation of liquid energy and liquid C_V from the solid phase is through the elastic properties [192]. By taking into account the vibrational states of a glass, the author calculates the energy and the C_V for the liquid phase and predicts the change from $C_V = 3k_BN$ to almost $C_V = 2k_BN$. That is due to the increasing loss of two transverse

modes with frequency $\omega < 1/\tau$ [192]. This theory is based on Frenkel's theory of liquid flow [193] that states that the only difference from a solid glass and a liquid is the relaxation time (τ). This is based on the continuity of the transition from glass to liquid, so the vibrational states of the liquid just above the glass transition temperature do not change from the vibrational states of the glass. This model works well with simple classical liquids but not for quantum liquids.

The previous theories are harmonic theories and do not take in account the effect on anharmonicity. In the harmonic approximation the phonon frequencies are considered to be temperature independent. In the anharmonic approximation the phonon frequencies depend on the temperature and more specifically decrease with temperature, and highly affect properties such as the coefficient of thermal expansion. Especially for the liquid phase, where the coefficient of thermal expansion is much higher than the solid's phase, the effect of anharmonicity has an important role that I will try to explain in the next paragraphs.

6.3 Evaluation of the effect of anharmonicity on heat capacity

The anharmonicity of matter is a main topic and there is a large amount of research about the anharmonicity of solids and how it affects thermodynamic properties [173,177,194]. That led to a good qualitative understanding about the effect of the anharmonicity, with the most common approach to evaluate it, the expansion of potential energy U in Taylor series, in a similar way as in equation 6.8, including higher order terms. In this expansion, the derivatives of the potential energy with the atomic displacements in equilibrium conditions are the anharmonic coefficients that according to Cowley [173] are very complicated to evaluate even for known potential functions.

For crystals, this approach involves the summation over the wave vectors $\mathbf{k}$, but for other configurations such as glasses the wave vectors are not defined, something that limits this method. For liquids this approach is even more unrealistic since the displacement of the atoms is random and non peri-

odic. Even in crystals, due to approximations the estimation of the potential energy is accurate only in the same order of magnitude.

The main problem in accurate calculation of the potential energy and the effect of anharmonicity is the lack of well defined models for describing interatomic forces [172, 173, 175, 176], which makes it a limiting factor for many quantitative calculations. For most solids apart from the lightest elements the anharmonicity appears generally to be small enough [182] and that is why if the models for interatomic forces do not describe with high quality the forces, the anharmonic part is difficult to be defined. Calculations through experimental data such as phonon lifetimes and frequency shifts are still not enough for a good estimation of the anharmonic effects and anharmonic expansion coefficients, since there are complications in the calculations that limit the predictive power of the theory [173].

As it is clear from the literature, there is need for a general method for the estimation of anharmonic heat capacity. For the problem of glass transition, Trachenko and Brazhkin have proposed a formula [6] for the evaluation of the effects of anharmonicity in heat capacity. The equation of C_{V} over $\mathrm{k_B}$ is

$$C_V = 3N(1 + \alpha T) \tag{6.18}$$

where α is the coefficient of thermal expansion. In equation 6.18 all the potentially complicated effects of anharmonicity are evaluated by using only one parameter the coefficient of thermal expansion. α is a system related parameter and not adjustable, and can be easily calculated regardless the complexity of the system. In the following paragraphs, I will try to extract and extend the equation 6.18 in a similar way described in the original paper.

At high temperature the free phonon energy over $\mathrm{k_B}$ of a harmonic solid is defined as

$$F = 3NT \ln \frac{\hbar\bar{\omega}}{T} \tag{6.19}$$

where $\bar{\omega}^{3N} = \omega_1\omega_2...\omega_{3N}$ is the averaged phonon frequency as introduced by Landau and Lifshitz [195]. The free phonon energy is in energy over Boltzman's constant units. Then the entropy is the derivative of the free energy with respect of temperature and is defined as $S = -\left(\partial F/\partial T\right)_V =$

$3N\,(1+\ln T/\hbar\bar{\omega})$. By definition $C_V = T\,(\partial S/\partial T)_V = 3N$ which leads to the classical Dulong−Petit result.

For the anharmonic case we assume that omega depends on temperature and in fact it decreases as temperature increases. The entropy is

$$S = 3N\left(1+\ln\frac{T}{\hbar\bar{\omega}} - \frac{T}{\bar{\omega}}\frac{\mathrm{d}\bar{\omega}}{\mathrm{d}T}\right)_V \tag{6.20}$$

The additional terms in free energy and entropy of the anharmonic crystal come from both the thermal expansion and the intrinsic anharmonicity. By definition, C_V is the derivative of the entropy with respect with temperature. For the calculation of C_V someone should know the values of the entropy's term $\mathrm{d}\bar{\omega}/\mathrm{d}T$. For the definition of this term there is no straightforward way and various assumptions should be taken into account.

The phonon pressure is the derivative of free energy with respect with volume and is defined as

$$P_\mathrm{ph} = -\left(\frac{\partial F}{\partial V}\right)_T = \frac{3NT\gamma}{V} \tag{6.21}$$

where γ is the averaged Grüseisen parameter, defined in equation 6.17, and is equal to $\gamma = (1/3N)\sum_{i=1}^{3N}\gamma_i$. By definition $B_\mathrm{ph} = -P_\mathrm{ph} = -(3NT\gamma(q-1)/V$, so

$$\left(\frac{\partial B_\mathrm{ph}}{\partial T}\right)_V = -\frac{3N\gamma(q-1)}{V} \tag{6.22}$$

where $q = \partial\ln\gamma/\partial\ln V$ and is the Grüneisen's parameter volume dependence and γ can be represented in q as $\gamma = \gamma_0\,(V/V_0)^q$, where γ_0 is defined in ambient conditions. Experimental values show that q has similar value for a variety of systems, so for simplicity reasons I can omit the $(q-1)$ term since it does not affect the order of magnitude calculations of C_V and redefine the equation 6.22 as

$$\left(\frac{\partial B_\mathrm{ph}}{\partial T}\right)_V = -\frac{3N\gamma}{V} \tag{6.23}$$

Typical vales for q are $q = 2.1$ for Pb, $q = 3.2$ for Ge [194], $q = 1.4$ for MgO [177], 1.5 - 2.0 for alkali halides [196] and 1.7 for $MgSiO_3$ [197].

The total bulk modulus is defined as $B = B_0 + B_{\rm ph}$, where B_0 is the bulk modulus at zero temperature. Moreover, by using the known formula $\gamma = V\alpha B/C_V$ we can replace the equation 6.23 as

$$\left(\frac{\partial B_{\rm ph}}{\partial T}\right)_V = -\alpha(B_0 + B_{\rm ph}) \tag{6.24}$$

For the case of small αT the formula 6.24 implies that $B \propto -T$.

The small αT is often the case for experimental temperature range and according to experiments [177] the above relation between bulk modulus and temperature is verified for both constant pressure and constant volume [198–200]. This is justified because of the intrinsic anharmonicity related to the softening of the interatomic potential at large vibrational amplitudes, and moreover because of an additional contribution from the thermal expansion [6]. After extending the bulk modulus I will try to correlate B with $\bar{\omega}$. For the acoustic modes, it is known that $v_{\rm sound} = \sqrt{B/\rho}$, where ρ is the density and moreover $\omega_i = kv_{\rm sound}$. That means that ω_i^2 is proportional to B, so $\bar{\omega}^2 \propto B$, something that is true for any system as long as the phonon spectrum is treated by the Debye approximation. This result is verified also for the optic modes case for both longitudinal and transverse phonon frequencies over a wide temperature range [201] and over a wide pressure range [202]. That comes to the conclusion that $\bar{\omega}^2 \propto B_0 + B_{\rm ph}$ and through the equation 6.24 it is concluded that

$$\frac{1}{\bar{\omega}}\left(\frac{d\bar{\omega}}{dT}\right)_V = -\frac{\alpha}{2} \tag{6.25}$$

This equation highlights the effect of intrinsic anharmonicity in the system.

Continuing from the equation 6.20 the anharmonic $C_{\rm V}$ is

$$C_V = 3N\left[1 - \frac{2T}{\bar{\omega}}\frac{{\rm d}\bar{\omega}}{{\rm d}T} + \frac{T^2}{\bar{\omega}^2}\left(\frac{{\rm d}\bar{\omega}}{{\rm d}T}\right)^2 - \frac{T^2}{\bar{\omega}}\frac{{\rm d}^2\bar{\omega}}{{\rm d}T^2}\right] \tag{6.26}$$

By using the assumption that $({\rm d}\bar{\omega}/{\rm d}T)_V \propto \bar{\omega}$ the last two terms of equation 6.26 cancel out. By using the result of the equation 6.25 the term $-(2T/\bar{\omega})({\rm d}\bar{\omega}/{\rm d}T)$ is equal to $+\alpha T$. This makes equation 6.26 equal to equation 6.18, $C_V = 3N(1 + \alpha T)$, which provides a straightforward way for the

estimation of the anharmonic effects in C_{V}. The relationship of C_{V} and α is due to the softening of the bulk modulus with temperature at constant volume due to the intrinsic anharmonicity [183], an effect that can be related to coefficient of thermal expansion in the Grüneisen approximation. The equation can be used to evaluate anharmonicity not only in crystals but also in glasses and liquids, for which calculations based on anharmonic expansions such as Taylor series expansion do not work.

For the equation 6.18 we can make the same assumption as that for equation 6.23 that the $(q-1)$ term can be neglected. For more precise calculations, this term can be included and then the equation 6.24 can be written as

$$\left(\frac{\partial B_{\mathrm{ph}}}{\partial T}\right)_V = -\delta(B_0 + B_{\mathrm{ph}}) \tag{6.27}$$

where $\delta = \alpha(q-1)$ [151]. Then, by combining (6.27) with $\bar{\omega}^2 \propto B_0 + B_{\mathrm{ph}}$ and following the same procedure as earlier we can conclude that $(1/\bar{\omega})(\mathrm{d}\bar{\omega}/\mathrm{d}T)_V = -(\delta/2)$. Combining this result with equation 6.26 we can write [151]

$$C_V = 3N(1 + \delta T) \tag{6.28}$$

Similarly but more accurately, δ represents all the anharmonic effects in heat capacity calculations. This parameter quantifies the decrease of B with temperature at constant volume.

As I mentioned, the equation 6.18 applies for many different systems such as crystals, glasses and liquids. In the next section I will present the methodology of how to test and verify this equation, and the various systems I have used. For my calculations I will try to demonstrate an order of magnitude evaluation of C_{V} so I will not use the equation 6.28 but the equation 6.18. I will present results from classical molecular dynamics simulations for these systems in different ensembles for a wide temperature range and I will calculate the effect of anharmonicity for them.

6.4 Case study for solids and liquids

This section is about verifying and evaluating the previously discussed theory with results from simulations. All the simulations I performed are classical molecular dynamics simulations. In previous chapter I mentioned the benefits of classical molecular dynamics, while in this section I will describe the benefits of using MD for the specific case, the systems I used, the methodology and the results about the effect of anharmonicity in C_{V}.

In the calculation of C_{V} there are two main benefits for using classical MD. Experimentally, the calculation of heat capacity under constant volume is through heat capacity under constant pressure. The C_{V} is very difficult to be measured experimentally due to physical restrictions in experiments under constant volume. In contrary, C_{P} is easy to be measured. The calculation of C_{V} comes through the equation 6.4. Still, there are many experimental uncertainties in the definition of α and β_T (or bulk modulus), particularly at high temperature where the calculation of C_{V} is inaccurate. This problem does not arise in MD simulations where it is possible to easily perform simulations under constant volume.

The second issue that classical MD easily surpass are the calculations close to the classical limit $\hbar\omega_{\mathrm{D}}/T \ll 1$ where $C_V = 3N$. This limit is not easy to be achieved in many experimental systems due to high Debye frequency [177]. That often makes unclear to what extent the deviation of experimental C_{V} from $3N$ is due to anharmonicity or the quantum effect of phonon excitation. This issue does not arise in classical MD simulations that I use for my calculations.

6.4.1 Materials

To prove the universality of the theory in my simulations I involve a variety of materials with different structures and symmetries, as well as a variety of interatomic potentials. In table 1 I describe the chemical formula, the structure and the space group for crystals, the number of the atoms in the system and the interatomic potential I used. The range of materials include single elements, oxides, ionic crystals and more complex systems while

Table 1: Materials used for calculation of α

Material	*Structure - Space Group*	*No. of Atoms*	*Potential*
Al_2O_3	Trigonal - $R\bar{3}c$	14,400	Buckingham[204]
Ar	Liquid	64,000	Lennard−Jones[205]
Ar	FCC - $Fm3m$	32,000	Lennard−Jones[206]
Ge	Diamond - $Fd3m$	27,000	Tersoff[80]
NaCl	FCC - $Fm\bar{3}m$	27,000	Buckingham[207]
SiO_2	Amorphous	12,288	Buckingham[208]
TiO_2	Tetragonal - $P4_2/mnm$	23,520	Buckingham[209]
$ZrSiO_4$	Tetragonal - $I4_1/amd$	17,496	Buck. & Morse[210,211]

structure includes various cubic, trigonal,tetragonal, glasses and liquids.

Most of the materials have crystalline structure and most specifically for Al_2O_3 and TiO_2 I used corundum and rutile structure respectively, which are the non default crystal structures for these materials. The SiO_2 is in amorphous state, as described in reference [203]. For argon I used two different configurations, one with fcc structure and one which represents a binary liquid in the supercooled viscous state. I use the binary system in order to avoid crystallisation of the system and represent a high-viscous liquid at low temperatures and a low-viscous liquid at high temperatures. Apart from these materials I tested few other systems such as C ($Fd3m$), GeO_2 (amorphous) and MgO ($Fm\bar{3}m$). C, GeO_2 and MgO with Ge, SiO_2 and NaCl respectively have the same crystalline structure and I will not proceed with further investigation for these materials.

The number of atoms is in the same order of magnitude for all the materials, between 12,000 and 64,000 atoms. Systems of this size are generally considered to be sufficient for describing realistically and accurately physical systems and properties in MD simulations. During the testing of our configurations I tested much bigger size systems without having more accurate results but only high increase of computational cost.

All the potentials for my simulations are well known empirical anharmonic interatomic potentials, described in previous section (4.1.1). For each

material the potential type is cited in table 1 in the Potential column. In order to reduce the computational cost I tested the cut-off parameters in order to produce accurate results without including calculations at large distances.

6.4.2 Methodology

The procedure I followed for the preparation of the systems in order to calculate the various properties is the same as the procedure described in section 4.1.2. As previously, for the calculation of heat capacity the materials need to be treated as bulk in order to avoid possible problems in MD simulations such as having surface interactions or anisotropic volume expansion, so I use PBC. Also the most common approach for the calculation of C_{V}, is to use the microcanonical NVE in which the volume and the energy of the system are constant and the temperature and the pressure are allowed to change.

For the calculation of heat capacity I run simulations for a wide temperature range, in order to cover the whole solid phase. The temperature range for most of the materials was from 1 K till around 4,000 K, a temperature that all used materials are in liquid state, and the temperature step was varying from 1 K to 4 K, without any difference in the fitting procedure later on. For the calculation of C_{V} I run simulations of the equilibrated system in NVE ensemble for 15 ps at every different temperature. For the calculation of the volume I run simulations of the equilibrated system in NPT Berendsen ensemble for 15 ps for every different temperature. For both NVE and NPT ensembles I used the same initial configuration, the same interatomic potential and the same simulation parameters, but I followed different procedure for the calculation of α.

Under constant pressure conditions, the coefficient of thermal expansion was calculated by using the direct equation

$$\alpha = \frac{1}{V_0}\frac{\Delta V}{\Delta T} \tag{6.29}$$

where V_0 is the system's volume at the lowest temperature and ΔV and ΔT is the volume and temperature difference, respectively, over all simulations for

each material. Under constant volume conditions, the coefficient of thermal expansion was calculated by using the equation 6.18. For higher accuracy of the results I calculated the value of α at each different temperature and I used the average value to compare with α from simulations under constant pressure conditions. C_{V} was calculated through the definition of heat capacity, by deriving the energy of the system with respect to temperature per atom. I used various fitting methods, such as polynomial fitting of various orders and cubic splines, in order to optimise and obtain the most accurate results and verify that C_{V} is not sensitive to the polynomial order and the fitting parameters.

6.4.3 Results

As I mentioned the calculation of heat capacity was done at a wide temperature range in order to include the whole solid phase of every system, with exception the viscous liquid case. The results I present in figures 41, 42, 43, 44, 45 and 46 I refer only to the solid phase, likewise for the calculation of the coefficient of thermal expansion. The left graphs represent the volume over the initial volume at the lowest temperature in respect with temperature. All results were directly extracted from NPT simulations where pressure and temperature in the system are kept constant. As we can see, all systems exhibit a linear increase in volume as temperature increases.

The right graphs represent the heat capacity under constant volume over the number of atoms in the system and over Boltzman's constant in respect with temperature. All results are fitted energy data over temperature. From these graphs we observe that for all different systems C_{V} increases above the classical Dulong−Petit value of 3 as temperature increases. Although C_{V} is expected to exhibit a linear increase we can see that for all materials the curve is not straight. This is something that is attributed to the initial fitting process of the data. In figure 47 I present a summary of the data for V/V_0 and C_{V} in respect with temperature for all solid systems I used.

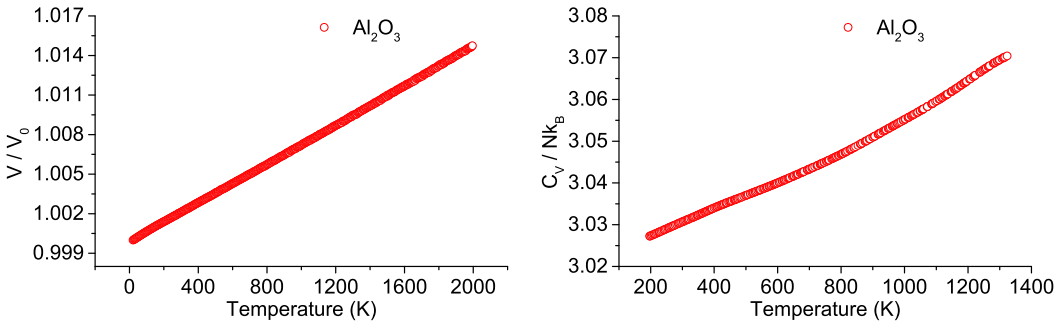

Figure 41: Al_2O_3. Left graph: Volume over V_0 as a function of temperature. Right graph: C_V as a function of temperature.

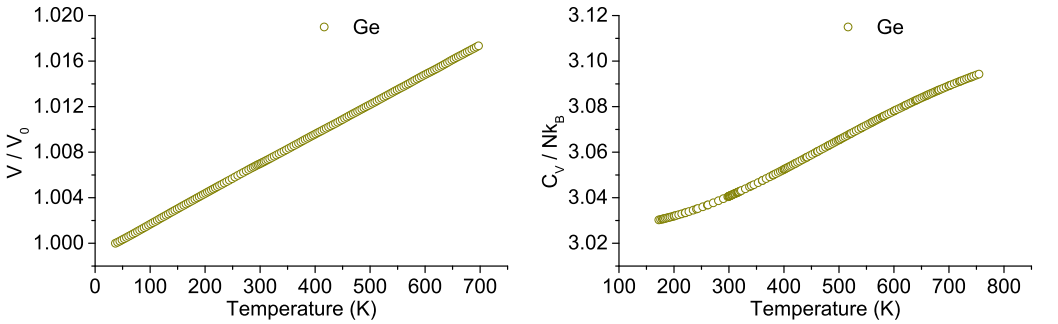

Figure 42: Ge. Left graph: Volume over V_0 as a function of temperature. Right graph: C_V as a function of temperature.

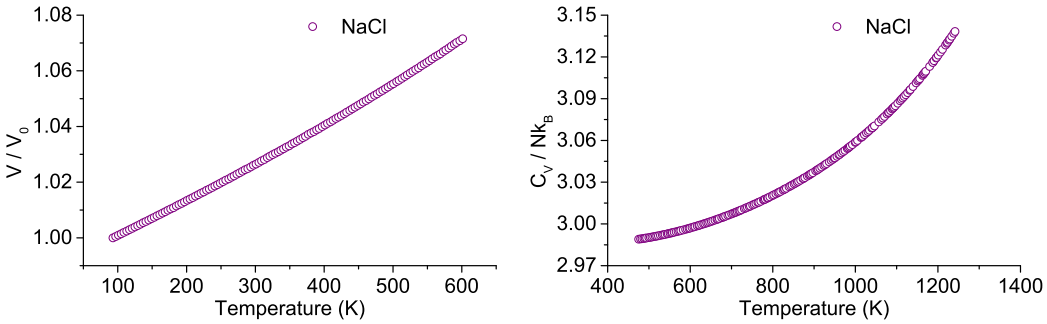

Figure 43: NaCl. Left graph: Volume over V_0 as a function of temperature. Right graph: C_V as a function of temperature.

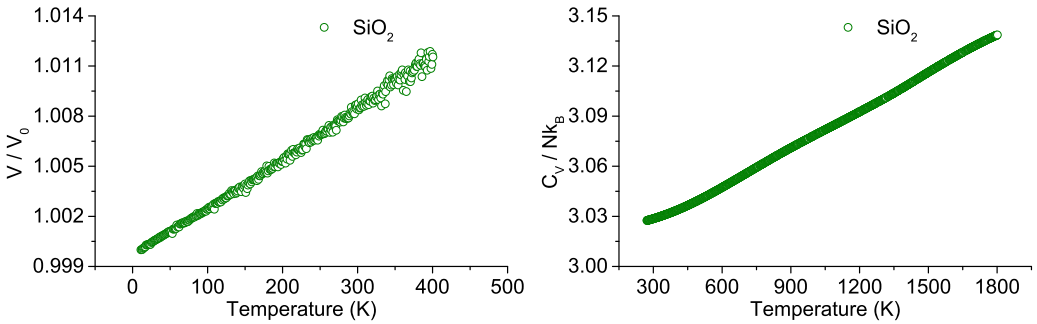

Figure 44: SiO_2. Left graph: Volume over V_0 as a function of temperature. Right graph: C_V as a function of temperature.

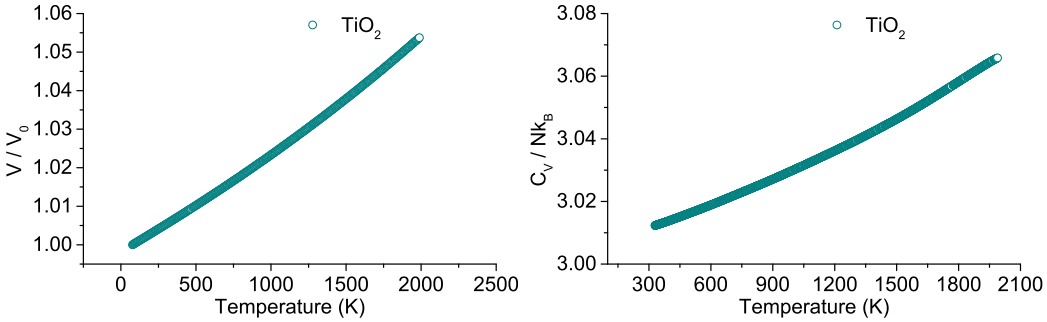

Figure 45: TiO_2. Left graph: Volume over V_0 as a function of temperature. Right graph: C_V as a function of temperature.

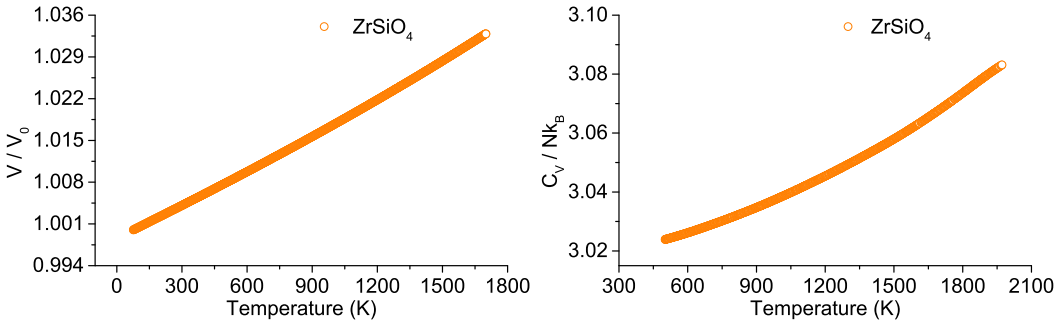

Figure 46: $ZrSiO_4$. Left graph: Volume over V_0 as a function of temperature. Right graph: C_V as a function of temperature.

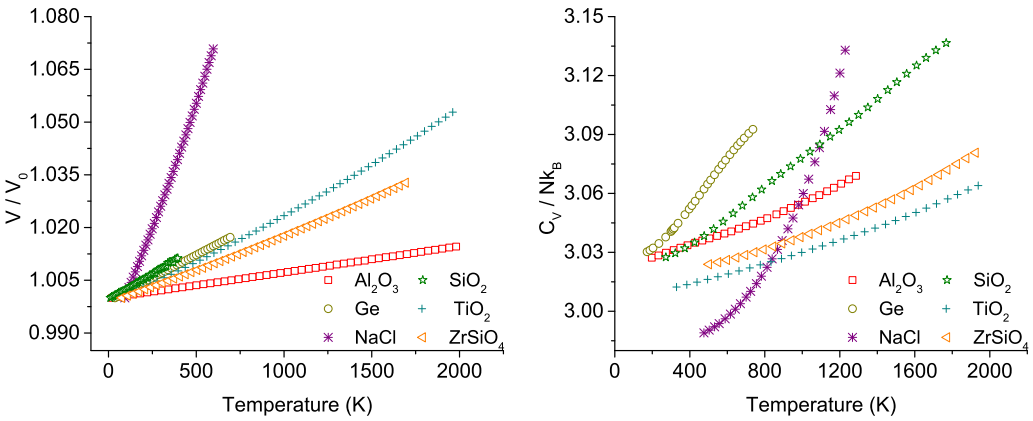

Figure 47: The 6 materials in solid phase. Left graph: Volume over V_0 as a function of temperature. Right graph: C_V as a function of temperature.

A major exception can be seen for the crystalline Argon case in figure 48, where the increase of C_{V} is preceded by its decrease at low temperature. Although Argon is a very simple element is characterised as a soft crystal. Such crystals tend to be soft and have low melting points because the atoms in the solid experience relatively weak interatomic attractions. Soft crystals that contain only individual atoms, as in crystalline Argon, include only weak London forces between their atoms. These crystals are characterised by large anharmonicity and have high Grüneisen parameter, ($\gamma = 2.9$ for Argon [212]). This is a drawback of the theory which is based on assumptions of the Grüneisen approximation, so I did not involve crystalline Argon in the calculations of the coefficient of thermal expansion. Nevertheless, this drawback is not a problem for most other crystals that have lower γ [213,214].

In the methodology section I mentioned that coefficient of thermal expansion is calculated for the solid phase, something that is represented as a linear part in the figures of heat capacity. For the special case of viscous liquid, in figure 49, α is calculated at low temperatures where C_{V} exhibits a linear increase. As with the other materials I calculated α at each temperature and I used the average value to compare with α from simulations under constant pressure.

To separate the α calculated from equation 6.29 and the α calculated from

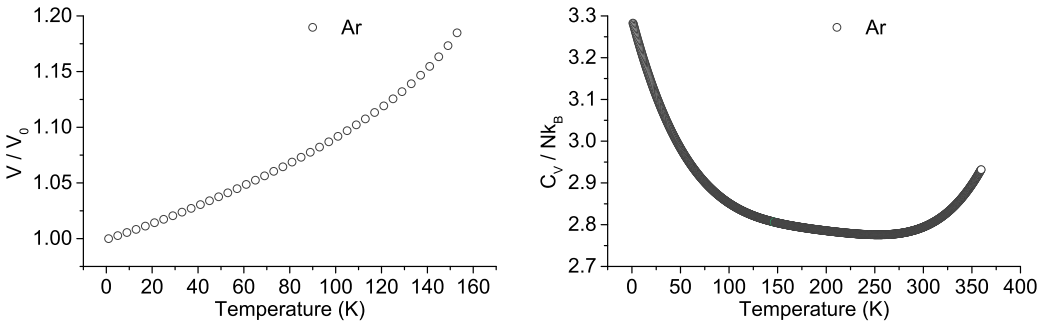

Figure 48: Argon fcc. Left graph: Volume over V_0 as a function of temperature. Right graph: C_V as a function of temperature.

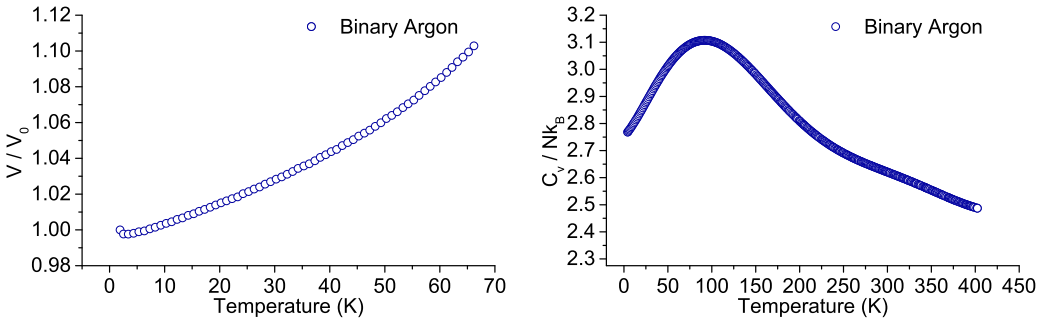

Figure 49: Binary Argon. Left graph: Volume over V_0 as a function of temperature. Right graph: C_V as a function of temperature.

the equation 6.18, I will name the first one as coefficient of thermal expansion calculated under NPT Berendsen ensemble (α_{NPT}) and the second coefficient of thermal expansion calculated under NVE ensemble (α_{NVE}). In the table 2 I show the values of α_{NPT} and α_{NVE} for each system and the difference between these two values. The values of α_{NPT} and α_{NVE} may deviate from the experimental values, something that I do not examine in the present research. This is a known result that occurs in computational simulations and arises from the use of small systems, comparing to real samples, and the use of empirical interatomic potentials. The validity of the theory is based on calculations from different simulations which use the same potential. Although interatomic potentials not necessarily reproduce results close to experimental values for α, they are developed to reproduce accurately other physical properties such as phonon frequencies, in which the equation 6.18

Table 2: Coefficient of thermal expansion values for various materials. Results from MD simulations

Material	$\alpha_{NPT}(10^{-5}\mathrm{K}^{-1})$	$\alpha_{NVE}(10^{-5}\mathrm{K}^{-1})$	$\frac{\lvert\alpha_{NPT}-\alpha_{NVE}\rvert}{\alpha_{NPT}}\%$
Al_2O_3	0.7	1.3	85.7
Ar (liquid)	172.0	175.0	1.7
Ge	2.6	3.6	38.5
NaCl	14.0	7.0	50.0
SiO_2	2.9	2.4	17.2
TiO_2	2.8	1.1	60.7
$ZrSiO_4$	2.0	1.3	35.0

is based on, they still give correct order of magnitude calculations. This is understood from the average percentage difference of $|\alpha_{NPT}-\alpha_{NVE}|/\alpha_{NPT}\%$ for all the systems, which is 41.2% and it provides correct order of magnitude estimation.

As a conclusion, the equation 6.18 gives the correct order of magnitude evaluation of anharmonic effects for all tested materials and structures, a result that is considered the best of what can be achieved using the traditional perturbation expansion approximations. This equation works well enough for crystals but it works particularly well for glasses and liquids, although it is an equation that approaches liquids from the solid phase. In the next paragraphs I am going to explain why the (6.18) can be used for liquids and the existence of a non-monotonic behaviour for the viscous liquid case in C_V.

6.4.4 Discussion of the liquid C_V

The material I chose to represent the liquid state is a binary Argon material that uses a Lennard−Jones potential to describe the interatomic interactions. As I present in figure 49 the C_V at low temperature has an almost linear increase. The calculated α_{NVE} comes from the first part of C_V, the linearly increasing part which corresponds to a viscous liquid and not to a solid.

A general definition of a viscous liquid is a liquid whose relaxation time (τ)

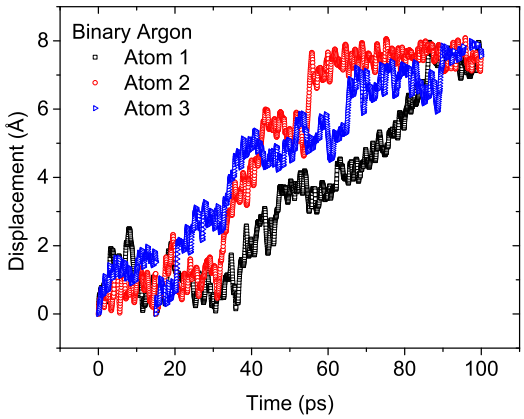

Figure 50: Atomic displacement over 100ps simulation period for 3 atoms of binary Argon.

is much larger than the Debye vibration period which is around 0.1 ps, so $\tau \gg \tau_{\mathrm{D}}$. Relaxation time is defined as the average time between consecutive atomic jumps in a liquid at one point in space [193]. To show that $\tau \gg \tau_{\mathrm{D}}$, in figure 50 I plot the coordinates of three atoms with the highest displacement form their initial position, taken from the simulation of the viscous liquid at 50 K. This temperature corresponds to the temperature in the middle of the linear increase of C_{V} for Argon.

From the graph I can conclude that the atomic displacements are much higher than the Debye vibration period or typical displacement for solids, and reach 8 Å over the whole simulation time of 100 ps. As it can be seen, the large-amplitude diffusive motions are present, something that indicates that the system is in the liquid state. According to Lindemann criterion [215] the melting might be expected when the root mean vibration amplitude $\sqrt{< u^2 >}$ exceeds a certain threshold value, which namely is when the amplitude reaches at least 10% of the nearest neighbour distance. This is obvious from figure 50. The Lindemann criterion was originally explaining the mechanism of melting for bulk materials with simple structure by using the vibration of atoms in the crystal to explain the melting transition. This method has been proved to work well with crystals described by the Lennard−Jones potential [216]. Moreover from the calculation of τ as the average time be-

tween atomic jumps, the relaxation time is $\tau \approx 15$ ps and I can conclude that this systems corresponds to a viscous liquid.

As it might be argued, the equation 6.18 is derived for solids so it can not be applied for liquids. In a liquid there are two types of motion, the diffusional motion and the phonon motion [193]. The phonon motion includes one longitudinal mode and two transverse modes with frequency $\omega > \frac{1}{\tau}$. Liquid energy is the sum of the diffusional energy with phonon energy, where the diffusional energy includes the kinetic and potential energy of the atoms. The time that an atom spends to move from one position to another is approximately equal to τ_{D} [193]. Therefore, the probability of a jump is $\rho = \tau_{\mathrm{D}}/\tau$.

In statistical equilibrium, the number of atoms in the transitory diffusing state is $N_{dif} = N\rho$, where N is the total number of atoms, which is equal to

$$N_{dif} = N\frac{\tau_{\mathrm{D}}}{\tau} \tag{6.30}$$

From the equation 6.30 it is clear the relative number of diffusing atoms at any given moment of time is negligible since for the viscous liquid it is true that $\tau \gg \tau_{\mathrm{D}}$.

As a consequence, the diffusional energy of the liquid in this regime can be neglected and the total liquid energy is equal to the phonon energy. The phonon energy of a liquid for time τ is given, to a very good approximation, by the phonon energy of its solid. This approximation is verified if I calculate the energy of a liquid from the anharmonic liquid energy equation proposed in [150], where the authors approach liquids from the solid state

$$E = NT\left(1 + \frac{\alpha T}{2}\right)\left[3 - \left(\frac{\tau_{\mathrm{D}}}{\tau}\right)^3\right] \tag{6.31}$$

where for the case of viscous liquid where $\tau \gg \tau_{\mathrm{D}}$, the equation 6.31 gives $E = 3NT\,(1 + \alpha T/2)$ and consequently $C_V = 3N(1 + \alpha T)$. The only difference between the phonon states in a liquid and a solid is that the liquid does not support all transverse modes as a solid does, but only modes with frequency $\omega > 1/\tau$ as it was mentioned earlier, something that for the viscous liquid

case gives a minor affect to the phonon energy.

By using the previous approximations I can say the energy of the viscous liquid is similar to the solid phonon energy. Thus, equation 6.18 is applicable to viscous liquids. This explains the non-monotonic behaviour of C_V which for low temperature, where the viscous regime is, the C_V increases. After the linear increase, the C_V reaches a maximum and then it decreases. This behaviour can be explained as a result of two competing effects. The C_V increases for low temperature due to anharmonicity and then C_V decreases at high temperature as a result of the number of transverse waves progressively decreasing with the frequency.

Extensive studies of anharmonicity in oxides and silicates report a systematically positive anharmonic contribution to C_V [217–222]. This decrease of C_V is a common effect and it is observed in experimental data for many liquids [149, 150, 192]. These two effects give the maximum of C_V, something that experimentally is difficult to be observed.

The experimental observation of the decrease of C_V, requires experiments where τ approaches τ_D. That could be achieved by using low viscosity liquids such as metallic, noble atom and some molecular liquids [149]. The problem with these liquids is that they tend to crystallise easily on cooling, preventing the formation of the viscous regime. Moreover, a linear increase of C_V could be observed in viscous liquids such as silicates, chalcogenides and other systems, but reaching a low viscosity regime in these systems and observe the decrease of C_V due to the loss of transverse waves, requires high temperature, where experiments are challenging.

Furthermore, viscous liquids often have strong bonds and high Debye temperature for internal vibrations. As a result the heat capacity continues to increase even at high temperature due to progressive excitation of internal vibrations, counteracting the decrease of C_V due to the loss of transverse modes. That makes experiments not able to observe the non-monotonic behaviour of C_V but able only to observe either a decrease of C_V in low viscosity liquids or an increase of C_V in high viscosity liquids.

6.5 Summary and discussion

From literature it is clear that a universal theory that calculates the heat capacity for all states of matter is absent. Theories of calculation of heat capacity focus on solids and gases while they approach liquids either from the gas phase or the solid phase. For the calculation of heat capacity I used a theory that approaches the liquids from the solid phase and it can calculate the heat capacity by using the equation 6.18. Using this equation provides a simple new way to evaluate the effect of anharmonicity on a system's thermodynamic functions, such as heat capacity. In this approach, the contribution of all potentially complicated anharmonic effects to C_{V} is evaluated using one parameter only, the coefficient of thermal expansion.

From the equation 6.18 I estimated the effect of anharmonicity in heat capacity, by comparing results of the coefficient of thermal expansion under constant volume conditions and under constant pressure conditions, by performing extensive classical MD simulations. These simulations are not affected from anharmonic effects since they treat materials as classic and at the same time allow to study a wide temperature range under various conditions, something that is not easily approached by experiments. The results of α from MD simulations under different conditions, show that the equation 6.18 provides a correct order of magnitude evaluation of anharmonic effects and they are considered to be better from what the traditional approach of perturbation expansion can give.

For the viscous liquid case, the heat capacity forms a non-monotonic behaviour, with a linear increase at low temperature, a maximum and then a linear decrease at high temperature, something that can not be observed experimentally. This phenomenon is a result of two competing effects. One is at the high-viscous regime at low temperatures where C_{V} increases due to high anharmonicity and second is at the low-viscous regime at high temperatures where C_{V} decreases due to decrease of transverse waves with frequency. Overall this theory has a good predictive power for systems of any complexity or structure.

7 Summary and conclusions

In previous chapters I try to explain and define the main objective of this thesis, the connection of dynamics in the solid and liquid state. Information on the structure and dynamics of a material help to predict its properties and its behaviour. The problem that still remains nowadays is the absence of a universal theory that describes dynamics of materials in all structural phases. Most of the current theories focus on crystals and they use various approximations to discuss amorphous and liquid materials. For this reason the understanding of the correlation of dynamics between the three phases of a material is very important.

In chapter 2 I provide the general theory that applies to the procedure and analysis I follow in the rest of the chapters. I discuss the structural properties of crystalline, amorphous and liquid materials and I give a brief description of the similarities and distinctions of the three phases. I define basic terms related to structure and structure analysis. Thereafter I discuss atomic dynamics of materials and the current theories and current approximations that are being used to describe dynamics in a system. This introduction is essential for better understanding of the results of next chapters.

Moreover I focus on the neutron scattering technique. I discuss the benefits of this technique and I explain the procedure during elastic and inelastic scattering. The neutron scattering technique is the major technique I use for experiments and simulations in order to study the collective excitation spectra and the phonon−roton minimum for barium and other materials.

In chapter 3 I describe the inelastic neutron scattering experiments I performed with barium. The results I present are for barium in the polycrystalline and liquid phase. These results include collective excitation spectra and DHO fits of phonon frequencies of barium at various temperatures. The DHO fits represent an average curve of all dispersion curves along the wave vector in the collective excitation spectra and provide a better understanding of the phonon frequencies of the system. I evaluate the fits by studying the damping factor of every fit and by comparing them with the initial data, showing the good quality of the fitting procedure.

The results from INS experiments show high similarity of the collective excitation spectra of the polycrystalline and liquid phase of barium. This is also observed in the DHO fit graphs of both phases. Furthermore I discuss the phonon−roton minimum regime of barium that can be observed in the results, something that I compare later with results from INS simulations and theoretical calculations.

In chapter 4 I present the computational work of this thesis and the principles of classical molecular dynamics simulations and how I calculate phonon frequencies. I calculate phonon frequencies for iron and argon in their crystalline and amorphous phase and I perform similar analysis as in the experimental method. I present collective excitation spectra and DHO fits for iron and argon showing similar results as in the experiments. Both crystalline and amorphous phase exhibit similar phonon frequencies and they exhibit the phonon−roton minimum at similar wave vector. Results from DHO experiments and simulations verify the connection of dynamics of solids and the corresponding liquids.

In chapters 3 and 4 I present results from INS calculations for both solid and liquid phases. As we can see from the collective excitation spectra and the DHO fits, the solid and the corresponding liquid structure exhibit remarkable similarities. The spectra of the solid and liquid follow the same pattern and they exhibit the characteristic regimes of phonon−maxon and phonon−roton at the same wave vector. From this observation in my results and also in results in literature, I can conclude that the high-frequency atomic dynamics of a solid are very similar to dynamics of the corresponding liquid.

Moreover in chapter 4 I present a detailed analysis of the local structure of many materials in their crystalline, amorphous and liquid phase. I compare results from the pair distribution function analysis and the angles between nearest neighbour atoms analysis in the three phases. Results from the three phases show that the population of the local structure remains the same regardless of the structure. The results for the amorphous and liquid phase of most materials exhibit similar angles between the bonds as those of the crystalline phase, implying similar local order in the three phases. From the

similarities of the three phases in results from both local population and local order analysis I can conclude that the short-range structure of any state of the system remains the same, or very similar, to this of the crystalline state. This is something already discussed in literature but it has not studied extensively.

At the end of chapter 4 I describe the method to produce accurate interatomic potential parameters for barium with the use of DFT calculations. The modelled potential for barium is in the extended Finnis−Sinclair form and I use the force-matching method to obtain the parameters. I perform extensive fitting calculations in order to calculate the 9 parameters of the potential but without obtaining results that describe accurately the physical properties of the system. From the angle analysis of barium, based on the results from angle analysis in other systems, I explain that the structure is not the predicted one and I identify this as the main reason for not producing potential parameters that describe accurately barium's physical properties.

In chapter 5 I focus on interatomic interactions and the origin of the phonon−roton minimum. I revise the theoretical background of the roton minimum and the proposed theories of its origin, based on superfluid helium. I propose a theory that uses as a starting point the hypothesis that the formation of the phonon−roton minimum is a result of atomic interactions and not a quantum phenomenon.

I use as study system a monatomic bcc material in order to explain the interatomic interactions in the short-range order. This theory explains that the local atomic interactions are the strongest in the system and they highly affect it. For the specific case I predict that the formation of the phonon−roton minimum is related to the nearest interatomic interactions of the third parallel neighbour plane of atoms in the longitudinal acoustic mode. I compare the theoretical results with results from INS experiments and simulations and I find that this theory has very good predictive power.

Although the theory is based on a crystalline system, it can extend to amorphous and liquid systems. This is clear from results in chapter 4 where I exhibit the local structure similarities of the three phases. Moreover, this theory can be extended to more complicated structures and it is expected to predict the origin of the phonon−roton minimum. Still this needs to be

verified by further calculations.

As I explain in chapter 5 the sort-range interactions in a crystal are very strong and they highly affect the local structure. These interactions highly constrain the atoms to form a specific structure. This is possibly the mechanism that impels the amorphous and liquid state to form structure similar to this of the corresponding crystalline structure. Moreover, the strong short-range interactions highly affect the dynamics of the system. This can be understood from the formation of the phonon−roton minimum at the same wave vector were the strongest interatomic interaction of the system minimise. Therefore the local structure of a system affects its dynamics, regardless of the state of the system.

In chapter 6 I extend the connection of solids and liquids to the macroscopic level by studying thermodynamical properties of various simple materials. I revise existed theories on the prediction of heat capacity of solids and liquids and I propose a new simple way to calculate heat capacity. This new theory calculates the heat capacity by using the coefficient of thermal expansion.

I perform classical MD simulations in order to calculate the heat capacity of various crystalline and amorphous materials. I test the validity of the theory by calculating the coefficient of thermal expansion under constant pressure conditions and under constant volume conditions. This theory has a good predictive power and it gives correct order of magnitude evaluation of the anharmonic effects in a material.

Moreover I test the theory for a viscous liquid system and it also provides good predictive power, as for solids. For this system the heat capacity exhibits a non-monotonic behaviour, with an initial linear increase at low temperature and then an almost linear decrease at higher temperature. This is due to two contradicting effects, initial increase due to high anharmonicity and then decrease due to the decreasing number of transverse waves. The good predictive power of the anharmonicity of a system applies to all tested cases including crystalline, amorphous and liquid simple materials. Since the theory functions well regardless the state of the system, we can assume that similar anharmonic effects apply to both solids and liquids.

Overall I can conclude that atomic dynamics of solids and the corresponding liquids are highly connected. Although I focus in details in the local-structure atomic dynamics and I prove the high similarity of dynamics of the solid and liquid phase, results from the calculation of heat capacity allude the connection of dynamics at the macroscopic level as well. Further investigation of the connection of dynamics of the two phases in more complex materials at both microscopic and macroscopic level will provide a generalised theory which will fill in the existing lack of theory predicting dynamics of liquids.

A Calculation of the angular frequency for short wave vector

For the linear chain model, which describes a one-dimensional model, the energy between two atoms is

$$E = \frac{1}{2}J(u_n - u_{n+1})^2 \tag{A.1}$$

where J is the force constant at the equilibrium position. The strain ϵ for displacement u_n of an atom n from its equilibrium position is given as $u_n = \epsilon n a$, where a is the interatomic distance. Then the energy from the strain of an atom from its equilibrium position is

$$E_{strain} = \frac{1}{2}\frac{J(u_n - u_{n+1})^2}{a} = \frac{1}{2}J\epsilon^2 a \tag{A.2}$$

From theory we know that if we include the isotropic elastic stiffness (c) the equation A.2 will be equal to

$$E_{strain} = \frac{1}{2}c\epsilon^2 \tag{A.3}$$

The relation between c and the force constant J is $c = Ja$.

Vibrations with short wave vector, or else long wavelength, correspond to acoustic waves. The relationship that connects the speed of sound v_{sound} and the c is

$$v_{\text{sound}}^2 = \frac{c}{\rho} = \frac{Ja^2}{m} \tag{A.4}$$

where ρ is the density and is equal to $\rho = m/a$

Moreover, the speed of sound is related to the angular frequency and the wave vector as $\omega = v_{\text{sound}}k$. The last equation with combination with equation A.4 defines the angular frequency for long wavelength as

$$\omega = v_{\text{sound}}k = \left(a\sqrt{\frac{J}{m}}\right)k \tag{A.5}$$

B Calculation of the angular frequency for long wave vector

The energy between an atom n and its nearest neighbour atom $n+1$ is

$$E_n = \frac{1}{2}J(u_{n+1} - u_n)^2 + \frac{1}{2}J(u_n - u_{n-1})^2 \tag{B.1}$$

From Newton's equation of motion we know that

$$F_n = -\frac{\partial E_n}{\partial u_n} = m\frac{\partial^2 u_n}{\partial t^2} \tag{B.2}$$

If we replace the equation B.1 in the equation B.2 we get

$$m\frac{\partial^2 u_n}{\partial t^2} = -J(2u_n - u_{n+1} - u_{n-1}) \tag{B.3}$$

The solution that describes the sinusoidal acoustic waves with respect of displacement is

$$u_{n,k} = U_k \exp[i(kx_n - \omega t)] \tag{B.4}$$

where U_k is the amplitude of the displacement along the wave vector with frequency ω. x_n is the position of the n-th atom and is defined as $x_n = na$, where for this case where we calculate distances between the nearest neighoubor atoms a is the interatomic distance. The general form of the equation B.4 including the displacement of all atoms in a system is

$$u_{n,k} = \sum_k U_k \exp[i(kna - \omega t)] \tag{B.5}$$

When describing only the nearest neighbour interactions for a monatomic linear system, the equation B.4 is simplified to

$$u_{n+1,k} = u_n \exp(ika) \tag{B.6}$$

If we use equation B.6 to solve equation B.2 we get

$$\begin{aligned} m\frac{\partial^2 u_n}{\partial t^2} &= -J(2u_n - u_{n+1} - u_{n-1}) \\ &= -Ju_n[2 - \exp(ika) - \exp(-ika)] \\ &= -2Ju_n[1 - \cos(ka)] \\ &= -4Ju_n \sin^2\left(\frac{ka}{2}\right) \end{aligned} \tag{B.7}$$

In order to include the angular frequency in our calculations we equate the mass times acceleration with mass times angular frequency squared times the displacement

$$m\frac{\partial^2 u_n}{\partial t^2} = -m\omega_k^2 u_n \tag{B.8}$$

Thus we can calculate the angular frequency for interactions between neighbour atoms as

$$\begin{aligned} \omega_k^2 &= \left(\frac{4J}{m}\right)\sin^2\left(\frac{ka}{2}\right) \\ \omega_k &= \sqrt{\frac{4J}{m}}\left|\sin\left(\frac{ka}{2}\right)\right| \end{aligned} \tag{B.9}$$

In order to calculate the angular frequency for the general case where we calculate all the interactions in the system and not only the nearest neighbour interactions, the equation B.1 will change to

$$E = N\sum_p \phi_p(pa) + \frac{1}{2}\sum_{n,p} J_p(u_n - u_{n+p})^2 \tag{B.10}$$

where $\phi_p(r_p)$ is the energy between the n-th atom and its p-th neighbour, which are in a distance $r_p = pa$. The force constant J_p between the n-th atom and its p-th neighbour is defined as

$$J_p = \frac{\partial^2 \phi_p}{\partial r_p^2} \tag{B.11}$$

Similar to equation B.3 and by including the equation B.6 but not for the

nearest neighbour atom but for a neighbour atom p, the general solution is

$$\begin{aligned} m\frac{\partial^2 u_n}{\partial t^2} &= -\sum_p J(2u_n - u_{n+p} - u_{n-p}) \\ &= u_n \sum_p J_p[2 - \exp(ikpa) - \exp(-ikpa)] \end{aligned} \tag{B.12}$$

As previously, by using equation B.8 we can calculate the general angular frequency for a system as

$$\begin{aligned} \omega_k^2 &= \sum_p \frac{4}{m} J_p \sin^2\left(\frac{kpa}{2}\right) \\ \omega_k &= \sum_p \sqrt{\frac{4}{m} J_p \sin^2\left(\frac{kpa}{2}\right)} \end{aligned} \tag{B.13}$$

This solution refers to monatomic systems. Systems of more than one different atoms require different equation for every different atom and the solution of these equations become very complicated to be solved by hand.

References

[1] V. M. Giordano and G. Monaco. Fingerprints of order and disorder on the high-frequency dynamics of liquids. *PNAS*, 107(51):21985 – 21989, 2010.

[2] L. D. Landau. On the theory of superfluidity of Helium II. *Journal of Physics*, XI(1):91 – 92, 1947.

[3] R. P. Feynman. Atomic theory of the two-fluid model of liquid helium. *Phys. Rev.*, 94:262 – 277, Apr 1954.

[4] T. Scopigno, G. Ruocco, and F. Sette. Microscopic dynamics in liquid metals: The experimental point of view. *Rev. Mod. Phys.*, 77:881 – 933, 2005.

[5] `http://www.isis.stfc.ac.uk`.

[6] K. Trachenko and V. V. Brazhkin. Heat capacity at the glass transition. *Phys. Rev. B*, 83:014201, Jan 2011.

[7] N. H. March. *Liquid metals*. Pergamon Press, 1968.

[8] S. R. Elliott. *Physics of amorphous materials*. Longman, 1990.

[9] M. T. Dove. *Structure and Dynamics: An atomic view of materials*. Oxford University Press, 2003.

[10] G. Tammann. *Der Glaszustand*, page 123. L. Voss, Leipzig, 1933.

[11] H. Rawson. *Glasses and their applications*, page 449. Royal institute of metals, London, 1991.

[12] A. Feltz. *Amorphous inorganic materials and glasses*, page 446. Weinheim / VCH Publishers, New York, 1993.

[13] S. R. Elliott. *Defects and disorder in crystalline and amorphous solids*, volume 418 of *C*, chapter 4, pages 73 – 86. Springer Netherlands, 1994.

[14] I. Gutzow and J. Schmelzer. *The vitreous state: thermodynamics, structure, rheology, and crystallization*, page 468. Springer-Verlag, Berlin, 1995.

[15] H. G. Pfaender. *Schott guide to glass*, page 207. Chapman & Hall, London, 2^{nd} edition, 1996.

[16] C. A. Angell. Formation of glasses from liquids and biopolymers. *Science*, 267(5206):1924–1935, 1995.

[17] J. C. Dyre. *Colloquium* : The glass transition and elastic models of glass-forming liquids. *Rev. Mod. Phys.*, 78:953–972, Sep 2006.

[18] J. C. Dyre, T. Hechsher, and K. Niss. A brief critique of the Adam–Gibbs entropy model. *Journal of Non-Crystalline Solids*, 355(10–12):624 – 627, 2009.

[19] A. A. Maradudin, I. M. Lifshitz, A. M. Kosevich, W. Cochran, and M. J. P. Musgrave. *Lattice dynamics*. W. A. Benjamic, New York, 1969.

[20] M. T. Dove. *Introduction to lattice dynamics*. Cambridge University Press, 1993.

[21] A. T. Petit and P. L. Dulong. Recherches sur quelques points importants de la theorie de la chaleur. *Annales de Chimie et de Physique*, 10:395–413, 1819.

[22] A. A. Maradudin, E. W. Montroll, G. H. Weiss, and I. P. Ipatova. *Theory of lattice dynamics in the harmonic approximation*. Academic press, 2^{nd} edition, 1971.

[23] B. Donovan and J. F. Angress. *Lattice vibrations*, volume 3. Chapman & Hall, London, 1971.

[24] M. Born and K. Huang. *Dynamical theory of crystal lattices*. Clarendon Press - Oxford, 1954.

[25] J. M. Ziman. *Electrons and phonons*. Clarendon Press, Oxford, 1960.

[26] L. D. Landau and E. M. Lifshitz. *Statistical Physics: Course of Theoretical Physics*, volume 5, page 150. Pergamon Press, 3rd edition, 1980.

[27] M. T. Dove. *Structure and Dynamics: An atomic view of materials*, page 191. Oxford University Press, 2003.

[28] M. Vasileiadis. *Calculation of the free energy of crystalline solids*. PhD thesis, Imperial College London, 2013.

[29] F. Sette, M. H. Krisch, C. Masciovecchio, G. Ruocco, and G. Monaco. Dynamics of glasses and glass-forming liquids studied by inelastic x-ray scattering. *Science*, 280(5369):1550–1555, 1998.

[30] J. M. Ziman. *Models of disorder*. Cambridge University Press, 1979.

[31] K. Huang. *Statistical mechanics*. John Wiley & Sons, 1987.

[32] V. N. Novikov and N. V. Surovtsev. Spatial structure of boson peak vibrations in glasses. *Phys. Rev. B*, 59:38–41, Jan 1999.

[33] G. Squires. *Introduction to the theory of thermal neutron scattering*. Cambridge University Press, Cambridge, 1978.

[34] S. W. Lovesey. *Theory of neutron scattering from condensed matter*. Clarendon Press, Oxford, 1984.

[35] M. Bee. *Quasielastic neutron scattering: Principles and applications in solid state chemistry, biology and materials science*, chapter 2. Hilger, Bristol, 1988.

[36] M. T. Dove. *Introduction to lattice dynamics*, chapter 9. Cambridge University Press, 1993.

[37] D. S. Sivia. *Elementary scattering theory*. Oxford University Press, Oxford, 2011.

[38] J. Bosse, W. Götze, and M. Lücke. Mode-coupling theory of simple classical liquids. *Phys. Rev. A*, 17(1):434–446, 1978.

[39] F. Hensel and W.W. Warren. *Fluid Metals: The Liquid-Vapor Transition of Metals*, chapter 3. Princeton Legacy Library. Princeton University Press, 2014.

[40] B. Fȧk and B. Dorner. Phonon line shapes and excitation energies. *Physica B: Condensed Matter*, 234–236:1107 – 1108, 1997. Proceedings of the First European Conference on Neutron Scattering.

[41] S. M. Shapiro, J. D. Axe, G. Shirane, and T. Riste. Critical neutron scattering in $SrTiO_3$ and $KMnF_3$. *Phys. Rev. B*, 6:4332–4341, 1972.

[42] F. Sette, G. Ruocco, M. Krisch, U. Bergmann, C. Masciovecchio, V. Mazzacurati, G. Signorelli, and R. Verbeni. Collective dynamics in water by high energy resolution inelastic x-ray scattering. *Phys. Rev. Lett.*, 75:850–853, 1995.

[43] C. R. Anderson, K. H. Andersen, J. Bossy, W. G. Stirling, R. M. Dimeo, P. E. Sokol, J. C. Cook, and D. W. Brown. High-resolution neutron-scattering study of the roton in confined superfluid ^{4}He. *Phys. Rev. B*, 59:13588–13591, 1999.

[44] F. Hippert. *Neutron and X-ray Spectroscopy*. Grenoble sciences. Springer, New York, 2006.

[45] T. Ichitsubo, S. Hosokawa, K. Matsuda, E. Matsubara, N. Nishiyama, S. Tsutsui, and A. Q. R. Baron. Nanoscale elastic inhomogeneity of a pd-based metallic glass: Sound velocity from ultrasonic and inelastic x-ray scattering experiments. *Phys. Rev. B*, 76:140201, 2007.

[46] S.W. Lovesey. *Condensed matter physics: dynamic correlations*. Frontiers in physics. Benjamin/Cummings, 1986.

[47] Ubaldo Bafile, Eleonora Guarini, and Fabrizio Barocchi. Collective acoustic modes as renormalized damped oscillators: Unified description

of neutron and x-ray scattering data from classical fluids. *Phys. Rev. E*, 73:061203, 2006.

[48] A. O. E. Animalu. Electronic theory of phase transitions in Ca, Sr, and Ba under pressure. *Phys. Rev.*, 161:445–455, Sep 1967.

[49] V. Heine and I. Abarenkov. A new method for the electronic structure of metals. *Philosophical Magazine*, 9(99):451–465, 1964.

[50] W. B. Pearson. *Handbook of lattice spacings and structures of metals*. Pergamon Press, New York, 1967.

[51] J. A. Moriarty. Localized d states for pseudopotential calculations: Application to the alkaline-earth metals. *Phys. Rev. B*, 6:4445–4458, 1972.

[52] W. A. Harrison. Transition-metal pseudopotentials. *Phys. Rev.*, 181:1036–1053, 1969.

[53] J. A. Moriarty. Pseudo green's functions and the pseudopotential theory of d-band metals. *Phys. Rev. B*, 5:2066–2081, 1972.

[54] K. S. Sharma. Phonon dispersion in barium. *physica status solidi (b)*, 108(2):K101–K104, 1981.

[55] K.S. Sharma and C.M. Kachhava. A linear potential and phonons in sodium. *Solid State Communications*, 30(11):749 – 753, 1979.

[56] U. Buchenau, M. Heiroth, H. R. Schober, J. Evers, and G. Oehlinger. Lattice dynamics of strontium and barium. *Phys. Rev. B*, 30:3502–3505, 1984.

[57] J. A. Moriarty. First-principles phonon spectra in Ca and Sr. *Phys. Rev. B*, 28:4818–4821, 1983.

[58] J. Mizuki, Y. Chen, K.-M. Ho, and C. Stassis. Phonon dispersion curves of bcc Ba. *Phys. Rev. B*, 32:666–670, 1985.

[59] A. D. B. Woods, B. N. Brockhouse, R. H. March, A. T. Stewart, and R. Bowers. Crystal dynamics of sodium at 90k. *Phys. Rev.*, 128:1112–1120, 1962.

[60] R. A. Cowley, A. D. B. Woods, and G. Dolling. Crystal dynamics of potassium. i. pseudopotential analysis of phonon dispersion curves at 9k. *Phys. Rev.*, 150:487–494, 1966.

[61] V. J. Minkiewicz, G. Shirane, and R. Nathans. Phonon dispersion relation for iron. *Phys. Rev.*, 162:528–531, 1967.

[62] R. Colella and B. W. Batterman. X-ray determination of phonon dispersion in vanadium. *Phys. Rev. B*, 1:3913–3921, 1970.

[63] B. M . Powell and G. Dolling. *Rare gas solids*, volume II, chapter 15. Academic Press, London, 1977.

[64] C. Stassis, C. K. Loong, C. Theisen, and R. M. Nicklow. Lattice dynamics of fcc Yb. *Phys. Rev. B*, 26:4106–4110, 1982.

[65] C. Stassis, J. Zaretsky, D. K. Misemer, H. L. Skriver, B. N. Harmon, and R. M. Nicklow. Lattice dynamics of fcc Ca. *Phys. Rev. B*, 27:3303–3307, 1983.

[66] M. Ferconi and M. P. Tosi. Phonon dispersion curves in high-temperature solids from liquid structure factors. *EPL (Europhysics Letters)*, 14(8):797, 1991.

[67] P. N. Gajjar, B. Y. Thakore, H. K. Patel, and A. R. Jani. On phonon dispersion in alkali metals. *Acta Physica Polonica A*, 88(3):489 – 502, 1995.

[68] T. Moriya. The theory of spin fluctuations in itinerant-electron magnets. *Physica B+C*, 91:235 – 243, 1977.

[69] G G Lonzarich and L Taillefer. Effect of spin fluctuations on the magnetic equation of state of ferromagnetic or nearly ferromagnetic metals. *Journal of Physics C: Solid State Physics*, 18(22):4339, 1985.

[70] S. Klotz and M. Braden. Phonon dispersion of bcc iron to 10 GPa. *Phys. Rev. Lett.*, 85:3209–3212, 2000.

[71] A. Bosak, M. Krisch, I. Fischer, S. Huotari, and G. Monaco. Inelastic x-ray scattering from polycrystalline materials at low momentum transfer. *Phys. Rev. B*, 75:064106, 2007.

[72] L. Mauger, M. S. Lucas, J. A. Muñoz, S. J. Tracy, M. Kresch, Yuming Xiao, Paul Chow, and B. Fultz. Nonharmonic phonons in α-iron at high temperatures. *Phys. Rev. B*, 90:064303, 2014.

[73] V. Pontikis, V. Russier, and J. Wallenius. An analytic n-body potential for bcc iron. *Nuclear Instruments and Methods in Physics Research Section B: Beam Interactions with Materials and Atoms*, 255(1):37 – 40, 2007.

[74] P. A. T. Olsson. Semi-empirical atomistic study of point defect properties in {BCC} transition metals. *Computational Materials Science*, 47(1):135 – 145, 2009.

[75] B. J. Alder and T. E. Wainwright. Phase transition for a hardsphere system. *J. Chem. Phys.*, 27(1208), 1957.

[76] A. Rahman. Correlations in the motion of atoms in liquid argon. *Phys. Rev.*, 136:A405–A411, 1964.

[77] J. E. Jones. On the determination of molecular fields. *Proc. R. Soc. Lond. A.*, 106(738), 1924.

[78] R. A. Buckingham. The Classical Equation of State of Gaseous Helium, Neon and Argon. *Proceedings of the Royal Society of London. Series A, Mathematical and Physical Sciences*, 168(933):264–283, 1938.

[79] P. M. Morse. Diatomic molecules according to the wave mechanics. ii. vibrational levels. *Phys. Rev.*, 34:57–64, Jul 1929.

[80] J. Tersoff. New empirical approach for the structure and energy of covalent systems. *Phys. Rev. B*, 37:6991–7000, Apr 1988.

[81] M. S. Daw and M. I. Baskes. Embedded-atom method: Derivation and application to impurities, surfaces, and other defects in metals. *Phys. Rev. B*, 29:6443–6453, Jun 1984.

[82] S. M. Foiles, M. I. Baskes, and M. S. Daw. Embedded-atom-method functions for the fcc metals Cu, Ag, Au, Ni, Pd, Pt, and their alloys. *Phys. Rev. B*, 33:7983–7991, 1986.

[83] M. W. Finnis and J. E. Sinclair. A simple empirical n-body potential for transition metals. *Philosophical Magazine A*, 50(1):45–55, 1984.

[84] X D Dai, Y Kong, J H Li, and B X Liu. Extended finnis–sinclair potential for bcc and fcc metals and alloys. *Journal of Physics: Condensed Matter*, 18(19):4527, 2006.

[85] `http://www.ccp5.ac.uk/DL_POLY`.

[86] P. P. Ewald. Die berechnung optischer und electrostatishe gitterpotentiale. *Ann. Phys.*, 64(253 - 287), 1921.

[87] M. P. Allen and D. J. Tildesley. *Computer simulation of liquids*. Clarendon Press, 1989.

[88] C. J. Fennell and J. D. Gezelter. Is the Ewald summation still necessary? Pairwise alternatives to the accepted standard for long-range electrostatics. *The Journal of Chemical Physics*, 124(23), 2006.

[89] H. J. C. Berendsen, J. P. M. Postma, W. F. van Gunsteren, A. DiNola, and J. R. Haak. Molecular dynamics with coupling to an external bath. *The Journal of Chemical Physics*, 81(8):3684–3690, 1984.

[90] S. Nosé. A unified formulation of the constant temperature molecular dynamics methods. *The Journal of Chemical Physics*, 81(1):511–519, 1984.

[91] W. G. Hoover. Canonical dynamics: Equilibrium phase-space distributions. *Phys. Rev. A*, 31:1695–1697, Mar 1985.

[92] J. W. Gibbs. *Elementary Principles in Statistical Mechanics*. Charles Scribner's Sons, New York, 1902.

[93] W. C. Swope, H. C. Andersen, P. H. Berens, and K. R. Wilson. A computer simulation method for the calculation of equilibrium constants for the formation of physical clusters of molecules: Application to small water clusters. *The Journal of Chemical Physics*, 76(1):637–649, 1982.

[94] L. Verlet. Computer "experiments" on classical fluids. I. Thermodynamical properties of Lennard-Jones molecules. *Phys. Rev.*, 159:98–103, 1967.

[95] `http://gulp.curtin.edu.au/`.

[96] E. R. Cope. *Dynamic properties of materials: Phonons from neutron scattering*. PhD thesis, University of Cambridge, 2010.

[97] H. J. Monkhorst and J. D. Pack. Special points for Brillouin-zone integrations. *Phys. Rev. B*, 13:5188–5192, 1976.

[98] I. Fischer, A. Bosak, and M. Krisch. Single-crystal lattice dynamics derived from polycrystalline inelastic x-ray scattering spectra. *Phys. Rev. B*, 79:134302, 2009.

[99] A. Bosak, I. Fischer, M. Krisch, V. Brazhkin, T. Dyuzheva, B. Winkler, D. Wilson, D. Weidner, K. Refson, and V. Milman. Lattice dynamics of stishovite from powder inelastic x-ray scattering. *Geophysical Research Letters*, 36(19), 2009.

[100] S. Gewurtz, H. Kiefte, D. Landheer, R. A. McLaren, and B. P. Stoicheff. Elastic constants of argon and neon by Brillouin scattering from single crystals near their triple points. *Phys. Rev. Lett.*, 29:1454–1457, 1972.

[101] L. A. Girifalco and V. G. Weizer. Application of the Morse potential function to cubic metals. *Phys. Rev.*, 114:687–690, 1959.

[102] R. C. Lincoln, K. M. Koliwad, and P. B. Ghate. Morse-potential evaluation of second- and third-order elastic constants of some cubic metals. *Phys. Rev.*, 157:463–466, 1967.

[103] R. A. Johnson and D. J. Oh. Analytic embedded atom method model for bcc metals. *Journal of Materials Research*, 4:1195–1201, 1989.

[104] M. R. Fellinger. *First principles-based interatomic potentials for modeling the body-centered cubic metals V, Nb, Ta, Mo, and W.* PhD thesis, Ohio State University, 2013.

[105] M. Guler and E. Guler. Embedded atom method-based geometry optimization aspects of body-centered cubic metals. *Chinese Physics Letters*, 30(5):056201, 2013.

[106] `http://www.castep.org`.

[107] W. Kohn and L. J. Sham. Self-consistent equations including exchange and correlation effects. *Phys. Rev.*, 140:A1133–A1138, 1965.

[108] P. Hohenberg and W. Kohn. Inhomogeneous electron gas. *Phys. Rev.*, 136:B864–B871, 1964.

[109] K. Burke. The ABC of DFT. `http://dft.uci.edu/doc/g1.pdf`, April 2007.

[110] J. S. Lin, A. Qteish, M. C. Payne, and V. Heine. Optimized and transferable nonlocal separable *ab initio* pseudopotentials. *Phys. Rev. B*, 47:4174–4180, 1993.

[111] M. H. Lee. *Advanced pseudopotentials for large scale electronic structure calculations.* PhD thesis, University of Cambridge, 1995.

[112] J. P. Perdew, K. Burke, and M. Ernzerhof. Generalized gradient approximation made simple. *Phys. Rev. Lett.*, 77:3865–3868, 1996.

[113] H. C. Andersen. Molecular dynamics simulations at constant pressure and/or temperature. *The Journal of Chemical Physics*, 72(4):2384–2393, 1980.

[114] F. Ercolessi and J. B. Adams. Interatomic potentials from first-principles calculations: The force-matching method. *EPL (Europhysics Letters)*, 26(8):583, 1994.

[115] Y. Mishin, D. Farkas, M. J. Mehl, and D. A. Papaconstantopoulos. Interatomic potentials for monoatomic metals from experimental data and *ab initio* calculations. *Phys. Rev. B*, 59:3393–3407, 1999.

[116] X. Y. Liu, J. B. Adams, F. Ercolessi, and J. A. Moriarty. EAM potential for magnesium from quantum mechanical forces. *Modelling and Simulation in Materials Science and Engineering*, 4(3):293–303, 1996.

[117] M. Z. Bazant, E. Kaxiras, and J. F. Justo. Environment-dependent interatomic potential for bulk silicon. *Physical Review B*, 56(14):8542–8552, 1997.

[118] A. B. Belonoshko, R. Ahuja, O. Eriksson, and B. Johansson. Quasi ab initio molecular dynamic study of Cu melting. *Physical Review B*, 61(6):3838–3844, 2000.

[119] P. Tangney and S. Scandolo. An ab initio parametrized interatomic force field for silica. *Journal of Chemical Physics*, 117(19):8898–8904, 2002.

[120] M. I. Mendelev, S. Han, D. J. Srolovitz, G. J. Ackland, D. Y. Sun, and M. Asta. Development of new interatomic potentials appropriate for crystalline and liquid iron. *Philosophical Magazine*, 83(35):3977–3994, DEC 11 2003.

[121] Youhong Li, Donald J. Siegel, James B. Adams, and Xiang-Yang Liu. Embedded-atom-method tantalum potential developed by the force-matching method. *Phys. Rev. B*, 67:125101, 2003.

[122] S. Izvekov and G. A. Voth. Multiscale coarse graining of liquid-state systems. *Journal of Chemical Physics*, 123(13), 2005.

[123] G. Grochola, S. P. Russo, and I. K. Snook. On fitting a gold embedded atom method potential using the force matching method. *Journal of Chemical Physics*, 123(20), 2005.

[124] Y. Q. Cheng, A. J. Cao, H. W. Sheng, and E. Ma. Local order influences initiation of plastic flow in metallic glass: Effects of alloy composition and sample cooling history. *Acta Materialia*, 56(18):5263–5275, 2008.

[125] H. W. Sheng, M. J. Kramer, A. Cadien, T. Fujita, and M. W. Chen. Highly optimized embedded-atom-method potentials for fourteen fcc metals. *Phys. Rev. B*, 83:134118, 2011.

[126] S. Izvekov and G. A. Voth. A multiscale coarse-graining method for biomolecular systems. *Journal of Physical Chemistry B*, 109(7):2469–2473, 2005.

[127] S.L. Shang, A. Saengdeejing, Z.G. Mei, D.E. Kim, H. Zhang, S. Ganeshan, Y. Wang, and Z.K. Liu. First-principles calculations of pure elements: Equations of state and elastic stiffness constants. *Computational Materials Science*, 48(4):813 – 826, 2010.

[128] R. P. Feynman and Michael Cohen. Energy spectrum of the excitations in liquid helium. *Phys. Rev.*, 102:1189–1204, 1956.

[129] A. D. B. Woods. Neutron inelastic scattering from liquid helium at small momentum transfers. *Phys. Rev. Lett.*, 14:355–356, 1965.

[130] R. A. Cowley and A. D. B. Woods. Inelastic scattering of thermal neutrons from liquid helium. *Canadian Journal of Physics*, 49(2):177–200, 1971.

[131] B. Fåk and K.H. Andersen. Neutron inelastic scattering from superfluid 4he beyond the roton minimum. *Physics Letters A*, 160(5):468 – 472, 1991.

[132] K H Andersen, W G Stirling, R Scherm, A Stunault, B Fak, H Godfrin, and A J Dianoux. Collective excitations in liquid 4 He: I. Experi-

ment and presentation of data. *Journal of Physics: Condensed Matter*, 6(4):821, 1994.

[133] H. R. Glyde and A. Griffin. Zero sound and atomiclike excitations: The nature of phonons and rotons in liquid ^{4}He. *Phys. Rev. Lett.*, 65:1454–1457, 1990.

[134] A. Miller, D. Pines, and P. Nozières. Elementary excitations in liquid helium. *Phys. Rev.*, 127:1452–1464, 1962.

[135] T. Burke, K. G. Major, and G. V. Chester. The motion of impurities and the spectrum of excitations in liquid helium-four. *Annals of Physics*, 42(1):144 – 172, 1967.

[136] M.R. Gibbs and W.G. Stirling. Temperature dependence of the phonon−maxon excitations in superfluid ^{4}He at SVP and 20 bars. *Journal of Low Temperature Physics*, 102(3-4):249–260, 1996.

[137] V. Tozzini and M.P. Tosi. Lattice vibrations and elastic constants of crystalline 4he and 3he near low-temperature melting. *Physica B: Condensed Matter*, 262(3–4):369 – 380, 1999.

[138] E. C. Svensson, W. Montfrooij, and I. M. de Schepper. Disappearance of roton propagation in superfluid ^{4}He at T_λ. *Phys. Rev. Lett.*, 77:4398–4401, 1996.

[139] T. Schneider and C. P. Enz. Theory of the superfluid-solid transition of ^{4}He. *Phys. Rev. Lett.*, 27:1186–1188, 1971.

[140] V. Celli and J. Ruvalds. Theory of the liquid-solid phase transition in helium ii. *Phys. Rev. Lett.*, 28:539–542, 1972.

[141] M. T. Dove, M. E. Hagen, M. J. Harris, B. M. Powell, U. Steigenberger, and B. Winkler. Anomalous inelastic neutron scattering from calcite. *Journal of Physics: Condensed Matter*, 4(11):2761, 1992.

[142] D. E. Galli, E. Cecchetti, and L. Reatto. Rotons and roton wave packets in superfluid ^{4}He. *Phys. Rev. Lett.*, 77:5401–5404, 1996.

[143] P. Nozières. Is the roton in superfluid ^{4}He the ghost of a Bragg spot? *Journal of Low Temperature Physics*, 137(1-2):45–67, 2004.

[144] G. J. Kalman, P. Hartmann, K. I. Golden, A. Filinov, and Z. Donkó. Correlational origin of the roton minimum. *EPL (Europhysics Letters)*, 90(5):55002, 2010.

[145] H. R. Glyde. *Excitations in Liquid and Solid Helium*. Oxford University Press, Oxford, 1994.

[146] K. Trachenko. Understanding the spin glass transition as a dynamic phenomenon. *Journal of Physics: Condensed Matter*, 23(36):366003, 2011.

[147] K. Trachenko and V. V. Brazhkin. Duality of liquids. *Scientific Reports*, 3(2188), 07 2013.

[148] D. Bolmatov, V. V. Brazhkin, and K. Trachenko. Thermodynamic behaviour of supercritical matter. *Nat Commun*, 4(3331), 08 2013.

[149] D. Bolmatov, V. V. Brazhkin, and K. Trachenko. The phonon theory of liquid thermodynamics. *Sci. Rep.*, 2(421), 05 2012.

[150] D. Bolmatov and K. Trachenko. Liquid heat capacity in the approach from the solid state: Anharmonic theory. *Phys. Rev. B*, 84:054106, Aug 2011.

[151] E. I. Andritsos, E. Zarkadoula, A. E. Phillips, M. T. Dove, C. J. Walker, V. V. Brazhkin, and K. Trachenko. The heat capacity of matter beyond the Dulong–Petit value. *Journal of Physics: Condensed Matter*, 25(23):235401, 2013.

[152] M. W. Zemansky. *Heat and Thermodynamics*, chapter 2, pages 28–33. McGraw-Hill Book Company, 4th edition, 1957.

[153] J. K. Roberts. *Heat and Thermodynamics*, chapter X, page 255. Blackie and Son Ltd, 1958.

[154] B. Yates. *Thermal expansion*, chapter 1, page 4. Plenum Press, 1972.

[155] A. Einstein. Die plancksche theorie der strahlung und die theorie der spezifischen warme. *Annalen der Physik*, 22(180-190), 1907.

[156] P. Debye. Theory of specific heats. *Chemical Abstracts*, 7(2891), 1913.

[157] M. T. Dove. *Structure and Dynamics: An atomic view of materials*, page 176. Oxford University Press, 2003.

[158] A. J. Walton. *Three Phases of Matter*, pages 314–315. Oxford University Press, 1990.

[159] G. Kh. Panova, N.A. Chernoplekov, A.A. Shikov, B.I. Savel'ev, and M.N. Khlopkin. Effects of amorphization on the vibrational specific heat of metallic glasses. *JETP*, 61(3):595 – 598, 1985.

[160] G. Burns. Comment on the low temperature specific heat of ferroelectrics, antiferroelectrics, and related materials. *Solid State Communications*, 35(11):811 – 814, 1980.

[161] J. C. Ho and D. P. Dandekar. Low-temperature heat capacities of RbCl, RbBr, and CsCl. *Phys. Rev. B*, 30:2117–2119, Aug 1984.

[162] M. Ahrens, R. Merkle, B. Rahmati, and J. Maier. Effective masses of electrons in n-type $SrTiO_3$ determined from low-temperature specific heat capacities, volume = 393, year = 2007, pages = 239 - 248. *Physica B: Condensed Matter*, (1–2).

[163] M. Cardona, R. K. Kremer, R. Lauck, G. Siegle, J. Serrano, and A. H. Romero. Heat capacity of PbS: Isotope effects. *Phys. Rev. B*, 76:075211, Aug 2007.

[164] A Durán, F Morales, L Fuentes, and J M Siqueiros. Specific heat anomalies at 37, 105 and 455 K in $SrTiO_3$:Pr, volume = 20, year = 2008. *Journal of Physics: Condensed Matter*, (8):085219.

[165] A. H. Romero, M. Cardona, R. K. Kremer, R. Lauck, G. Siegle, J. Serrano, and X. C. Gonze. Lattice properties of PbX (X = S, Se, Te): Experimental studies and ab initio calculations including spin-orbit effects. *Phys. Rev. B*, 78:224302, Dec 2008.

[166] M. Cardona, R. K. Kremer, R. Lauck, G. Siegle, A. Muñoz, and A. H. Romero. Electronic, vibrational, and thermodynamic properties of metacinnabar β-HgS, HgSe, and HgTe. *Phys. Rev. B*, 80:195204, Nov 2009.

[167] O. Kilian, G. Allan, and L. Wirtz. Near Kohn anomalies in the phonon dispersion relations of lead chalcogenides. *Phys. Rev. B*, 80:245208, Dec 2009.

[168] R. Shaltaf, X. Gonze, M. Cardona, R. K. Kremer, and G. Siegle. Lattice dynamics and specific heat of α-GeTe: Theoretical and experimental study. *Phys. Rev. B*, 79:075204, Feb 2009.

[169] N. W. Ashcroft and N. D. Mermin. *Solid state physics*. Saunders College, Philadelphia, 1976.

[170] C. Kittel. *Introduction to solid state physics*. John Wiley & Sons, 1996.

[171] B. Njegic and M. S. Gordon. Exploring the effect of anharmonicity of molecular vibrations on thermodynamic properties. *The Journal of Chemical Physics*, 125(22), 2006.

[172] A. A. Maradudin, P. A. Flinn, and R. A. Coldwell-Horsfall. Anharmonic contributions to vibrational thermodynamic properties of solids: Part II. The high temperature limit. *Annals of Physics*, 15(3):360 – 386, 1961.

[173] R. A. Cowley. Anharmonic crystals. *Reports on Progress in Physics*, 31(1):123, 1968.

[174] J. Rosén and G. Grimvall. Anharmonic lattice vibrations in simple metals. *Phys. Rev. B*, 27:7199–7208, Jun 1983.

[175] A. F. Guillermet and G. Grimvall. Analysis of thermodynamic properties of molybdenum and tungsten at high temperatures. *Phys. Rev. B*, 44:4332–4340, Sep 1991.

[176] D. C. Wallace. Anharmonic entropy of alkali metals. *Phys. Rev. B*, 46:5242–5245, Sep 1992.

[177] O. L. Anderson. *Equations of State of Solids for Geophysics and Ceramic Science*. Oxford University Press, 1995.

[178] A. R. Oganov and P. I. Dorogokupets. Intrinsic anharmonicity in equations of state and thermodynamics of solids. *Journal of Physics: Condensed Matter*, 16(8):1351, 2004.

[179] T. H. K. Barron. *Proc. Int. Conf. on Lattice Dynamics*, pages 247 – 254. Oxford Pergamon Press, 1965.

[180] G. Leibfried and W. Ludwig. Theory of anharmonic effects in crystals. volume 12 of *Solid State Physics*, pages 275 – 444. Academic Press, 1961.

[181] P. Brüesch. *Phonons: Theory and experiments I*, pages 162–163. Springer-Verlag, 1982.

[182] A. J. Leadbetter. Anharmonic effects in the thermodynamic properties of solids I. An adiabatic calorimeter for the temperature range 25 - 500 °C: the heat capacities of Al_2O_3 , Al and Pb. *Journal of Physics C: Solid State Physics*, 1(6):1481, 1968.

[183] B. Fultz. Vibrational thermodynamics of materials. *Progress in Materials Science*, 55(4):247 – 352, 2010.

[184] J. Frenkel. *Kinetic theory of liquids*, page 93. Oxford University Press, 1946.

[185] J. Frenkel. On the liquid state and the theory of fusion. *Trans. Faraday Soc.*, 33:58–65, 1937.

[186] G. Grimvall. The heat capacity of liquid metals. *Phys. Scr.*, 11(6):381, 1975.

[187] D. C. Wallace. Liquid dynamics theory of high-temperature specific heat. *Phys. Rev. E*, 57:1717–1722, Feb 1998.

[188] A. R. Dexter and A. J. Matheson. Temperature dependence of heat capacity and viscosity of non-associated liquids. *Trans. Faraday Soc.*, 64:2632–2638, 1968.

[189] L. Brillouin. On thermal agitation in liquids. *Trans. Faraday Soc.*, 33:54–55, 1937.

[190] J. H. Hildebrand, J. D. Bernal, E. Bauer, R. J. W. Le Fevre, F. Simon, F. C. Frank, and Magat. General discussion. *Trans. Faraday Soc.*, 33:86–87, 1937.

[191] A.V. Granato. The specific heat of simple liquids. *Journal of Non-Crystalline Solids*, 307–310(0):376–386, 2002.

[192] K. Trachenko. Heat capacity of liquids: An approach from the solid phase. *Phys. Rev. B*, 78:104201, Sep 2008.

[193] J. Frenkel. *Kinetic theory of liquids*, pages 188–249. Oxford University Press, 1946.

[194] G. Grimvall. *Thermophysical properties of materials.* Elsevier, 1999.

[195] L. D. Landau and E. M. Lifshitz. *Statistical Physics: Course of Theoretical Physics*, volume 5, chapter 6. Pergamon Press, 3rd edition, 1980.

[196] R. W. Roberts and R. Ruppin. Volume dependence of the grüneisen parameter of alkali halides. *Phys. Rev. B*, 4:2041–2046, Sep 1971.

[197] L. Stixrude and C. Lithgow-Bertelloni. Thermodynamics of mantle minerals — i. physical properties. *Geophys. J. Int.*, 162(2):610 – 632, 2005.

[198] M. S. Anderson and C. A. Swenson. Experimental equations of state for the rare gas solids. *Journal of Physics and Chemistry of Solids*, 36(3):145 – 162, 1975.

[199] S. Yamamoto, I. Ohno, and O. L. Anderson. High temperature elasticity of sodium chloride. *Journal of Physics and Chemistry of Solids*, 48(2):143 – 151, 1987.

[200] O. L. Anderson, D. G. Isaak, and S. Yamamoto. Anharmonicity and the equation of state for gold. *Journal of Applied Physics*, 65(4):1534–1543, 1989.

[201] F. Aguado and V. G. Baonza. Prediction of bulk modulus at high temperatures from longitudinal phonon frequencies: Application to diamond, *c*-BN, and 3*c*-SiC. *Phys. Rev. B*, 73:024111, Jan 2006.

[202] J. Xie, S. P. Chen, J. S. Tse, S. Gironcoli, and S. Baroni. High-pressure thermal expansion, bulk modulus, and phonon structure of diamond. *Phys. Rev. B*, 60:9444–9449, Oct 1999.

[203] K. Trachenko, M. T. Dove, K. D. Hammonds, M. J. Harris, and V. Heine. Low energy dynamics and tunneling states in silica glass. *Phys. Rev. Lett.*, 81:3431–3434, Oct 1998.

[204] L. Minervini, M. O. Zacate, and R. W. Grimes. Defect cluster formation in M_2O_3-doped CeO_2. *Solid State Ionics*, 116(3–4):339 – 349, 1999.

[205] W. Kob and H. C. Andersen. Testing mode-coupling theory for a supercooled binary Lennard-Jones mixture I: The van Hove correlation function. *Phys. Rev. E*, 51:4626–4641, May 1995.

[206] M. T. Dove. *Introduction to lattice dynamics*, page 3. Cambridge University Press, 1993.

[207] M. T. Dove. *Introduction to lattice dynamics*, page 10. Cambridge University Press, 1993.

[208] S. Tsuneyuki, M. Tsukada, H. Aoki, and Y. Matsui. First-principles interatomic potential of silica applied to molecular dynamics. *Phys. Rev. Lett.*, 61:869–872, Aug 1988.

[209] M. Matsui and M. Akaogi. Molecular dynamics simulation of the structural and physical properties of the four polymorphs of TiO_2. *Molecular Simulation*, 6(4-6):239–244, 1991.

[210] K. Trachenko, M. T. Dove, and E. K. H. Salje. Reply to comment on 'large swelling and percolation in irradiated zircon'. *Journal of Physics: Condensed Matter*, 15(37):6457, 2003.

[211] K. Trachenko, M. T. Dove, T. Geisler, I. Todorov, and B. Smith. Radiation damage effects and percolation theory. *Journal of Physics: Condensed Matter*, 16(27):S2623, 2004.

[212] G. E. Jelinek. Properties of crystalline argon, krypton, and xenon based upon the born−huang method of homogeneous deformations. iii. the low−temperature limit. *Phys. Rev. B*, 5:3210–3217, 1972.

[213] R. Ramji Rao and M. Peter. Grüneisen gamma of some cubic crystals from third-order elastic constants data. *Helvetica Physica Acta*, 47(6):705 – 715, 1974.

[214] D.S. Sanditov, A.A. Mashanov, M.V. Darmaev, B.D. Sanditov, and V.V. Mantatov. Grüneisen parameter and elastic constants of crystals and vitreous bodies. *Russian Physics Journal*, 52(3):221–230, 2009.

[215] F. A. Lindemann. The calculation of molecular vibration frequencies. *Physik. Z.*, 11:609 – 612, 1910.

[216] Z. H. Jin, P. Gumbsch, K. Lu, and E. Ma. Melting mechanisms at the limit of superheating. *Phys. Rev. Lett.*, 87:055703, Jul 2001.

[217] P. Gillet, F. Guyot, and J. M. Malezieux. High-pressure, high-temperature raman spectroscopy of Ca_2GeO_4 (olivine form): some insights on anharmonicity. *Physics of the Earth and Planetary Interiors*, 58(2–3):141 – 154, 1989.

[218] P. Gillet, P. Richet, F. Guyot, and G. Fiquet. High-temperature thermodynamic properties of forsterite. *Journal of Geophysical Research: Solid Earth*, 96(B7):11805–11816, 1991.

[219] F. Guyot, Y. B. Wang, P. Gillet, and Y. Ricard. Quasi-harmonic computations of thermodynamic parameters of olivines at high-pressure and high-temperature. A comparison with experiment data. *PEPI*, 98(1-2):17–29, NOV 1996. Session SW2 of the XXI IUGG General Assembly - Thermoelastic Properties of Deep Mantle Phases, Boulder, CO, July 02-14, 1995.

[220] P. Gillet, F. Guyot, and Y. Wang. Microscopic anharmonicity and equation of state of $MgSiO_3$-perovskite. *Geophysical Research Letters*, 23(21):3043–3046, 1996.

[221] P. Gillet, I. Daniel, and F. Guyot. Anharmonic properties of Mg_2SiO_4-forsterite measured from the volume dependence of the Raman spectrum. *EJM*, 9(2):255–262, MAR-APR 1997. 6th International Symposium on Experimental Mineralogy, Petrology and Geochemistry (EMPG-VI), Germany, April 10-13, 1996.

[222] P Gillet, I Daniel, F Guyot, J Matas, and JC Chervin. A thermodynamic model for $MgSiO_3$-perovskite derived from pressure, temperature and volume dependence of the Raman mode frequencies. *PEPI*, 117(1-4):361–384, JAN 2000. 6th Symposium of Study on the Earths Deep Interior (SEDI98), Tours, France, July 05-10, 1998.